Department of Physics and Astronomy
Heidelberg University

Bachelor Thesis in Physics
submitted by

Marleen Maxton

born in Cologne (Germany)

2023

Study of dielectronic recombination resonances and their strengths in highly charged oxygen ions

This Bachelor Thesis has been carried out by Marleen Maxton at the
Max-Planck-Institut für Kernphysik in Heidelberg
under the supervision of
Apl. Prof. Dr. José R. Crespo López-Urrutia

Abstract

This thesis focuses on studying the K-shell dielectronic recombination (DR) of highly charged oxygen ions using the PolarX electron beam ion trap. The aim is to measure absolute dielectronic resonance strengths. The x-ray spectrum was recorded for different electron beam energies, trap depths, and beam currents. The charge state distribution was also measured for each parameter combination using the ion extraction system. To determine the electron and ion space charge, we observed the apparent shift of the resonance energies with the electron beam current and trap depth. This helped us find the compensation factor for the negative space charge of the electron beam by the positive ion space charge. We used these values to infer the DR resonance energies, electron beam radius, and electron current density. We determined the absolute number of trapped ions by using the compensation factor, along with an independent measurement with a Faraday cup setup. We also estimated the overlap between the ion cloud and the electron beam using the space-charge-based electron beam radius and gyromagnetic radius of the trapped ions. Using these inferred parameters with the fitted X-ray line intensities, we determined the DR resonance strengths for selected resonances and compared them to distorted wave calculations using the FLEXIBLE ATOMIC CODE. The accurate measurements of the DR strengths are of interest to test atomic theory and beneficial for modeling of astrophysical and laboratory hot plasmas.

Zusammenfassung

Diese Arbeit befasst sich mit der Untersuchung der dielektronischen Rekombination (DR) in der K-Schale von hochgeladenen Sauerstoffionen unter Verwendung der PolarX-Elektronenstrahl-Ionenfalle. Ziel ist es, absolute dielektronische Resonanzstärken zu messen. Das Röntgenspektrum wurde für verschiedene Elektronenstrahl-Energien, Fallentiefen und Strahlströme aufgenommen. Auch die Ladungszustandsverteilung wurde für jede Parameterkombination mit dem Ionenextraktionssystem gemessen. Um die Elektronen- und Ionenraumladung zu bestimmen, beobachteten wir die scheinbare Verschiebung der Resonanzenergien mit dem Elektronenstrahlstrom und der Fallentiefe. Auf diese Weise konnten wir den Kompensationsfaktor für die negative Raumladung des Elektronenstrahls durch die positive Raumladung der Ionen ermitteln. Aus diesen Werten konnten wir die DR-Resonanzenergien, den Elektronenstrahlradius und die Elektronenstromdichte ableiten. Die absolute Anzahl der gefangenen Ionen wurde mit Hilfe des Kompensationsfaktors und einer unabhängigen Messung mit einem Faraday-Cup-Setup bestimmt. Außerdem schätzten wir den Überlapp zwischen der Ionenwolke und dem Elektronenstrahl anhand des auf der Raumladung basierenden Elektronenstrahlradius und des gyromagnetischen Radius der Ionen ab. Unter Verwendung dieser abgeleiteten Parameter und der Röntgenlinienintensitäten berechneten wir die DR-Resonanzstärken für ausgewählte Resonanzen und verglichen diese mit Berechnungen basierend auf *distorted wave calculations* mit dem FLEXIBLE ATOMIC CODE. Die genauen Messungen der DR-Stärken sind von Interesse, um die Atomtheorie zu testen und für die Modellierung von astrophysikalischen und im Labor erzeugten heißen Plasmen nützlich.

Contents

1 Introduction

More than 90% of the universe is made out of plasma which is often called the fourth state of matter [1]. Plasma is an ionised gas that consists of electrons, atoms, ions and molecules, often containing a significant fraction of highly charged ions that dominate the emission lines at very high temperatures.

Highly charged ions (HCI) have been stripped of a significant amount of their electrons and therefore showcase extreme properties compared to weakly charged ions. They constitute a vital interface between atomic physics, plasma physics and astrophysics as they play an essential role in our understanding of the processes involved in laboratory and astrophysical plasma. Due to the decreased shielding of the nuclear charge Z and the consequent change in the energetic levels of the electrons, optical transitions in neutral atoms and weakly charged ions are shifted to the x-ray regime in HCIs [2]. Since each atom can exist in Z different ionised states, HCIs account for a vast number of characteristic spectral lines. This renders them highly interesting objects for spectroscopy which is concerned with the interaction of light and matter.

The brightest x-ray source seen on earth is the sun [3] and its nature has been an object of fascination for millennia. An important milestone in our understanding of the sun was the observation of dark lines in the solar spectrum in 1802 by William Hyde Wollaston [4] and independently by Joseph Fraunhofer in 1814 [5]. The explanations for these lines was discovered fifty years later in 1860 by Gustav Robert Kirchhoff and Robert Bunsen. Each element shows a characteristic line spectrum and the so called Fraunhofer lines in the solar spectrum were identified as characteristic absorption lines of elements that exist in natural abundance on earth [6]. With this realisation it is possible to determine the composition of any cosmic object if the spectral pattern is familiar to the observer, providing a powerful tool to astrophysicists whose knowledge of the universe is mostly based on radiation spectra. However, not all solar lines could be explained with the elemental spectra observed on earth. Though the emission lines of HCIs were already observed in laboratory vacuum spark experiments in the mid nineteen-thirties, they were believed to be rare in nature [7]. This changed in 1942, when Bengt Edlén identified the origin of absorption lines in the solar spectrum as Fe^{13+} and marked the beginning of astrophysical spectroscopy of HCIs [8].

HCI spectroscopy is a powerful diagnostic tool for characterising laboratory and astrophysical plasmas. The emission lines entail information about parameters of the plasma such as the charge state distribution, electron and ion density, dynamics, energy balance and temperature distribution. The velocity of the plasma can be determined from the Doppler shift and the consequent broadening of the line width, whilst the line intensities depend e. g. on the number

of ions present in the plasma, the charge state distribution and the temperature [1]. These physical relations can be put into a theoretical model to describe the plasma based on different characteristic parameters and infer the observable quantities. This model can then be compared to the experimental measurements to deduce the properties of the plasma and benchmark the theoretical assumptions. A detailed knowledge of the ion spectrum is therefore essential.

Since x-ray radiation is efficiently absorbed in the earths atmosphere [9], physicists had to rely on spacecraft-based observations to investigate the cosmic x-rays [10, 11]. The invention of more powerful ion sources made it possible to examine the x-ray radiation of HCIs under laboratory conditions to benchmark the wealth of data those satellites acquired. One of those ion sources, the electron beam ion trap (EBIT), proved to be of particular use for spectroscopic studies. They facilitate a relatively simple and efficient way to produce and store HCIs for long times. Ions are sequentially ionised by an electron beam of high current density and confined by the space charge of the beam itself and additionally by a set of electrodes. With these devices, it has been possible to produce charge states up to bare uranium ions [12]. The parameters inside the EBIT can be accurately adjusted, allowing for the controlled production of the desired charge states. The ions can either be studied directly inside the EBIT as they radiate as a result of the interaction with the electron beam and other ions or be extracted for further experiments.

One important electron-ion interaction which can be observed in the emitted spectrum is the dielectronic recombination (DR). In this resonant two-step process, an electron from the continuum is first captured into an excited state and a bound electron is excited with the freed energy. In a second step, one of the excited electrons decays radiatively to a lower state by emitting a photon of characteristic energy. In 1964, Alan Burgess first realised the importance of the DR process for HCIs in the solar corona at sufficiently high temperatures [13]. As the DR process occurs resonantly, it plays a key role for the charge state distribution, the population of excited states, the photon scattering and the cooling effects due to radiative losses [1, 14–17]. A good understanding of the DR process hence plays an important role in the experimental diagnostic and theoretical modeling of plasma. For this, however, a precise knowledge of the resonance energies and strengths is crucial.

The dielectronic resonances of oxygen are of special interest to the astrophysical community. Oxygen is the third-most abundant element in the universe as it is synthesised at the end of the helium fusion of massive stars and then scattered by SNeII supernova explosions [18]. Thus, it is an important constituent of the interstellar medium and a vital puzzle piece in understanding the physical processes in the cosmos. In the sun, it accounts for roughly 1% of the total mass and can be especially observed in the solar corona and winds [19].

The aim of this thesis is to measure the absolute resonance strengths of the dielectronic recombination in highly charged oxygen ions. The advantage of providing such absolute values is that they do not rely on theoretical data and thus constitute an independent determination of the resonance strengths that can be compared with the theory. This is something that has not been achieved before for highly charged ions.

In chapter 2, the properties of highly charged ions, the theory behind the charge changing processes occuring in an EBIT and the interaction of the electron beam with the trapped ion cloud are outlined. The experimental set-up of the EBIT and the measurement scheme employed to extract the absolute resonance strengths are presented in chapter 3. The total ion charge in the trap is estimated in chapter 4 and the charge states in the trap are identified. Furthermore, the ion and electron space charge are calculated from the DR resonance energies, the charge state distribution inside the trap is determined and the electron current density, the number of ions and the overlap factor are estimated. In a last step, those quantities together with the fitted intensity of the observed dielectronic resonances are used to calculate the absolute resonance strengths. In the last chapter 5, the results are summarised and an outlook is provided.

2 Theoretical Background

In order to gain a better understanding of the physical processes in an Electron Beam Ion Trap (EBIT), this chapter will cover an introduction to highly charged ions and the main charge changing processes observed in the experiment. The basic principle of an EBIT will be discussed with a focus on the physics of the electron beam, the ion cloud and time-of-flight measurements. This chapter is oriented on [2] and [20].

2.1 Highly charged ions

Highly charges ions (HCI) are atoms that were stripped of a large number of electrons. When electrons are removed from the atom, the screening effect of the nuclear charge Z decreases, leading to a higher effective nuclear charge Z_{eff} as seen by the electrons. The electrons closest to the nucleus experience the highest effective charge. Since the Coulomb potential is proportional to Z_{eff}^2, the electron cloud is more tightly bound as the effective charge increases and the electronic wave functions in HCIs are highly compressed. The size of the ions therefore decreases, forming compact objects. Due to this Coulomb scaling, the ionisation energies grow rapidly with increasing charge. For hydrogen-like ions, the ionisation energy is proportional to Z^2.

The energetic levels of the electrons in the ion move further apart as the charge increases, shifting the wavelengths of photons emitted via electronic transitions into the x-ray regime. The separation of energetic levels with different principle quantum number n is mainly given by the Coulomb potential and the photon energies for these transitions thus scale with Z_{eff}^2. For transitions with the same principle quantum number but different fine structure levels, the photon energies scale more strongly with Z_{eff}^4, whereas transitions between the hyperfine levels scale with Z_{eff}^3. In an external magnetic field, the energetic levels of the electrons shift due to the Zeeman effect, whilst the Stark effect shifts them if external electric fields are present. Both effects decrease with higher effective nuclear charge Z_{eff}. The ion is therefore less susceptible to external influences, whilst the photon energies are shifted to much higher energies, rendering it a highly interesting object for spectroscopy e. g. proposed x-ray frequency combs and quantum computing [21, 22].

In addition, some familiar quantum mechanical selection rules for transitions inside the ion are less restrictive in HCIs due to a change in the coupling schemes of the electrons. Transitions that would normally be forbidden or suppressed can now be much stronger.

2.2 Charge state distribution

The charge state distribution observed during the experiment is determined by the ionisation, recombination, charge exchange processes taking place inside the EBIT, as well as the escape rate of the ions. The HCIs inside the EBIT are mainly produced by sequential electron impact ionisation as a result of the interaction with the electron beam. Whilst the ions are confined inside the EBIT, they can also recombine to lower charge states. The primary processes involved are radiative recombination and dielectronic recombination. A schematic depiction of both process can be seen in Figure 2.1. Since photoionisation depends strongly on the number of photons present, it is negligible for EBIT applications without the use of an additional light source.

2.2.1 Electron impact ionisation

Electron impact ionisation (EII) encompasses the removal of a bound electron upon interaction of the ion with a free electron. The process can only occur if the kinetic energy of the free electron is higher than the binding energy of the least tightly bound electron. The binding energy of the most weakly bound electron hence constitutes a threshold for electron impact ionisation and the highest charge state that can be achieved inside the EBIT is thus limited by the electron beam energy. The cross section of this process is a function of the beam energy that is zero at the threshold and rises to a peak value at an energy of about two to three times the electron ionisation potential. It decreases with increasing charge q of the ion [20]. The process can be described by

$$A^{q+} + e^- \rightarrow A^{(q+1)+} + 2e^-. \tag{2.1}$$

2.2.2 Radiative recombination

Radiative recombination (RR) is the inverse process to photoionisation. An ion captures an electron from the continuum to a bound state whilst simultaneously emitting a photon with the energy $\hbar\omega$ as summarised by

$$A^{q+} + e^- \rightarrow A^{(q-1)+} + \hbar\omega. \tag{2.2}$$

The photon energy E_γ is given as a result of energy conservation by

$$E_\gamma = E_{\text{kin}} - E_b, \tag{2.3}$$

where E_{kin} is the kinetic energy of the free electron and E_b the binding energy of the state after the recombination.

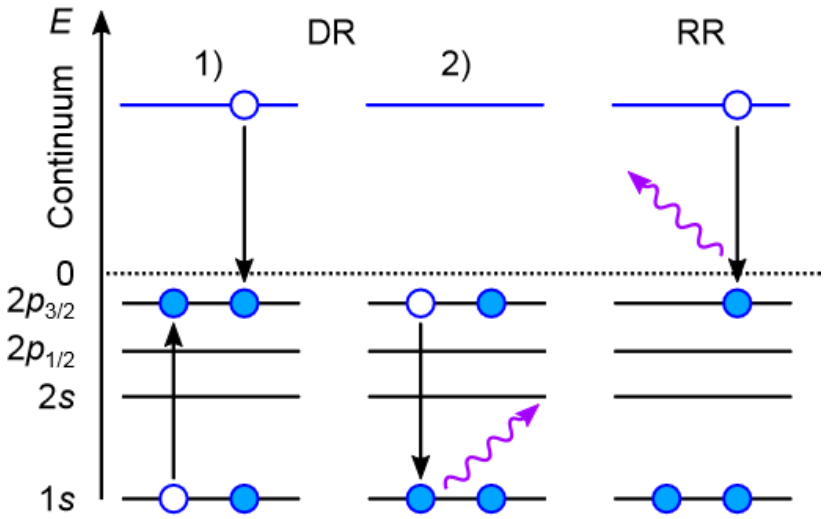

Figure 2.1: Schematic overview of the KLL dielectronic recombination (left) and radiative recombination (right). Left: 1) An electron from the continuum is resonantly captured into a bound state in the L shell, exciting a bound electron from the K shell into the L shell with the freed energy. The excitation energy matches the energy released by the capture. 2) The excited state decays radiatively, emitting a photon of characteristic energy. Right: A free electron is captured non-resonantly. The released energy is emitted as a photon. Figure adapted from [23]

2.2.3 Dielectronic recombination

Dielectronic recombination (DR) is a resonant two-step process and the inverse process to the Auger-Meitner effect. In the DR process, a photon of the energy $\hbar\omega$ is radiated which can be described by

$$A^{q+} + e^- \rightarrow \left(A^{(q-1)+}\right)^{**} \rightarrow A^{(q-1)+} + \hbar\omega. \tag{2.4}$$

In a first step, an electron from the continuum is captured into an excited state and the energy released during the capture is transferred to another bound electron, exciting it to a higher energy level. The ion enters a doubly excited state. Due to the discrete energy levels of the ion, this is a resonant process with the kinetic energy of the free electron E_{kin} being determined by

$$E_{\text{kin}} = \Delta E - E_b, \tag{2.5}$$

where ΔE is the excitation energy of the bound electron and E_b the binding energy of the captured state. In a second step, the excited ion decays radiatively. One of the excited electrons decays to a lower state and emits a photon equal to the excitation energy. Since the DR process is possible for many different energy levels, the naming convention includes the principle quantum number. For instance, the KLM resonance involves a free electron being captured into the M-shell and an electron from the K-shell being excited to the L-shell.

Resonance strength

The resonance strength S for a DR line with a cross section σ is defined as

$$S = \int_0^\infty \sigma(E) dE, \tag{2.6}$$

where E is the electron beam energy [24]. Due to the unidirectional electron beam, the resonant capture of an electron in the DR process leads to a nonstatistical occupation of the magnetic sublevels. The photon emitted in the consequent radiative decay is polarized and the emission is hence anisotropic. Since the photon detectors are mounted perpendicular to the electron beam axis, the polarization effect has to be taken into account and the calculated resonance strengths are only valid at a 90° angle. The resonance strength $S_{4\pi}$ which is averaged over the solid angle 4π is given by

$$S_{4\pi} = S_{90^\circ} \cdot \frac{3 - P}{3}, \tag{2.7}$$

where S_{90° is the resonance strength at 90° relative to the beam axis and P the polarization [25].

2.3 Electron Beam Ion Trap

Electron Beam Ion Traps (EBIT) are used to breed and trap HCIs. A schematic overview of the fundamental principle can be seen in Figure 2.2. The most important elements of an EBIT are the electron gun, the collector and the drift tubes which are formed by an assembly of cylindrical electrodes. These components are arranged along the electron beam axis with the drift tubes in the trap center being surrounded by magnets. Electrons are accelerated by the difference between the voltages applied to the electron gun and the drift tubes. In the trap center, the electron beam sequentially ionises the atoms by electron impact ionisation and simultaneously trap the produced ions radially with its negative space charge. In order to increase the current density and consequently the production rate of the ions, the electron beam is magnetically compressed along the beam axis with the maximum compression being reached in the trap center. Axially, the ions are trapped by a negative bias to the central drift tube with respect to both adjacent drift tubes, forming a potential well. After passing the drift tubes, the electron beam is decelerated and dumped at the collector. The stored ions can be ejected from the EBIT by inverting the axial trapping potential and extracted by subsequent ion optical elements for use in further experiments.

2.3.1 Electron beam

Interactions between the free electrons from the electron beam and the ions inside the ion cloud can only take place in the regions where they overlap. The electron beam size therefore constitutes an important parameter for the experiment. Under the assumption of an electron gas

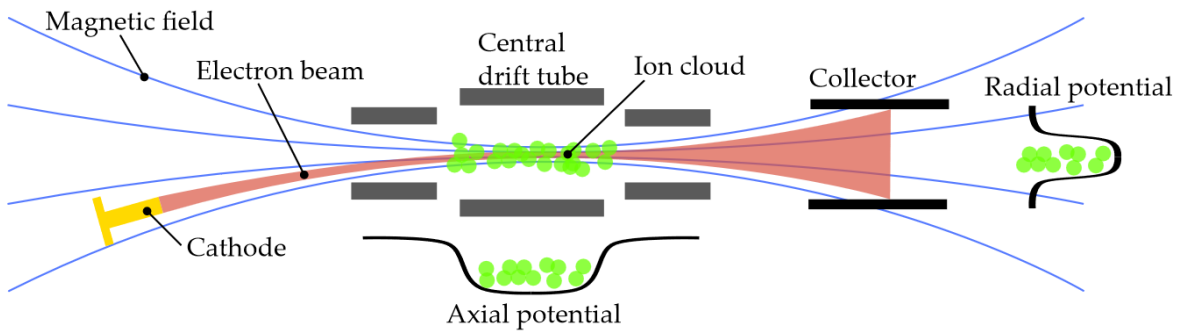

Figure 2.2: Principle of an electron beam ion trap. Electrons are emitted by the cathode and electrostatically accelerated towards the central drift tube. The electron beam is compressed by the magnetic field to reach its highest current density in the trap center where the ion cloud is formed through sequential electron impact ionisation. Axially, the ions are confined by the potential well resulting from the drift tube voltages. Radial confinement is accomplished by the negative electron beam space charge. The electron beam expands with the decreasing magnetic field and is dumped on the collector. Figure adapted from [26]

that is emitted in a laminar flow with zero temperature and at zero magnetic field, the Brillouin radius r_B describes the size of an electron beam that is compressed by a magnetic field B

$$r_B = \sqrt{\frac{2m_e I}{\pi\epsilon_0 v_e e B^2}}, \tag{2.8}$$

where m_e is the electron mass, e the elementary charge, ϵ_0 the vacuum electric permittivity, v_e the electron velocity and I the current of the electron beam [27]. However, the electrons are emitted thermionically at a cathode temperature T_c, the electron beam is not laminar and the magnetic field at the cathode B_c cannot be assumed to be zero. Consequently, the beam size increases and the resulting beam can be described by the Herrmann radius r_H which is predicted to contain 80% of the electron beam.

$$r_H = r_B\sqrt{\frac{1}{2}+\frac{1}{2}\sqrt{1+4\left(\frac{8k_B T_c r_c^2 m_e}{e^2 r_B^4 B^2}+\frac{B_c^2 r_c^4}{B^2 r_B^4}\right)}} \tag{2.9}$$

k_B is the Boltzmann constant and r_c the diameter of the cathode [28]. The ions are trapped radially by the space charge potential Φ_e of the electron beam which can be expressed by

$$\Phi_e(r \le r_e) = \frac{I}{4\pi\epsilon_0 v_e}\left[\left(\frac{r}{r_e}\right)^2 + \ln\left(\frac{r_e}{r_{\mathrm{dt}}}\right)^2 - 1\right] \tag{2.10}$$

$$\Phi_e(r \ge r_e) = \frac{I}{2\pi\epsilon_0 v_e}\ln\left(\frac{r}{r_{\mathrm{dt}}}\right), \tag{2.11}$$

where r_{dt} represents the inner radius of the drift tubes and r_e the electron beam radius. It was derived by solving the Poisson equation [29]. Since the electron velocity v_e is in the relativistic

regime, it is calculated by rearranging the formula of the relativistic kinetic energy E_{kin} to

$$v_e = c \cdot \sqrt{1 - \left(\frac{m_e c^2}{E_{\text{kin}} + m_e c^2} \right)^2} \tag{2.12}$$

with the speed of light c. Different models for the electron density distribution exist. In general, the radial distribution of the electron beam is assumed to be of Gaussian shape. The average current density j_e of the electron beam is given by

$$j_e = \frac{I}{\pi r_e^2}. \tag{2.13}$$

The energy spread of the electron beam is very small compared to the energy itself and the beam is therefore quasi-monoenergetic. Since the ions are confined at the position of DT4, the accelerating potential of the EBIT is in first approximation given by the difference of the cathode potential Φ_{cath} to the potential of DT4 Φ_{DT4}. However, the potential difference has to be corrected for the space charge contribution of the electron beam Φ_e and the ion cloud Φ_i as well as for the work function of the cathode W_{cath} and DT4 W_{DT4}. The space charge of the electron beam is partially compensated by the space charge of the ion cloud. This results in a beam energy of

$$E_{\text{beam}} = e(\Phi_{\text{DT4}} - \Phi_{\text{cath}} + \Phi_i - \Phi_e - W_{\text{DT4}} + W_{\text{cath}}). \tag{2.14}$$

Due to the effective beam energy differing from the nominal beam energy given by the voltages applied to the cathode and DT4, the DR resonance energies seem to be shifted when the space charge changes.

2.3.2 Ion cloud

The ion cloud consists of many different charge states of various elements whose populations are constantly changed by ionisation, recombination and escape to form an equilibrium charge state distribution. In addition to the injected elements, the residual gas inside the EBIT gets ionised and trapped. Due to the ion-ion collisions happening on shorter time scales than charge changing processes, the energy is assumed to be distributed thermally among a specific charge state q_i and each charge state is therefore associated with a specific temperature T_i. The ion temperature tends to increase with the charge state and can be approximated in a closed trap by

$$k_B T_i \approx \frac{q_i V_T}{5} \tag{2.15}$$

with the trap depth V_T [20]. The ion temperature also influences the spacial distribution of the ions which can be assumed to follow a Boltzmann distribution

$$n_i(r) = n_i(0) \exp\left(-\frac{e q_i \Phi(r)}{k_B T_i} \right), \tag{2.16}$$

where $n_i(r)$ is the ion density at a radial distance r from the trap axis, $n_i(0)$ the density on the beam axis and $\Phi(r)$ the total electrostatic potential at a distance r [20].

Electron beam heating is the major source of heating inside the EBIT and has the strongest effect on higher charge states. Ions are heated due to long-range Coulomb collisions with electrons from the beam. The main source of cooling is evaporative cooling. Ions that are sufficiently energetic escape from the trap. This process is more likely for lower charge states that are less tightly bound by the trap potential. Since the total temperature of the ions is lowered by evaporative cooling, ion trapping is improved. In some experiments light gases are specifically injected for this reason. The kinetic energy of the ions is assumed to follow a Maxwell-Boltzmann distribution. As the trap gets shallower, energetic ions from the tail of the distribution can escape the trap. However, due to the high rate of ion-ion collision, the ion cloud quickly regains equilibrium. Since the most energetic ions have left the trap, the ion temperature is reduced and the Maxwell-Boltzmann distribution adjusts to the lower temperature and gets narrower. This process leads to a differential equation for the rate of escape for ions with charge q_i

$$\frac{dN_{q_i}}{dt} = -N_{q_i}\nu_i \left(\frac{\exp(-\omega_i)}{\omega_i} - \sqrt{\omega_i}\left(\mathrm{erf}(\omega_i) - 1\right) \right) \tag{2.17}$$

with

$$\omega_i = \frac{q_i V_T}{k_B T_i}. \tag{2.18}$$

N_{q_i} is the number of ions with charge q_i and ν_i the coulomb collision rate with other ions [30].

2.4 Time-of-flight measurements

The different charge-to-mass ratios q/m of the confined ions can be identified by a time-of-flight measurement. With these ratios the relative abundance of elements and charge states inside the trap can be reconstructed. The ions are ejected from the trap by an acceleration potential U_{acc}, traverse a length L and reach a detector that is capable of time resolved measurements as shown in Figure 2.3. Assuming the motion of the ions in the trap to be negligible compared to the velocity acquired by the kick, the kinetic energy of the ions after leaving the trap is

$$E_{\mathrm{kin}} = qU_{\mathrm{acc}}. \tag{2.19}$$

The velocity v_i of the ions is in the non-relativistic regime and the kinetic energy can therefore be set equal to

$$E_{\mathrm{kin}} = \frac{1}{2}mv_i^2, \tag{2.20}$$

resulting in

$$v_i = \sqrt{2U_{\text{acc}}\frac{q}{m}} \tag{2.21}$$

$$\Rightarrow t_{\text{ToF}} = \frac{L}{v_i} = \frac{L}{\sqrt{2U_{\text{acc}}}}\frac{1}{\sqrt{\frac{q}{m}}} \tag{2.22}$$

with t_{ToF} being the measured time from acceleration to detection. $L/\sqrt{2U_{\text{acc}}}$ can be assumed to be approximately constant for all ions since it depends on the parameters of the EBIT [31].

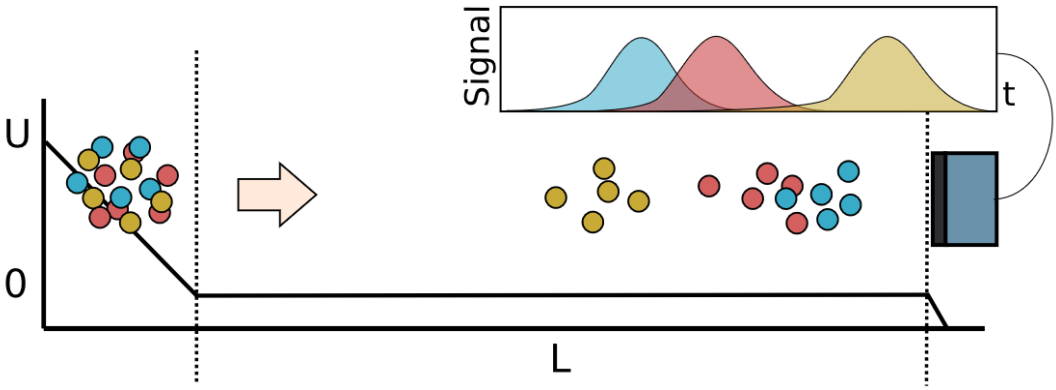

Figure 2.3: Principle of a time-of-flight measurement. The ion cloud is accelerated towards the detector and the ions with different q/m ratio separate over the duration of the flight due to their varying velocities. Figure adapted from [32]

3 Experimental setup of the PolarX-EBIT

In this chapter, the working principle of an EBIT will be discussed in more detail by presenting the PolarX-EBIT that was used in this work. In addition, the measurement schemes conceived to obtain absolute DR resonance strengths will be outlined.

3.1 PolarX-EBIT

The PolarX-EBIT is a Heidelberg compact electron beam ion trap (HC-EBIT). A schematic depiction can be seen in Figure 3.1. Since the HC-EBITs are operated at room temperature and employ permanent magnets, they are much smaller than conventional EBITs, cost less to construct and are easier to maintain, operate and transport. The HC-EBITs are able to produce hydrogen-like ions up to iron and helium-like and lithium-like ions up to xenon. Electron beam currents of up to 80 mA and beam energies of up to 10 keV can be reached. The PolarX-EBIT has a differentially pumped gas injection system. However, the measurements were performed with the residual gas in the trap and the injection system was not utilised in this work. With its off-axis electron gun and the resulting optical access along the beam axis, the PolarX-EBIT was specifically designed for operation at synchrotron and FEL facilities [33].

3.2 Magnetic structure

The magnetic field required for the electron beam compression is provided by a structure of cylindrical permanent neodymium (NbFeB) magnets. The magnets are stacked and fixed between magnetic steel parts to achieve a magnetic field of up to 0.86 T in the trap center as shown in Figure 3.2. Four soft-iron rods and two soft-iron pole pieces form the yoke of the structure. The latter concentrate the magnetic field in the trap center. The whole structure is axially symmetric at the trap center and has a discrete four fold rotational symmetry around the beam axis, resulting in a nearly rotationally symmetric magnetic field. In order to achieve maximal beam compression in the trap center, the magnetic field is optimised to have a flux density close to zero at the cathode position and its maximal flux density in the center of the trap. Furthermore, the magnetic field is sufficiently high along the beam axis to allow for a good electron beam transport. A measurement of the magnetic field for the VAUQSI HC-EBIT is shown in Figure 3.3. The magnetic structure is identical to the structure of the PolarX-EBIT.

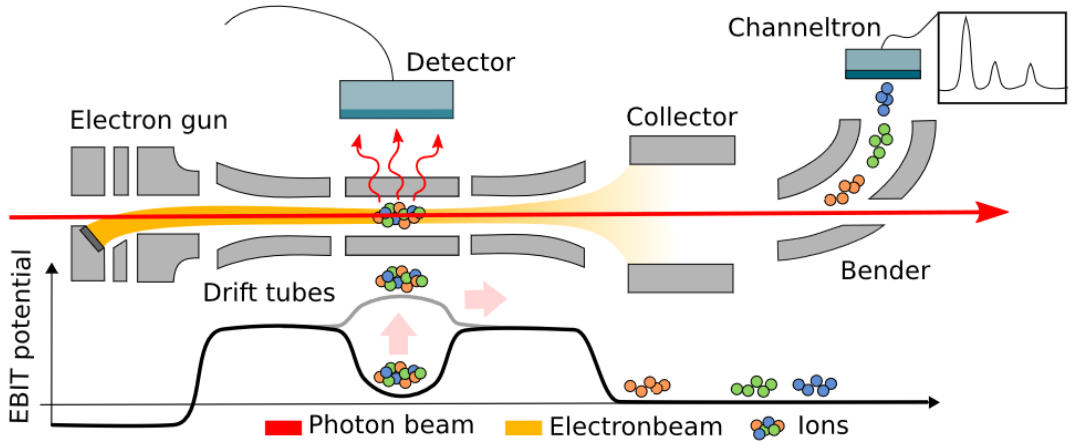

Figure 3.1: Overview of the PolarX-EBIT. At the trap center, the photons are detected with a silicon drift detector. Ions can be ejected from the trap, deflected by the electrostatic bender and dumped onto the channeltron for a time-of-flight measurement. An external photon beam can be overlapped with the electron beam along the beam axis. Figure adapted from [32]

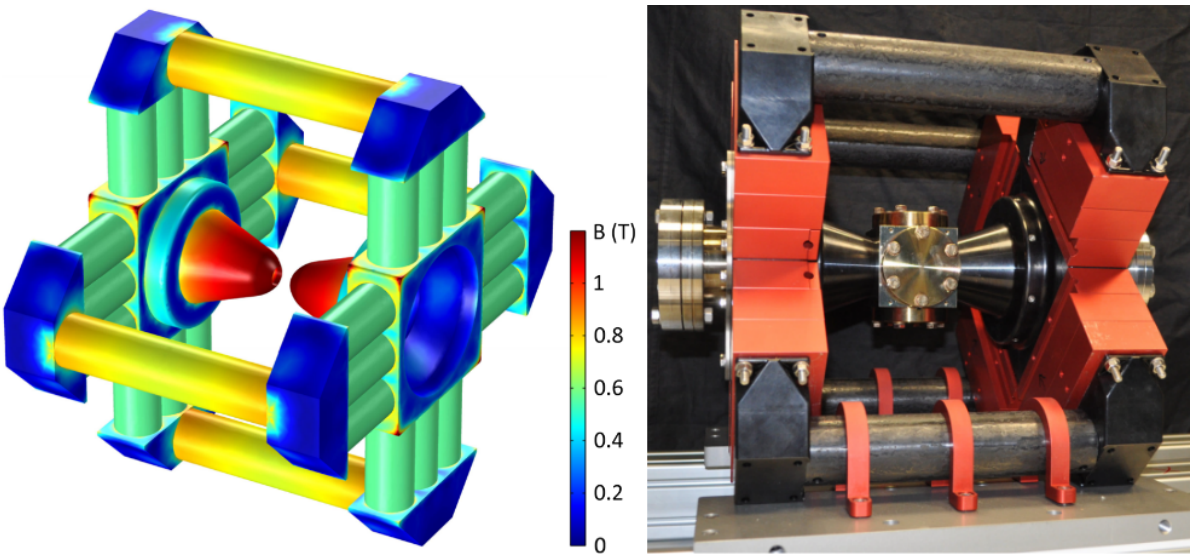

Figure 3.2: Magnetic structure. Left: Simulated absolute magnetic flux density on the surface of the magnetic structure. Stacked permanent magnets (green) create the magnetic field, whilst soft-iron rods (yellow) and soft-iron pole pieces (red) guide and concentrate the field in the trap center, reaching a flux density of up to 0.86 T. Figure adapted from [33]. Right: Magnetic structure of the PolarX-EBIT. The permanent magnets are located inside the red cartridges. Figure adapted from [26]

The central cube that surrounds the drift tubes has four radial ports, one for pumping, one for gas injection and two for optical access. The ports for optical access provide a large solid angle that leads to a high photon count rate on the mounted detectors.

To achieve the highest charge states and reduce the contamination inside the trap, the EBIT is pumped in three stages, the first including four turbo molecular pumps (TMP) for the different regions of the EBIT that are connected to another TMP in the second stage. In the third stage, the intermediate TMP is backed by a scroll pump. With this pumping system, ultra high vacuum conditions with a pressure in the 10^{-9} mbar-regime can be reached [33].

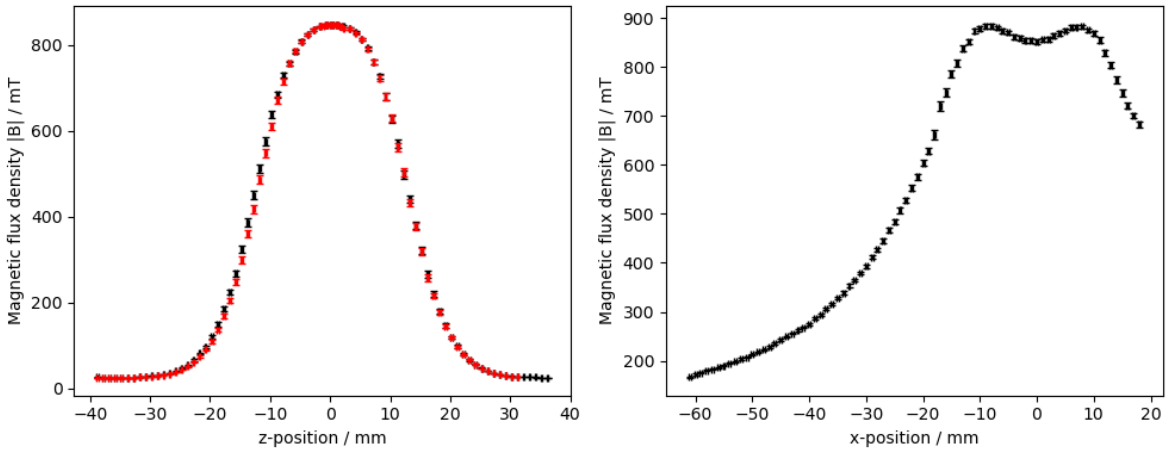

Figure 3.3: Measured magnetic flux density of the VAUQSI-EBIT which has an identical design to the PolarX-EBIT. The measurement was performed using a Hall sensor. Left: Magnetic flux density along the beam axis with a maximal density of (847.9 ± 2.1) mT. The Hall sensor was moved strictly inwards (black) and outwards (red) to observe the hysteresis of the probe. Right: Magnetic flux density perpendicular to the beam axis with a maximum density of (884.0 ± 4.5) mT and a density of (851.7 ± 4.3) mT in the trap center.

3.3 Electron gun

The electron gun supplies the free electrons for the beam and is depicted in Figure 3.4. It consists of the cathode, the focus electrode and the anode that are separated by electrically isolating alumina-ceramic rods. In order to achieve the highest possible overlap between the ion cloud and an incoming photon beam, the gun is designed as an off-axis electron gun so that the photon beam can freely pass through the EBIT along the beam axis. The electron gun is structured so that it is open for pumping and its position can be optimised using an XYZ-axis manipulator. It can reach current emission densities of up to $10 \frac{\mathrm{A}}{\mathrm{cm}^2}$.

The electrons are emitted by a thermionic dispenser cathode made out of a porous tungsten matrix that is impregnated with barium. Over time, barium evaporates from the surface of the cathode due to the high temperatures involved. This loss is then replenished by the barium stored inside the tungsten matrix through diffusion, allowing for a stable beam operation.

Because of its low work function of approximately 2 eV, the cathode can be operated at a lower temperatures of circa 1300 K which allows for a better compression of the electron beam according to the Herrmann radius in equation 2.9. In the off-axis electron gun, the cathode is tilted by 22° with respect to the horizontal plane.

The focus electrode is employed to compensate for distortions of the potential, improve the beam transport and control the emission current together with the copper anode. It is manufactured out of molybdenum to resist the high cathode temperature. Due to the magnetic field, the electron trajectories are bent sideways according to the Lorentz force when the electrons are steered onto the beam axis. To correct for this effect, the focus electrode is vertically separated into two independent electrodes.

The copper anode is used for beam steering and to regulate the emission current. Since the cathode emits the electrons off-axis, the beam has to be deflected back onto the beam axis. For this, the anode is split into two electrodes at a 35° angle with respect to the horizontal plane. Separate voltages can be applied to both electrodes. The rear anode defines the extraction potential, whilst the front anode is utilised for beam steering [33].

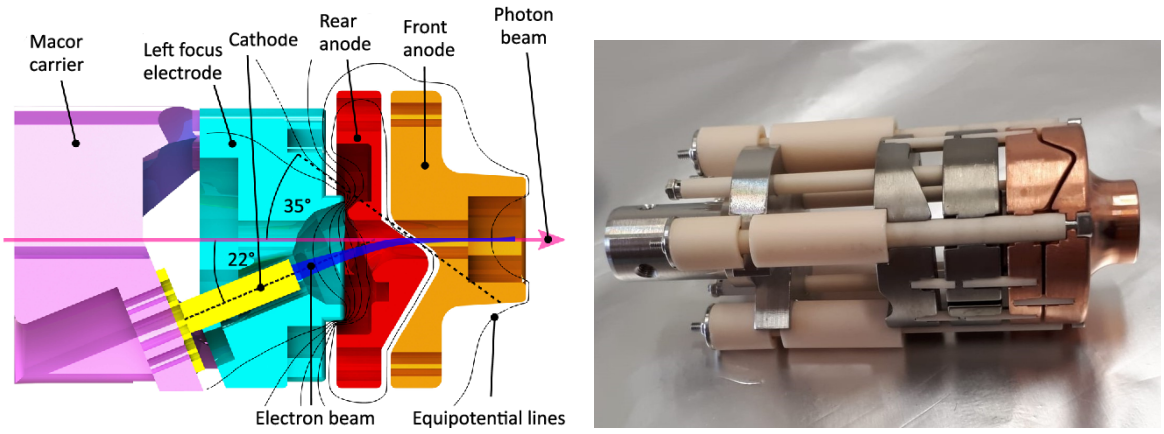

Figure 3.4: Off-axis electron gun. Left: Schematic cross section of the electron gun. Due to the angled cathode, the photon beam can freely pass through the structure. The anode is split at 35° with respect to the horizontal plane. It bends the electrons onto the beam axis, whilst the vertically split focus electrode corrects for the deflection due to the Lorentz force. Figure adapted from [33]. Right: Electron gun of the SQS-EBIT that is identical in design.

3.4 Drift tubes

By applying voltages to the drift tubes, the electrons are accelerated to the trap center and the ions are confined in the center of the EBIT. The drift tubes are cylindrical electrodes in the center of the trap that are made out of a titanium alloy and fixed on alumina-ceramic rods for precise spacing and electrical insulation as seen in Figure 3.5. The effective trap length of DT4

amounts to 22 mm, whilst the inner diameter is 5 mm. To gain optical access to the trap, DT4 has four cut-outs of 16 mm length and 2.5 mm width that are covered with a stainless-steel mesh to reduce fringe effects. The cut-outs permit a large opening angle of 58° to observe photon emission from the trap.

After leaving the electron gun, the beam is fed into the drift tube assembly by a trumpet-shaped entrance. Individual voltages can be applied to each drift tube. In the PolarX-EBIT, DT3 and DT5 that constitute the walls of the potential well are synchronised to form a symmetric trap. The drift tubes DT1 and DT2 are used to refocus the beam. DT3 to DT5 confine the ions axially. DT6 is grounded in the PolarX-EBIT. The whole drift tube assembly is positively biased in order to accelerate the electron beam. The trap can be inverted to extract the trapped ions by applying a fast high voltage potential to DT4 with a BEHLKE switch.

Since the drift tubes are located in close proximity to each other, the assembly is subjected to electrostatic reach-through effects due to which the effective potentials of the drift tubes depend on each other. Changing the trap depth via the voltages applied to DT3 and DT5 influences the potential of the central drift tube DT4 which in turn affects the beam energy. These effects can however be corrected for in the data analysis [26, 33, 34].

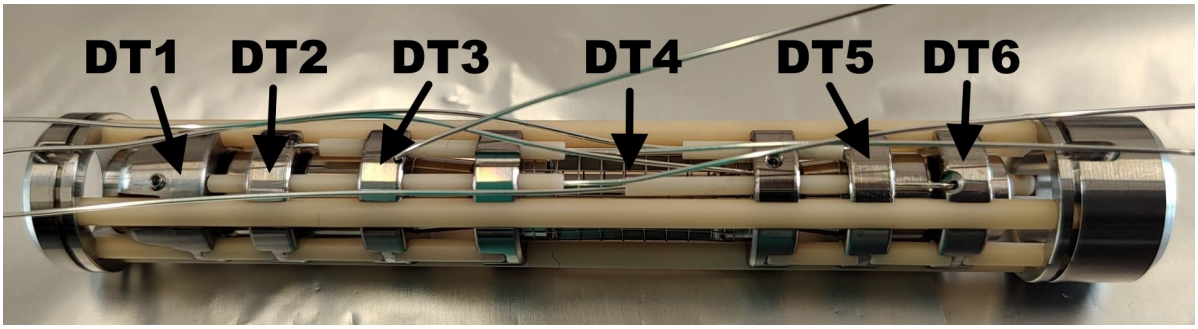

Figure 3.5: Drift tubes of the VAUQSI-EBIT that are identical in design to the ones installed in the PolarX-EBIT. The six titanium alloy drift tubes are fixed by alumina-ceramic rods and held into place by the two outer rings. The voltage of each drift tube can be set independently.

3.5 Collector

Before reaching the collector, the electrons pass a region at ground potential and are decelerated. The collector itself is on a ground potential and thus biased positively with respect to the cathode so that the electrons can reach it. At the collector, the magnetic field is much weaker than in the trap center, so that the force that compresses the electron beam decreases and the beam expands until the electrons impinge on the surface of the collector. Since the electron beam energy is deposited at the collector, it consists of copper and is water cooled. The deposited electron current can be measured to extract the transmission of the electron beam current[33].

3.6 Extraction

Two extraction electrodes are situated behind the collector that are negatively biased with respect to the cathode. This stops the electrons from hitting the walls of the machine, worsening the vacuum, producing dangerous radiation or damaging equipment downstream. The extraction electrodes can be employed to refocus the ejected ions. Behind the extraction electrodes, the ions reach the bender that consists of a curved inner and outer electrode. Voltages are applied to these components in order to bend the ion trajectory electrostatically at a 90° angle. Behind the bender, a Sikler lense refocusses the ion beam before it arrives at the channeltron [26, 33].

3.7 Detectors

The ions are detected at the end of the extraction beamline by a channeltron. When a particle impinges on the channeltron, secondary electrons are emitted from the surface material. These are accelerated towards the read-out electronics by a voltage applied across the channeltron. On their way, the secondary electrons impinge again on the surface and emit more electrons which results in an electron shower. The strongly amplified electron signal can be measured.

The photon emission of the ion cloud is detected by a silicon drift detector (SDD) that is mounted at one of the trap ports. Photons that reach the detector deposit their energy on the surface which results in the creation of electron-hole pairs in the high purity silicon material. The produced electron charge is proportional to the photon energy. A transversal electrical field is applied to the material and the charges drift towards a collection electrode. The built-in beryllium window was removed to allow for a shorter distance to the trap center and hence a larger solid angle and higher photon count. To block low energetic UV and visible light from saturating the detector, an aluminium filter of 500 nm thickness is mounted in front of the SDD. The signal from the detectors is processed by 13 bit analog-to-digital converters that have an input range of 0 to 10 V. The data acquisition is performed with the MPA4 system by FAST ComTec using the corresponding MPANT software to control the acquisition and display the data. The MPA4 system is a multiparameter multichannel analyzer that can register single events and events in coincidence. In addition, the data acquisition can be triggered by a single registered event [26, 32].

3.8 Measurement scheme

In order to determine the absolute resonance strengths, the number of ions, electron current density, line intensity and charge state distribution need to be known. For this, the electron and ion space charge have to be estimated which can be inferred from the x-ray spectrum that was recorded as a function of the trap depth and electron beam current. The DR resonances were recorded by varying the beam energy whilst keeping the trap depth and beam current constant.

As a first step, the ion charge was estimated with the bender serving as a Faraday cup. Then, the time-of-flight of the ions was recorded for various ramp times and trap depths. Both measurements were controlled by the DR server to operate the EBIT. Finally, the photon signal in the trap center and the time-of-flight signal were recorded for various electron beam currents, trap depths and electron beam energies to scan the DR resonances.

In the following, negative trap depths constitute a lower voltage on the central DT than the surrounding ones, whereas positive trap depths denote an inverted trap.

3.8.1 DR Server

The DR Server is a program that allows to control the charge trapping and breeding process inside the EBIT with a graphical interface. Function generators are programmed according to the parameters set on the interface, facilitating a straightforward application of the EBIT for simple measurements. The kick duration, ramp time, trap depth, lowest and highest energy of the scanning phase can be specified. The measurement scheme can be seen in Figure 3.6.

The cathode is set to a fixed voltage. DT3, DT4 and DT5 are biased together with a triangular wave function that continuously ramps up and down the specified energy range as seen in the blue and red line in Figure 3.6. The ramp time specifies the period of the triangular wave function. DT3 and DT5 are additionally biased with the trap depth as seen in the offset in the figure. The ions are kicked out of the trap at the end of the ramp time (green) by triggering the fast switch BEHLKE for a specified kick duration which additionally biases DT4 with a high voltage, inverting the trap.

3.8.2 Estimating the ion charge with the bender

As an independent measurement of the absolute ion charge, the outer bender can be used as an improvised Faraday cup. For this, an oscilloscope is connected to the outer bender with a short cable in order to keep the parasitic capacitance low. The inner bender was first set to ground. However, as the outer bender has a cut-out on the beam axis for the photon beam, some of the ions traversed the bender without hitting it. To offset this problem, a positive voltage was applied to the inner bender to deflect the particle trajectories until the signal from the outer bender reached maximal saturation. This was achieved at a voltage of 400 V. The measurements were controlled with the DR Server and performed for various ramp times and trap depths. The kick duration was set to 400 ns and electron beam energy to 800 eV. The signal from the oscilloscope was read out 11 times and the average of these measurement was recorded.

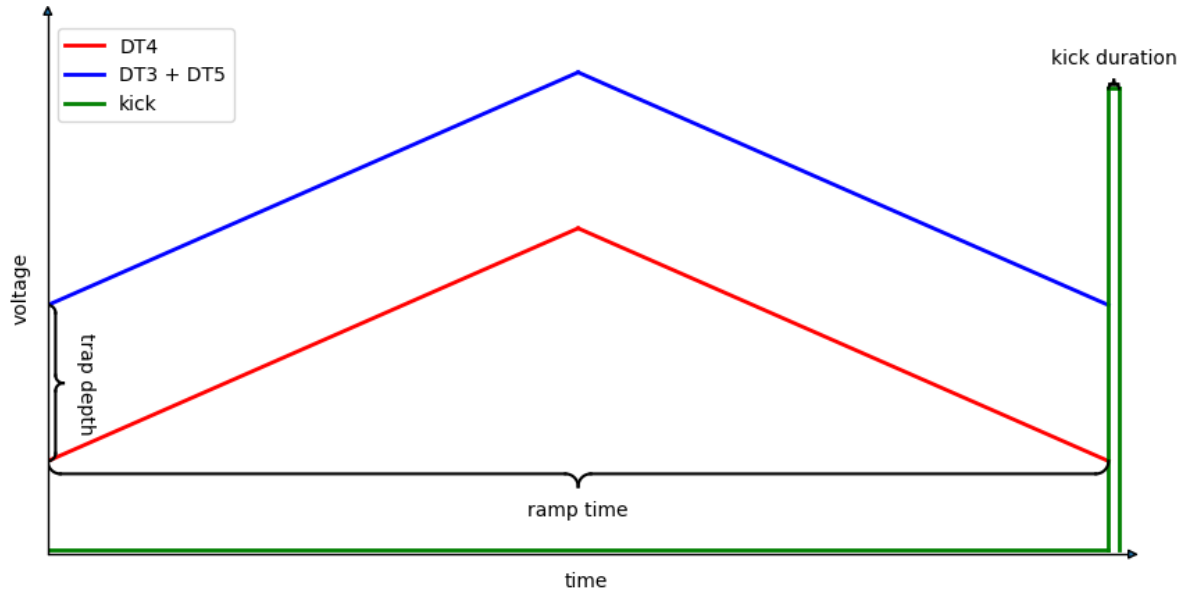

Figure 3.6: Measurement scheme of the DR server. The voltage signal is ramped up and down for DT3, DT4 and DT5. DT3 and DT5 are additionally biased by the trap depth. At the end of the ramp time, the ions are kicked out of the trap.

3.8.3 Time-of-flight scans

To probe the charge state distribution inside the EBIT, time-of-flight (ToF) measurements were performed with the DR server for different ramp times and trap depths. This was done for a kick duration of 400 ns and an electron beam energy of 800 eV. The signal on the channeltron was recorded by the oscilloscope with the kick-voltage serving as the trigger. For each measurement, 10 scans were averaged.

3.8.4 Measurement of the DR resonances

To measure absolute cross sections of the He-like oxygen DR resonances, the photon signal was recorded for varying trap depths and electron beam currents with the SDD at the trap center. The scan utilised two function generators with two different outputs each, so that in total four different voltage signals could be provided. The voltages of the drift tubes were set in discrete steps and amplified by a factor of 400, so that the values set by the function generators only had to be a fraction of the desired voltages. The measurement scheme is depicted in Figure 3.7.

Before each scan, an electron beam current was set manually. Then, the offset between DT3 and DT5 (blue) to DT4 (red) was fixed to the trap depth. For each trap depth, the electron beam energy was interated between 400 eV and 800 eV. For this, a DC signal is applied to the drift tubes DT3, DT4 and DT5 which is changed by 0.1V in each step with an additional DC bias for DT3 and DT5 to set the trap depth. The cathode was supplied with -200 V which

results in a voltage of 200 V to 600 V for the drift tubes to achieve the desired nominal beam energies. To keep track of the electron beam energy, a corresponding DC function (black) with a voltage on a discrete linear scale of 0.1 to 4.5 V was fed into the MPA system. After setting the trap depth and the electron beam energy, the program pauses for 0.1 s to acquire the photon signal. Then, it triggers the pulse so that the ions are kicked out of the trap. The consequent time-of-flight signal was recorded with the oscilloscope and the next electron beam energy is set. The full scan of each current was repeated three times to achieve sufficient statistics.

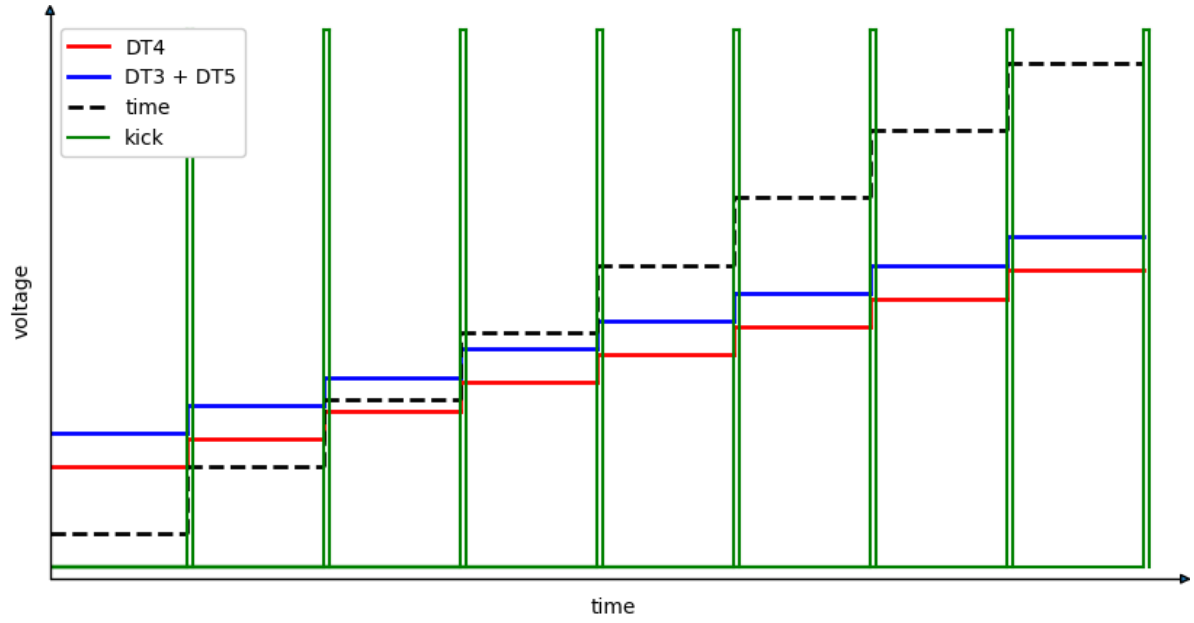

Figure 3.7: Measurement scheme for the DR resonances. The voltages are set in discrete steps. The drift tubes DT3, DT4 and DT5 are ramped up for the desired energy range with an addition offset to DT3 and DT5 for the trap depth. A discrete time signal is sent to the MPA system to indicate the set electron beam energy value. At the end of each step, the ions are kicked out of the trap and the time-of-flight is measured by the oscilloscope.

4 Data analysis and results

At the beginning, the ion charge inside the trap was estimated with the bender for various ramp times and trap depths. In a second step, the charge states in the trap were identified with a time-of-flight measurement. The photon signal was recorded for different beam currents, trap depths and electron beam energies and the K_α photons are selected from these measurements. By fitting the DR resonances in the spectra, the ion and electron space charge are determined. From this, the compensation of the electron beam by the ions and the resonance positions without the space charge is calculated. The charge state distribution in the trap is estimated from the time-of-flight signal. In a next step, the electron current density, number of ions and overlap factor are determined. By fitting the resonances, the line intensities are determined. With these parameters, the resonance strengths are calculated and compared to the theory.

4.1 Estimating the ion charge using the bender

As described in section 3.8.2, the ion charge inside the trap was estimated for various ramp times and trap depths by employing the outer bender as a makeshift Faraday cup. The outer bender and the oscilloscope can be treated as an RC circuit with the ion charge q_i being deposited on the bender as a result of the ions being kicked out of the trap. The coaxial cable connecting the oscilloscope and the bender serves as a capacitor with the capacity C, whilst a resistor of the resistance $R = 1\,\mathrm{M\Omega}$ is integrated into the oscilloscope. Owing to the ions impinging on the outer bender, a voltage V_0 is built up in the coaxial cable with

$$V_0 = \frac{Q_i}{C}. \tag{4.1}$$

The voltage decays exponentially as a result of the discharge over the resistor according to

$$V(t) = V_0 \cdot \exp\left(-\frac{t}{\tau}\right), \tag{4.2}$$

where t is the passed time and τ is the RC time constant with

$$\tau = RC. \tag{4.3}$$

The error of the oscilloscope signal was estimated as the standard deviation of the signal before the ions hit the bender and amounts to $58.3\,\mu\mathrm{V}$ for each measured voltage. Due to the low signal, the data appears to be quite noisy. The signal uncertainty is taken into consideration as a weight for each fit.

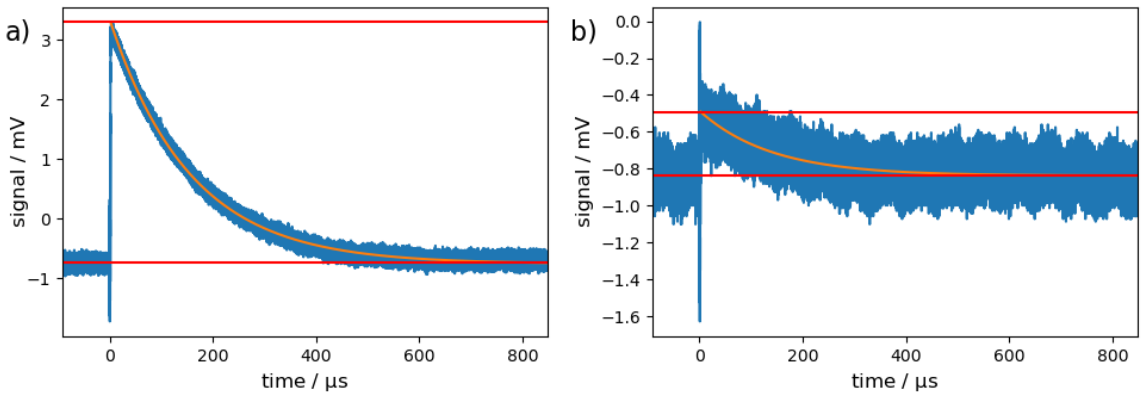

Figure 4.1: Two examples of the fit for the ion charge. The signal (blue) is fitted with an exponential function (orange). The red lines mark the upper and lower boundary for the voltage V_0. For the sake of clarity, the error of the data is not shown. a) Ramp time of 1.0 s and trap depth of -35 V. b) Ramp time of 0.01 s and trap depth of 30 V.

The RC time constant τ is determined by fitting the exponential equation 4.2 to each measurement. An offset b of the voltage is taken into account. Since there is a small offset t_0 between the trigger and the peak value of the signal, V_0 is not a good measure for the height of the signal. Instead, the lower voltage is determined by fitting a constant function to the signal before the ions arrive, whilst the peak voltage is calculated as the value of the exponential fit at the point where the signal reaches saturation. The difference between these two points gives the signal height with its standard deviation propagated from the uncertainties of the fits. Two examples for the performed fits can be seen in Figure 4.1.

In a next step, the RC time constant τ is calculated from the fits. Given that τ only depends on the resistance R and the capacity C of the experimental set-up, it is expected to be independent of the ramp times and trap depth. Since the signal is small for inverted traps and very short ramp times, τ shows larger fluctuations for these parameters. For the final value of τ, the fitted τ values are hence averaged for ramp times larger than 0.002 s and trap depths deeper than 5 V. The uncertainty is taken from the standard deviation of the average. τ is estimated as (162.4 ± 3.3) µs. Using equation 4.3, the capacity C follows as (162.4 ± 3.3) pF. With this value, the ion charge Q_i is calculated according to equation 4.1 from the peak voltage V_0 for each measurement. The result can be seen in Figure 4.2.

The upper panel of Figure 4.2 shows the total ion charge as a function of the ramp times. For short ramp times, the trap is empty resulting in a very low measured charge. The ions are then sequentially ionised by the electrons leading to an increase of the ion charge with the ramp times. This increase reaches saturation after approximately 10-30 ms, since the ions reach their equilibrium distribution where ionisation and recombination processes are in balance. If the maximum ion charge is lower, equilibrium is reached faster.

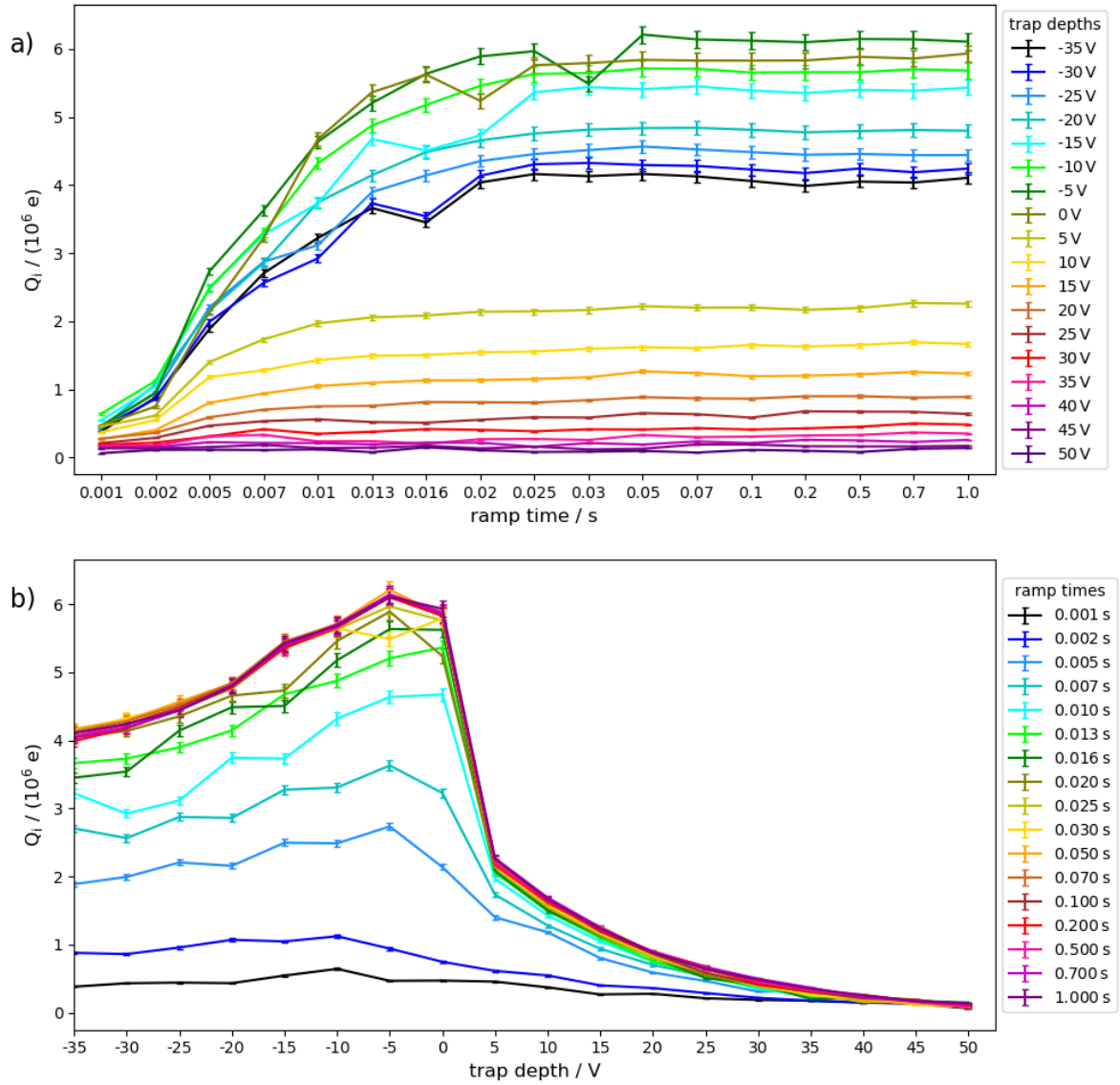

Figure 4.2: Total ion charge as measured by the bender. a) As a function of the ramp times with a different line for each trap depth. b) As a function of the trap depth with each line marking a different ramp time.

The lower plot in Figure 4.2 showcases the total charge depending on the trap depth for different ramp times. At highly inverted trap depths, almost no ions are confined, resulting in a low ion charge. When the inverted trap turns to to a potential well, ions can be confined and the trapped charge rises rapidly until it decreases again for deeper traps. A possible reason for the decrease could be that the conditions within a deeper trap might not be optimal for confinement. The ion temperature rises with the trap depth and more ions might be able to escape. An approximation of the ion temperature is given by equation 2.15.

The ion charge for optimal trapping conditions at sufficiently long ramp times is approximately $(6.1 \pm 0.1) \cdot 10^6\, e$. However, it is not known what percentage of the ejected ions hit the surface before reaching the bender and how many still pass through the slit in the bender as seen in Figure 3.1 and are therefore not detected. The calculated ion charge thus serves as an lower limit on the total trapped charge.

4.2 Time-of-flight data

The charge states inside the EBIT were identified with a time-of-flight (ToF) measurement as described in section 3.8.3. The ToF peaks were recorded with an oscilloscope for different ramp times and trap depths. Equation 2.22 takes the two parameters t_0 and $L/\sqrt{2U_{\mathrm{acc}}}$ to translate between the charge-to-mass ratios q/m and the flight duration t_{ToF}. L is the path length from the trap center to the detector, U_{acc} the accelerating voltage and t_0 is the offset to the trigger of the oscilloscope. Both parameters are expected to be constant if the experimental setup is not changed during the measurement. By determining the parameters for one data set, the charge states in the remaining measurements can be calculated. Since the ion population in the trap has reached saturation after 0.05 s according to Figure 4.2, a data set with a ramp time of 0.5 s is used for the calibration. The signal was summed over all trap depths and can be seen in Figure 4.3.

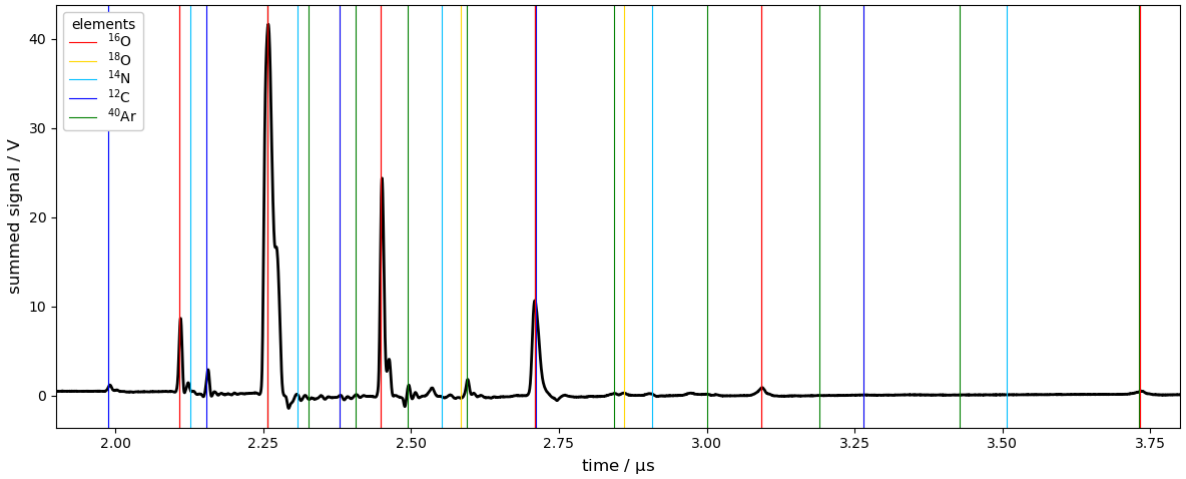

Figure 4.3: Calibration of the charge states. The data (black) is recorded with the oscilloscope for a ramp time of 0.5 s and summed up for different trap depths. The vertical lines represent the flight duration for the charge states as calculated using the calibration from equation 2.22. Each color represents a different element. The parameters that are required to calculate the flight duration are based on the assumption that the largest time-of-flight peak belongs to helium-like oxygen.

It was assumed that the EBIT is filled with residual gas that is ionised and trapped. The main components of air are ^{16}O, ^{14}N, ^{40}Ar and ^{18}O. In addition, there might also be carbon ^{12}C. For these elements q/m is known. The parameters t_0 and $L/\sqrt{2U_{\mathrm{acc}}}$ are adjusted until the elemental lines match the peaks seen in Figure 4.3. It is assumed that the largest peaks belong to oxygen since it is the second-most abundant component of air and much easier to trap then nitrogen. This leads to $t_0 = 242.6\,\mathrm{ns}$ and $L/\sqrt{2U_{\mathrm{acc}}} = 12.1 \cdot 10^{-3}\,\mathrm{m}/\sqrt{\mathrm{V}}$ as a first estimate.

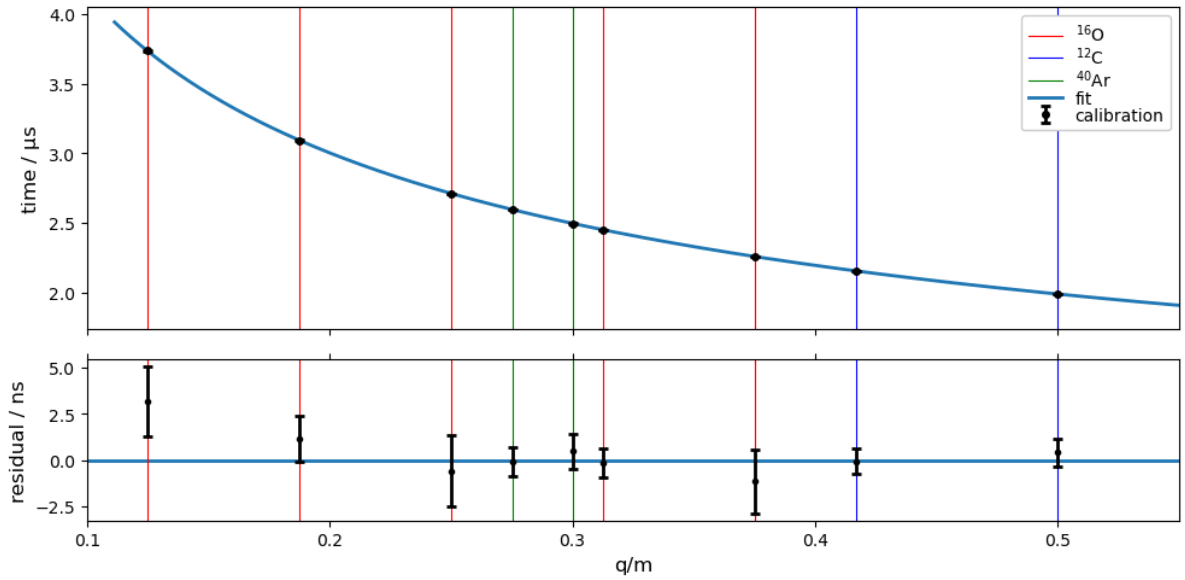

Figure 4.4: Fit of the calibration peaks with equation 2.22 to determine t_0 and $L/\sqrt{2U_{\mathrm{acc}}}$. The upper plot shows the fit to the Gaussian center of the peaks, the lower plot the residuals. The element lines are taken from the first approximate calibration.

With this identification of the peaks, the parameters t_0 and $L/\sqrt{2U_{\mathrm{acc}}}$ can be further calibrated. For this, the peaks in Figure 4.3 are fitted with a Gaussian distribution. The peaks that can be clearly attributed to a q/m value through the first estimation are taken as calibration points to refine the parameters. The strong ^{16}O peaks and two of the ^{12}C and ^{40}Ar peaks are used for the calibration as depicted in Figure 4.4. The flight duration and its uncertainty for each peak are determined from the Gaussian fit and plotted in Figure 4.4. With these points the parameters can be determined by fitting equation 2.22. This results in $t_0 = (250.05 \pm 1.69)\,\mathrm{ns}$ and $L/\sqrt{2U_{\mathrm{acc}}} = (17.09 \pm 0.01)\,\mathrm{m}/\sqrt{\mathrm{V}}$. The residuals of the fit match within their standard deviation.

Using the calibration curve shown in Figure 4.5, the q/m values of the uncalibrated data points can be determined. Additional lines for ^{18}O, ^{40}Ar and possibly ^{12}C can be identified. However, not all fitted peaks correspond to a charge state. It might be that these belong to other elements inside the trap. Another possibility is that they originate from electronic artefacts, mainly the ringdown from the electronics. This effect is discussed further in [35]. The ringdown is also visible in Figure 4.3 after the most prominent peaks.

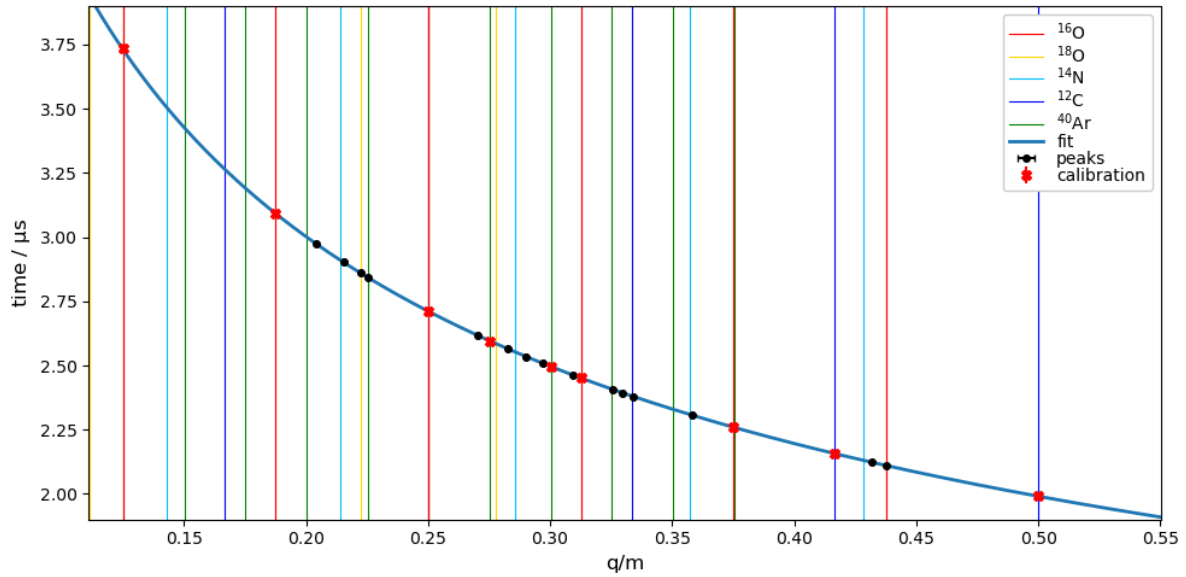

Figure 4.5: Charge state calibration. The q/m value of the ions that are assumed to be in the trap are marked with colored vertical lines and the fitted calibration curve is drawn in blue. The peaks used for the calibration are marked in red. The q/m values of the uncalibrated peaks that are depicted in black are predicted by the calibration curve. A peak is assumed to be attributed to a charge state if it overlaps with the vertical q/m line of that specific state. Not all charge state lines are visible since lines with the same q/m ratio overlap.

With the estimated values of t_0 and $L/\sqrt{2U_{\text{acc}}}$, the charge states in the other ToF measurements can be identified. Figure 4.6 shows two examples for the charge state identification. Oxygen is the dominant element in the trap. It is ionised up to hydrogen-like oxygen ^{16}O. For deep traps and long ramp times, helium-like oxygen yields the dominant contribution. Other important elements in the trap are ^{14}N, ^{12}C and ^{40}Ar.

The upper plot of Figure 4.6 depicts the change of the ion population with the trap depth for a fixed ramp times of 0.2 s. It can be seen that the trap is almost empty for strongly inverted traps as the ions are not confined inside a potential well. The ion content then increases with the trap depth and even for inverted traps ions can be confined. For a deep trap, the ion content hardly changes.

The lower plot in Figure 4.6 depicts the ion content for a fixed trap depth of -10 V and varying ramp times. At short ramp times, the charge state distribution mainly consists of the lower charge states O^{4+}, O^{3+} and O^{2+}. As the ramp time rises, the charge state distribution shifts to the higher charge states O^{6+} and O^{5+} and the contribution of the lower charge states decreases rapidly. At long ramp times, hydrogen-like oxygen can be observed, although helium-like oxygen remains the dominant ion and the contribution of helium-like carbon shifts to hydrogen-like carbon. More ToF scans can be found in Figures 6.1 to 6.4 in the appendix.

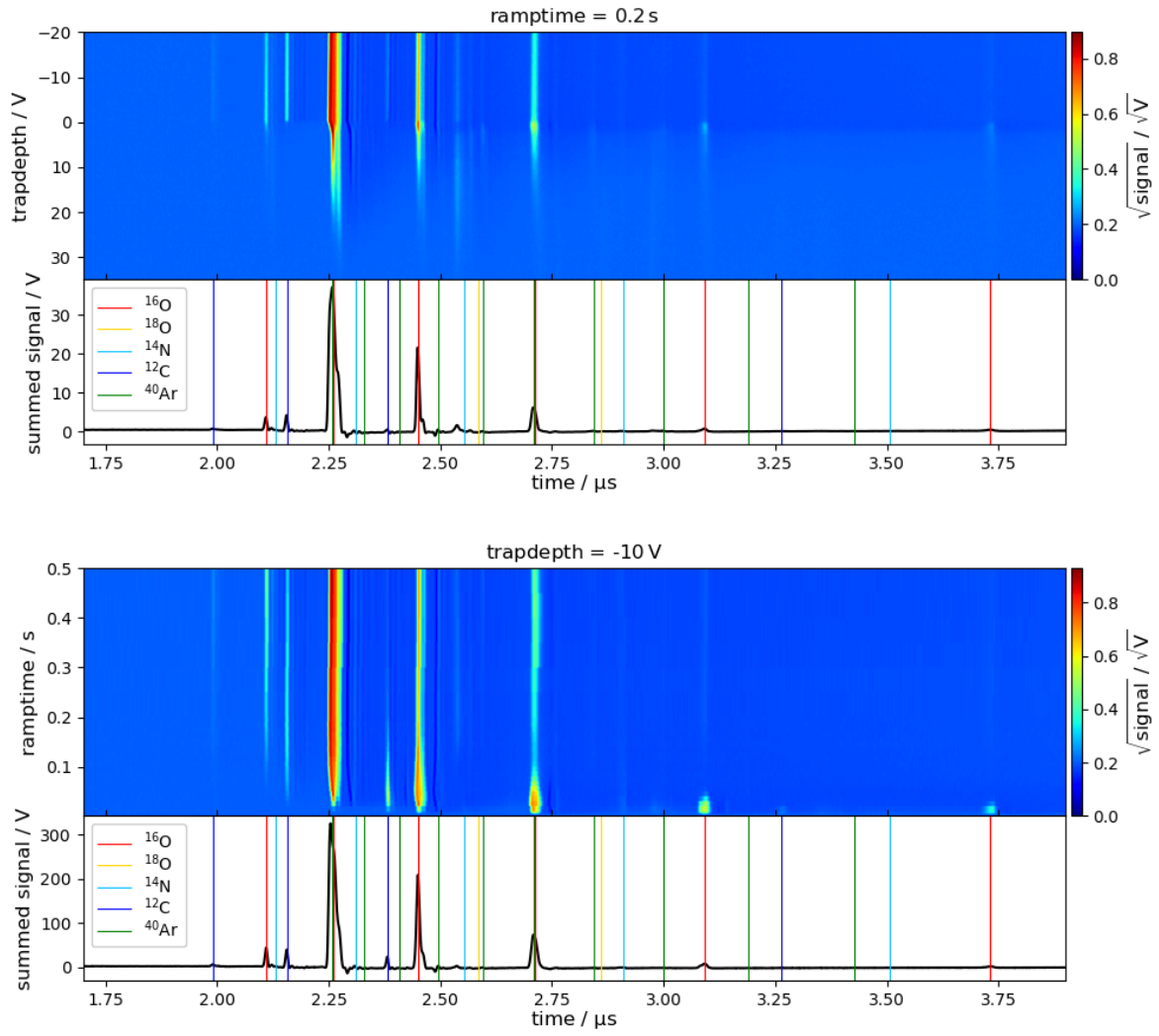

Figure 4.6: ToF scans. The upper half of the plots depicts the ToF signal for a fixed ramp time of 0.2 s and varying trap depths (top) and for a fixed trap depth of -10 V and varying ramp times (bottom). For better visibility, the square root of the signal is shown. The lower plots display the summed signal (black) and the ToF lines for different ions (colored) similar to Figure 4.3. The ion lines are calculated using the parameters estimated in section 4.2. At a fixed ramp time, the trap is almost empty for strongly inverted traps, whilst at a fixed trap depth, the ions move to higher charge states as the ramp time increases.

4.3 X-ray fluorescence data

The MPA system measures the photon energy for each photon event detected by the SDD in coincidence with the electron beam energy, encoded via an analog voltage. It saves the voltage signal into a channel proportional to the input. Thus, both the electron energy and photon energy values are displayed in terms of channels and need to be calibrated.

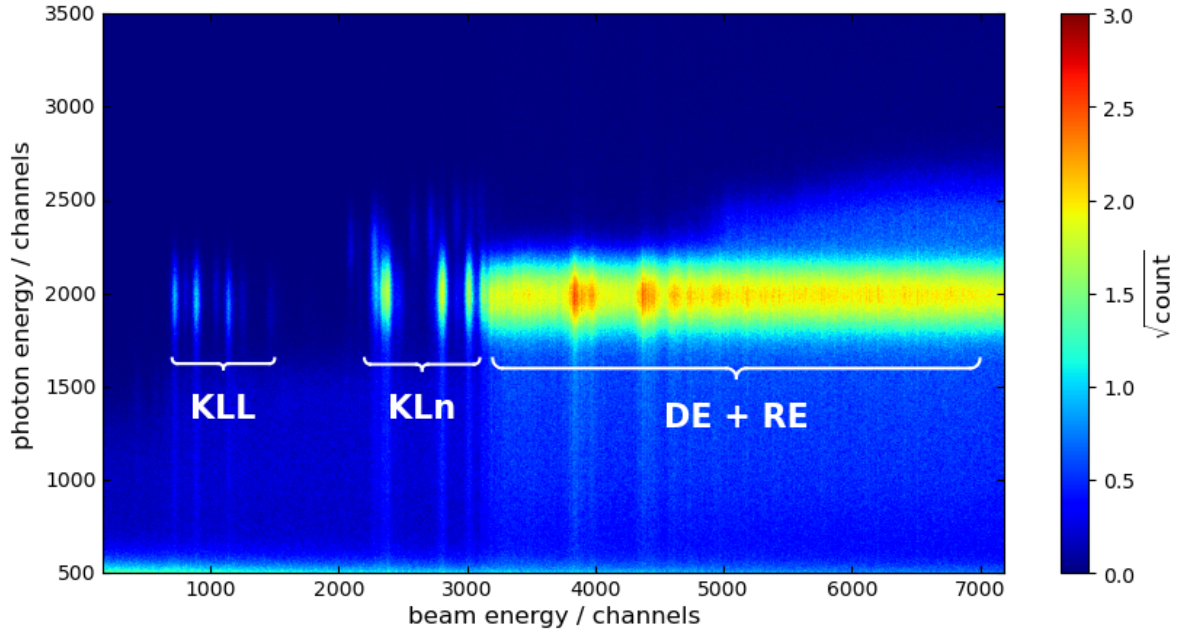

Figure 4.7: Photon count as a function of the uncalibrated beam energy and photon energy for an electron beam current $I = 1.44\,\mathrm{mA}$ and a trap depth $V_T = -13\,\mathrm{V}$. The beam energy and photon energy scale linearly with the channel number. For a clearer depiction of the DR resonances, the square root of the photon count is depicted. The KLL and KLn for n $\geq$ 3 DR signal are marked in the plot as well as the direct (DE) and resonant (RE) excitation.

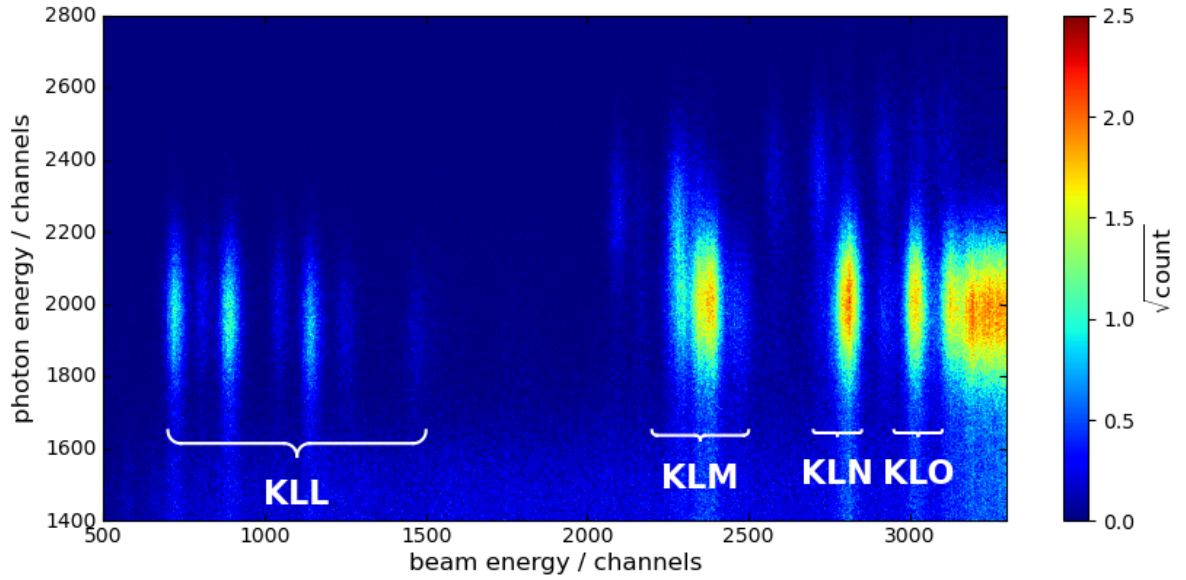

Figure 4.8: Enlarged view of Figure 4.7. The KLn dielectronic recombination signals are marked in the plot.

An example for the photon signal can be seen in Figure 4.7 with an enlarged view in Figure 4.8. The K_α photon emission by the radiative decay of an L-shell electron to the K-shell can be seen at a photon energy channel of about #2000. In the figures, the KLL, KLM, KLN and KLO dielectronic recombination is marked. Due to detector artifacts, the resonance appear smeared out in the photon energy. The direct and resonant excitation can be seen as a brightly colored band where an electron from the lower shell is either resonantly or non-resonantly excited from the K-shell to the L-shell and then decay radiatively.

This work only concerns itself with the DR resonances that involve the emission of a K_α photon. The data analysis was therefore performed on the K_α slice of the photon energy data as shown in the upper plot of Figure 4.9. The same slice was taken for each measurement. The photon count was summed along the photon energy axis to get the processes that involve K_α emission as a function of the uncalibrated electron beam energy. An example for the resulting summed count can be seen in the lower plot of Figure 4.9.

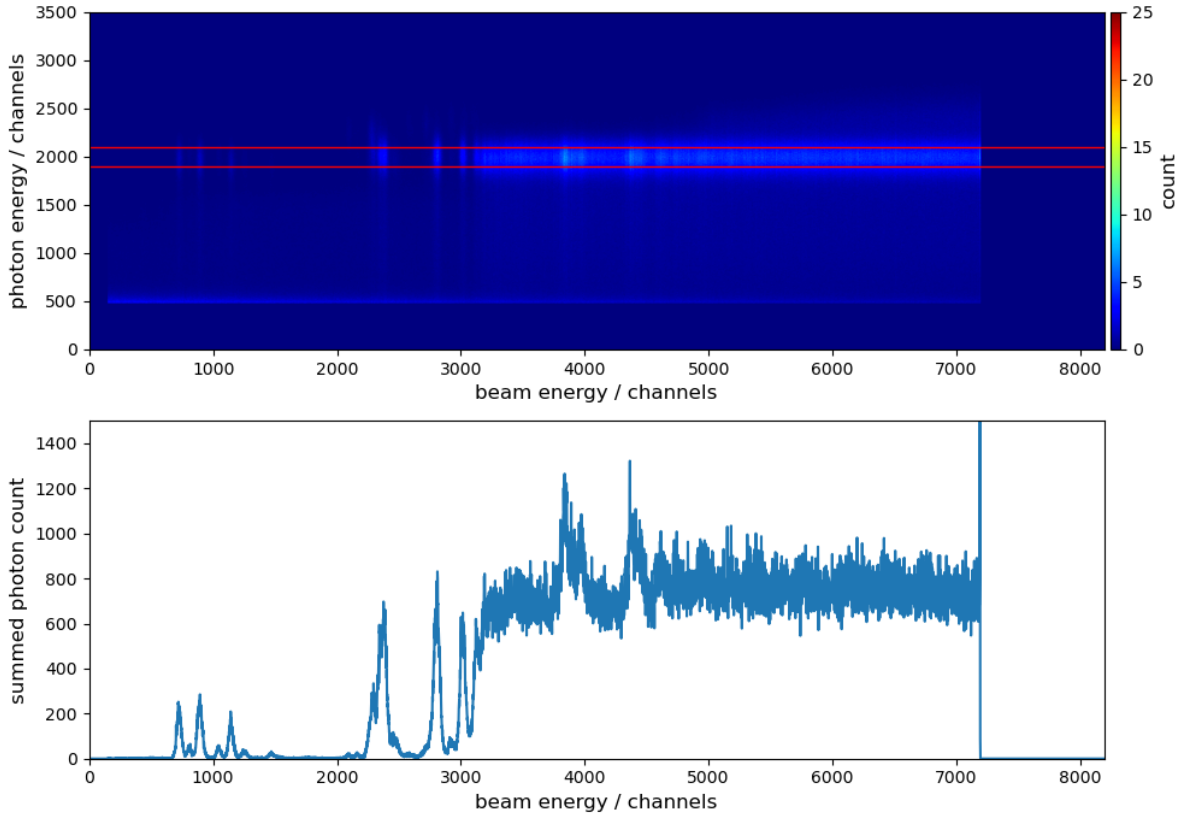

Figure 4.9: Processing of the photon signal for $I = 1.44\,\mathrm{A}$ and $V_T = -13\,\mathrm{V}$. Top: A slice of the photon energy (red) for the K_α photon signal is selected. Bottom: The slice is summed along the photon energy axis and displayed as a function of the beam energy for further analysis of the resonance peaks.

For the following data analysis, the electron beam signal has to be calibrated in units of eV to represent the energy. The nominal beam energy determined by the voltage difference between the cathode and DT4 was set in steps of 0.1 eV between 400 V and 800 V. The target voltages are divided by 400, produced with a function generator and then amplified with a Trek 677B amplifier by a nominal factor of 400. To estimate the actual gain factor of the amplifier, the voltage difference between the cathode and DT4 was measured with a multimeter whilst varying the set voltages via the control system. This measured amplification factor is (399.17 ± 0.09) with an additional offset of (320 ± 88) mV and the voltage difference is hence set between (399.49 ± 0.31) V and (798.65 ± 0.34) V.

To calibrate the data, the recorded analog voltage is scaled to the nominal electron beam energy. The electron beam signal varies between 0.1 V and 4.5 V, but the MPA system has an acceptance of 0 V to 5 V, so the electron beam signal does not extend over the whole channel range. This is taken into account for the boundaries of the calibrated electron beam signal and can be seen in the margins of Figure 4.9.

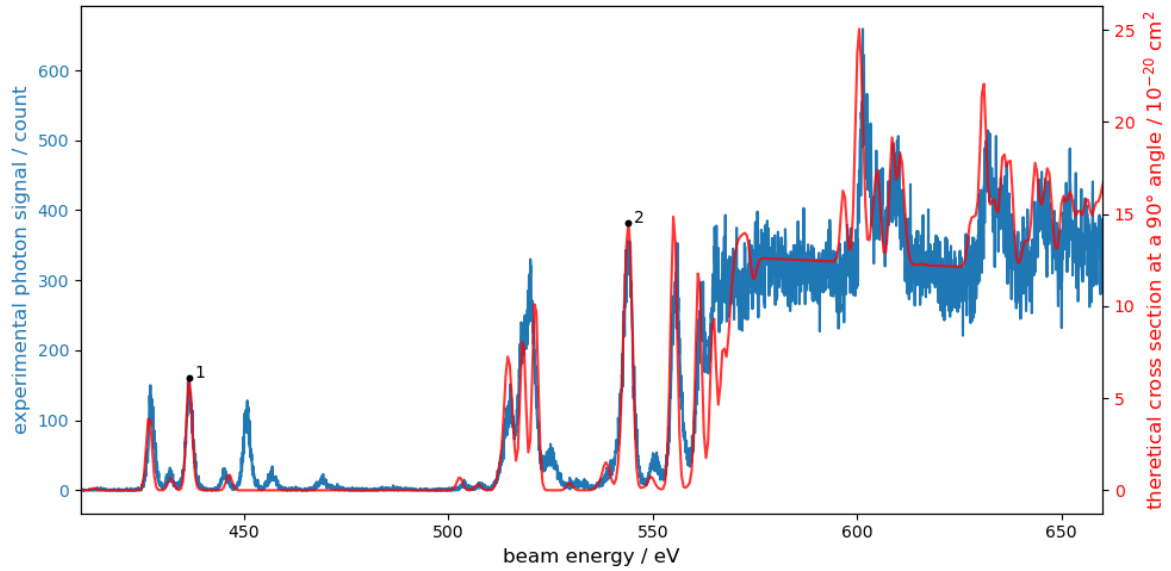

Figure 4.10: Comparison of the experimental photon count for the electron beam current $I = 0.99$ mA and trap depth $V_T = -4$ V (blue) to the theoretical resonance strengths of helium-like oxygen at an angle of 90° to the beam axis (red). The marked peaks were taken as reference points to scale the experimental electron beam energy.

The theoretical resonance strengths for helium-like oxygen were calculated with Flexible Atomic Code (FAC) and are depicted as the red line in Figure 4.10. The polarization effect at 90° angle to the beam axis are taken into consideration in the calculation. For a quick comparison between the recorded data and the theory, the two peaks marked in the figure were fitted with a Gaussian function. The experimental data was then scaled according to the peak centers. All resonances present in the theoretical data seem to be in good agreement with the

experimental data. However, some peaks are not reflected in the theoretical data and hence originate from different charge states, most likely lithium-like and beryllium-like oxygen. Since the calculations for the polarization factor P get increasingly complex when more electrons are involved, the theoretical resonance strengths at 90° were only calculated for the helium-like system.

4.4 Determining the space charge

The space charge shifts the resonance energies according to equation 2.14 relative to the nominal beam energy. A change in the trap depth alters the ion content inside the trap and thus the ion space charge, whilst a change in the electron beam current alters the electron current density and thus the electron space charge. The DR resonances were measured for varying trap depths and electron beam currents to infer the ion and electron space charge. To achieve this, the resonance peaks were first fitted with Gaussian distributions to determine the resonance energies. The resonances are ordered into lines as seen in Figure 4.12 that show the energy shift as a function of the trap depth for the different electron beam currents. For the further analysis, the resonance energies have to be corrected for the reach-through effect of the drift tubes as described in section 3.4. The ion space charge is calculated from the shift of the resonance position between the measurements with an empty and a full trap for different electron currents. The electron space charge is determined from the shift of the resonance positions in an almost empty trap for different beam currents.

4.4.1 Fitting the spectral lines

In a first step, the resonance positions have to be determined for the varying recorded trap depths and electron beam currents. The focus was put on ten isolated and strong resonances. The selected peaks are marked in Figure 4.11. Each peak was identified with a peak-finding algorithm. Once identified, a Gaussian distribution was fitted to the data in a region of interest around the selected peak. For each measurement, the fitted Gaussian peaks were attributed to a certain resonance and ordered into corresponding lines for the varying trap depths. An example for the lines can be seen in Figure 4.12. The fitted resonance lines for all currents are depicted in Figures 6.5 and 6.6 in the appendix.

The drift tubes of the EBIT are subjected to electrostatic reach-through as described in section 3.4 and the data has to be corrected for this effect. The left plot in Figure 4.15 depicts the position of the first resonance line for different electron beam currents as a function of the trap depth V_T. Three distinct regions are marked in the figure.

The first section is in the regions of deep traps and shows a linear shift to higher resonance energies for deeper traps. This might be due to the increase of the ion temperature with the trap depth as described by equation 2.15. At higher temperatures, more ions can escape the trap and

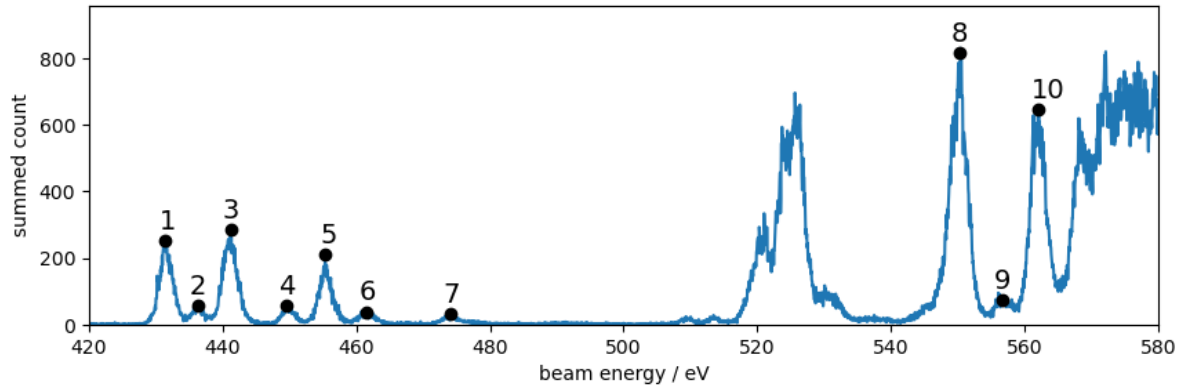

Figure 4.11: Summed photon count for the K_α emission as a function of the electron beam energy for the electron beam current $I = 1.44\,\text{mA}$ and trap depth $V_T = -9\,\text{V}$. The resonances that are used in the following data analysis are marked in black.

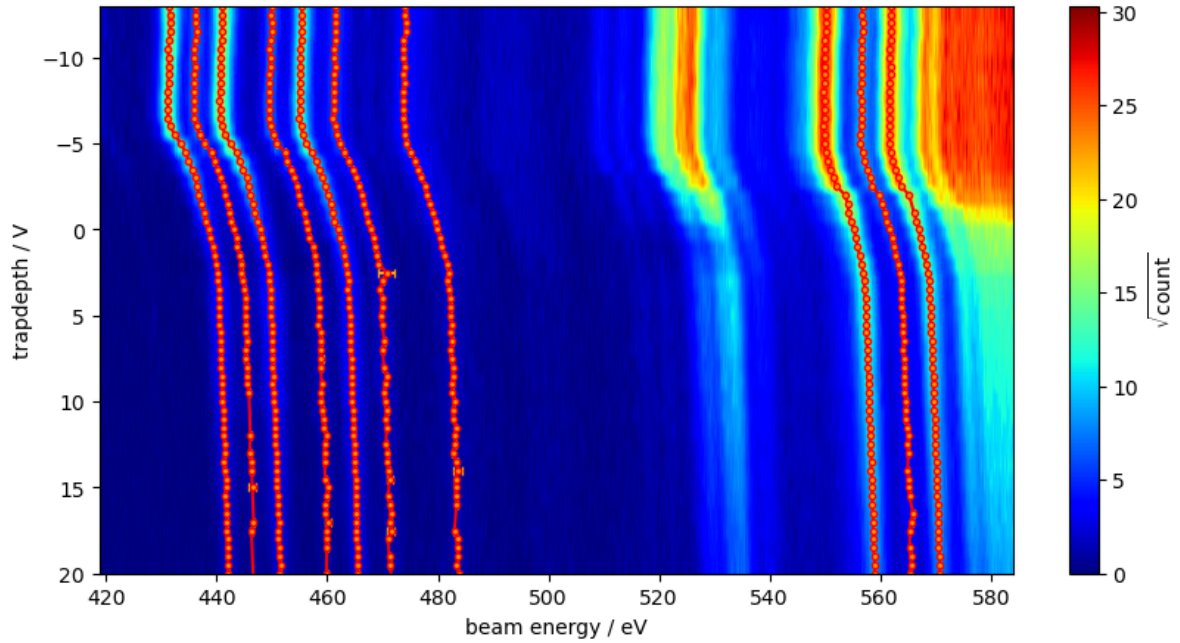

Figure 4.12: Summed photon count for the K_α emission as a function of the electron beam energy and the trap depth for a beam current of $I = 1.44\,\text{mA}$. Ten resonances were selected, fitted with a Gaussian distribution for each trap depth and ordered into lines. The center of the Gaussian functions are marked in red. The square root of the count is shown for better visibility.

the ion space charge decreases. Hence, the effective electron beam energy decreases according to equation 2.14 and shifts the observed resonance positions to higher nominal electron beam energies. Therefore, an optimal trap depth seems to exist that results in maximal ion space charge and thus a minimum in the observed resonance energies.

In the second section the nominal resonance energies rapidly move to higher energies as the trap changes from a deep to an inverted trap. In shallower traps, ions can more easily escape the confinement axially resulting in a reduction of the ion space charge and an increase in the observed beam energy.

The third region depicts the resonance positions for an almost empty trap. The space charge contribution of the ions is negligible and the resonance positions are expected to be constant. However, they still shift to higher energies for higher inverted traps since the relative voltage difference of DT3 and DT5 to DT4 influences the effective voltage $V_{\mathrm{DT4,eff}}$ of DT4. This effect is believed to be linear with

$$V_{\mathrm{DT4,eff}} = V_{\mathrm{DT4}} + c \cdot V_T, \tag{4.4}$$

where c is the voltage change of DT4 with the trap depth V_T. To correct for $c \cdot V_T$ the resonance positions in the third region can be fitted with a linear function. The fit of the first resonance is shown in Figure 4.13 for the different electron beam currents. The slope c of the fitted lines can be seen in Figure 4.14 as a function of the electron beam current. The slope seems to increase slightly with the current. This might be due to the increased electron space charge that additionally shifts the resonances to higher energies. Since this effect only has a small influence on the slope, it was disregarded. The shift per trap depth c is calculated as the weighted average of all fitted lines and amounts to $c = (0.11 \pm 0.02)$ eV/V. The shift is marked in black in Figure 4.14.

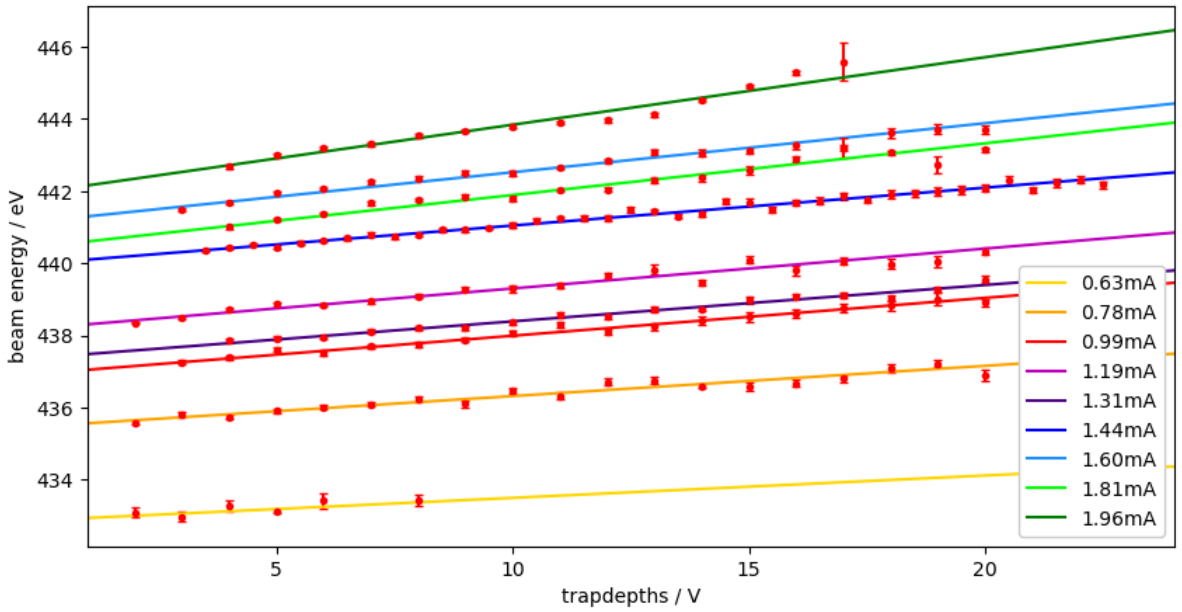

Figure 4.13: Linear fit to the positions of the first resonance as a function of the trap depth for various electron beam currents in the third regions as defined in the main text. Each line represents a different electron beam current.

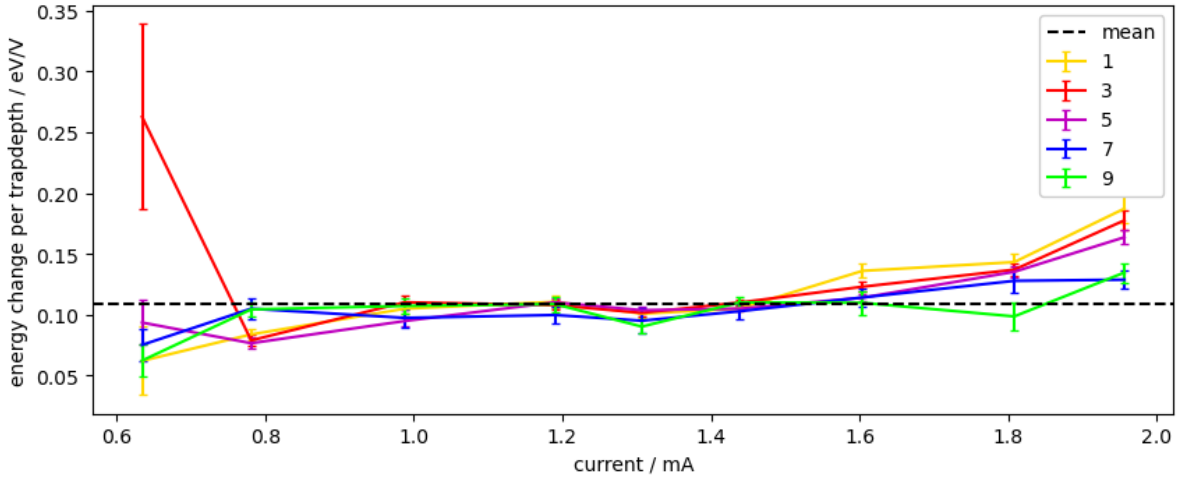

Figure 4.14: Slopes of the linear fits as seen in Figure 4.13 as a function of the electron beam current. Each color represents a different resonance with the weighted average of all resonances being marked in black. For the sake of clarity, only a selection of the resonances are shown.

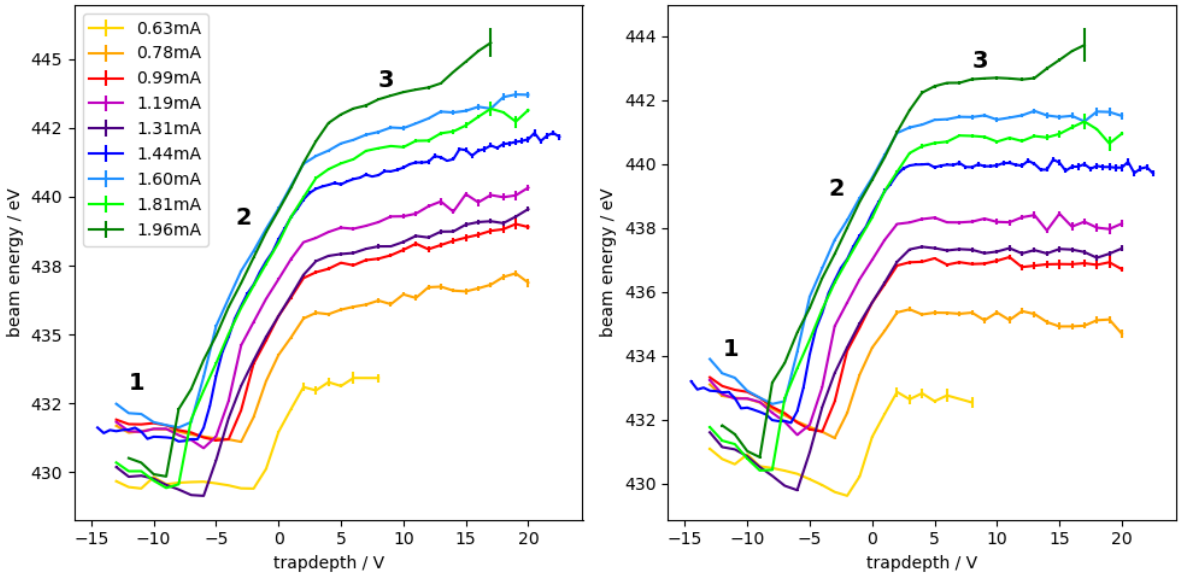

Figure 4.15: Fitted positions of the first resonance as a function of the trap depth. Each line represents a different electron beam current. The three different regions are marked in the plot. Left: Resonance energies before the correction for the reach-through effect. Right: Corrected resonance energies.

To correct for the reach-through effect, the shift $c \cdot V_T$ has to be subtracted from all resonance positions. The new line positions of the first resonance can be seen in the right plot of Figure 4.15. The resonance positions are now constant in the third section, whilst the slope of the first section is steeper. The uncorrected and corrected resonance lines for all resonances are depicted in Figures 6.7 and 6.8 in the appendix.

Since the ion content in the trap changes, the three sections are expected to be visible in the resonance intensity. The intensity was approximated by the area of the fitted Gaussian distribution. The resulting integrated count for the first resonance can be seen as a function of the trap depth in Figure 4.16 for the different electron beam currents. At deeper trap depths, the intensity is high and seems to be constant as the trap is essentially full. For shallower traps, the intensity rapidly decreases as the trap empties itself until it is almost zero. In addition, the intensity grows with the beam current due to the higher current density in the center of the trap and thus the higher recombination and excitation rate. The discussed behavior is depicted for all lines in Figure 6.9 in the appendix.

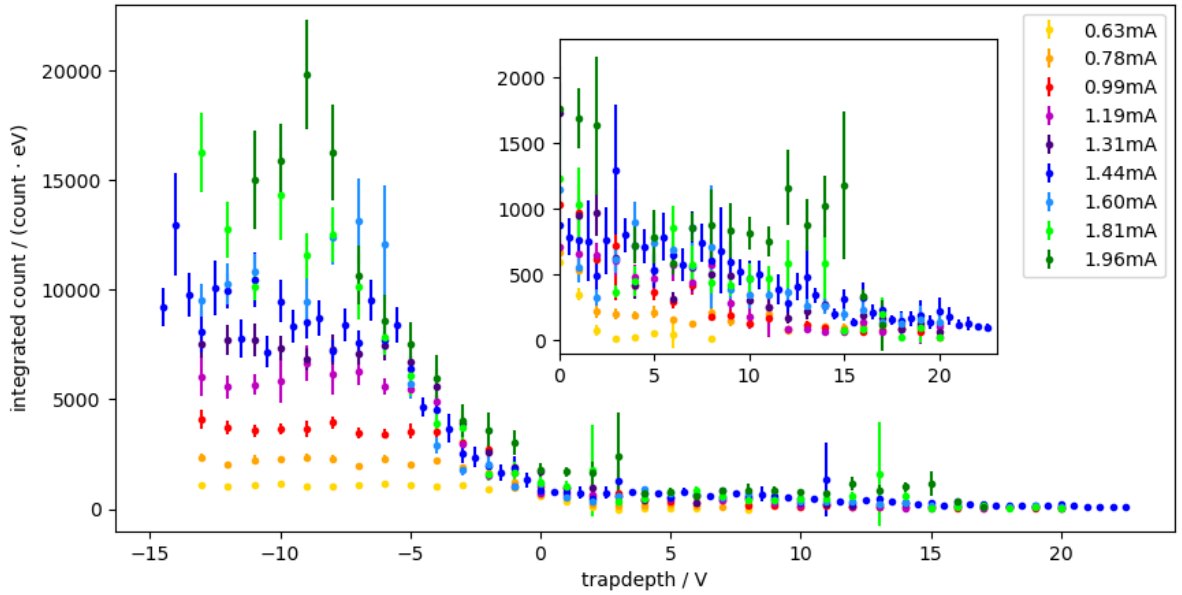

Figure 4.16: Area of the Gaussian function fitted to all resonance peaks as a function of the trap depth. Each color represents a specific electron beam current. An enlarged view of the data for trap depths higher than 0 V is displayed as an inset.

4.4.2 Ion and electron beam space charge

To calculate the space charge, the resonance positions for a full and an empty trap have to be determined. The first intersection between the deep and the shallower trap gives the resonance position for a full trap, the second intersection between the shallow and the inverted trap leads to the resonance position for an empty trap.

To determine the intersections, the first and third section were fitted with a linear function. The transition point from the first to the second section is estimated as the minimal observed resonance energy at which the ion content in the trap is maximal. The point at which the data strays away from the linear fit in section three marks the transition point between the second

and third section. An example for the estimated intersection points for the first resonance can be seen in Figure 4.17. The plots for all currents can be found in Figure 6.10 in the appendix.

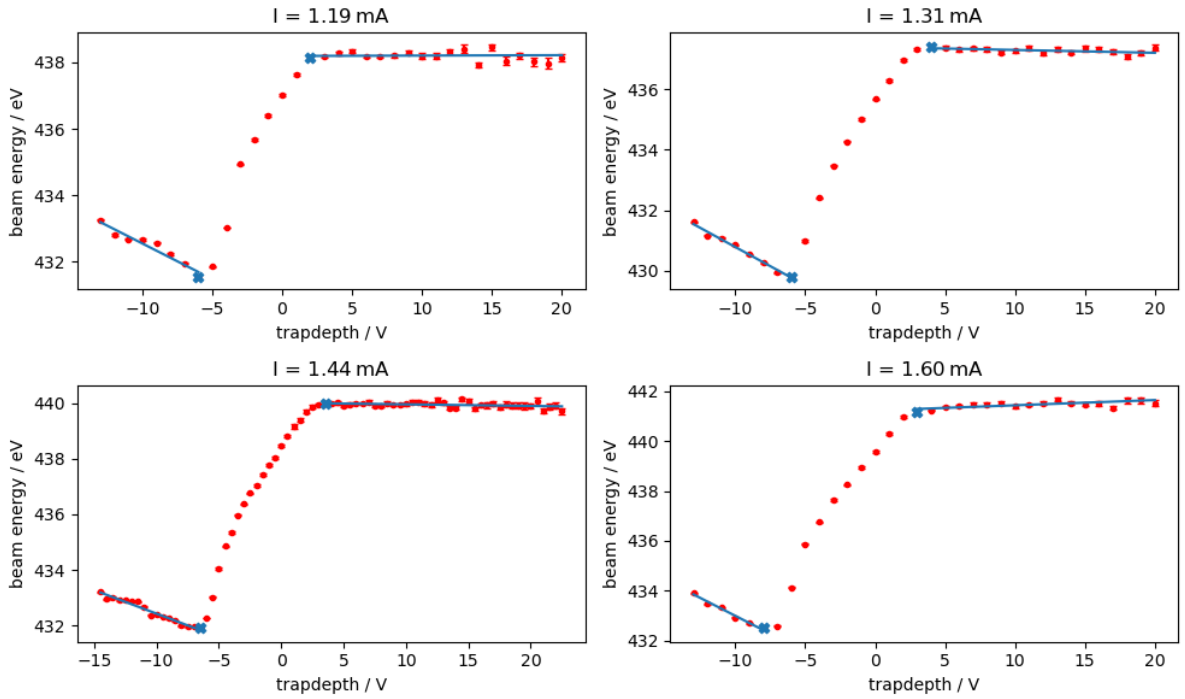

Figure 4.17: Determining the transition points between the three different regions for the first resonance line. The transition points are shown for four different electron beam currents. The resonance positions (red) are plotted as a function of the trap depth and fitted with a line (blue) in the first and third section. Blue crosses mark the determined intersection points.

Whilst the first and third section can be fairly well described by a linear function, the second section behaves differently. This is due to the evaporation of the ions as explained in section 2.3.2 and described by equation 2.17. The second region of the first resonance is depicted in Figure 4.18 for four different beam currents. The two blue crosses that mark the end of the region are equivalent to the intersection points in Figure 4.17. A line is fitted to the second region. The residuals are shown in the lower half of the plots and form a curve. Due to time constraints, equation 2.17 was not solved numerically and compared to the data, but the curve can be explained qualitatively. Assuming the ion cloud has a fixed temperature, with an energy distribution as given by the Maxwell-Boltzmann law. Reducing the trap depth will lead to the escape of the most energetic ions (i.e. with a higher energy than $q_i V_T$), reducing the ion amount. Reducing the trap depth further and further leads to an escape as given by the MB-integral. However, due to thermalisation after the highly energetic ions left the trap, the temperature of the ion cloud will also lower, leading to a more complex behavior.

The beam energy of determined intersection points is shown in Figure 4.19. In the upper half of the plot, the absolute intersection positions are shown, whilst in the lower half the

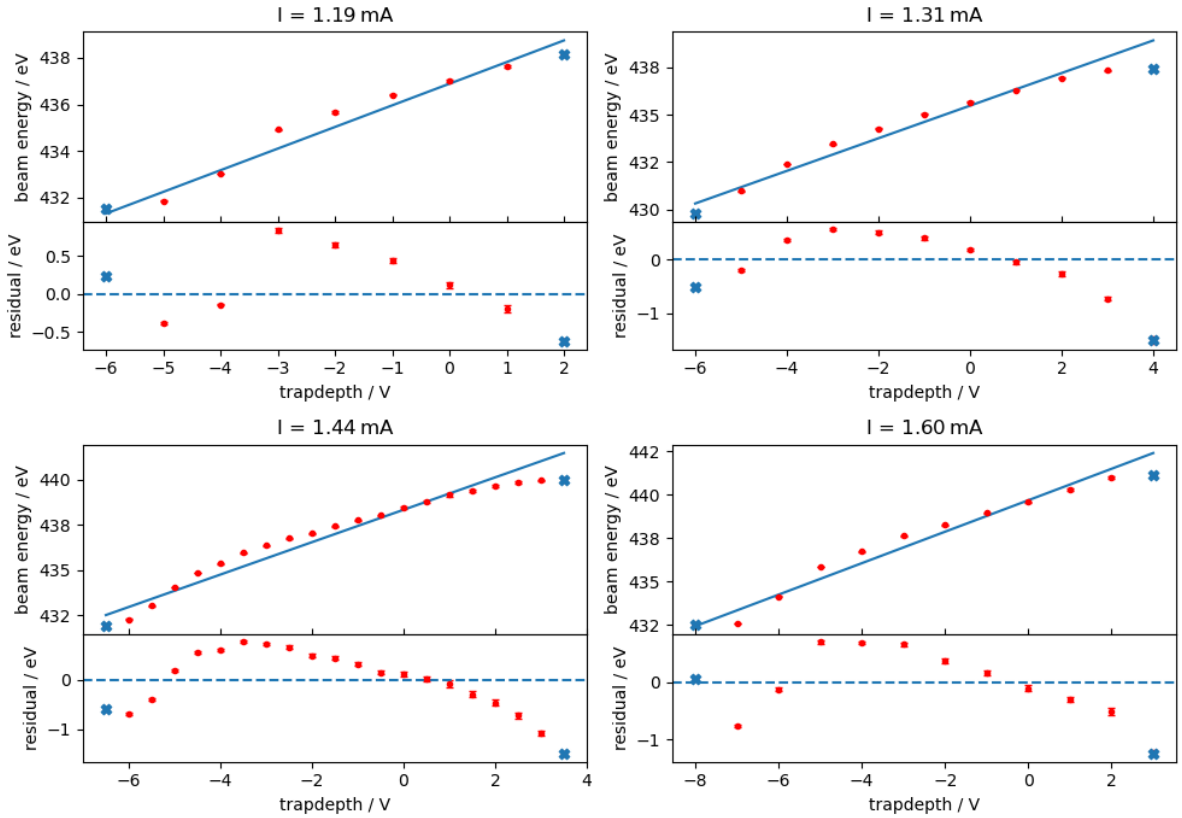

Figure 4.18: Second region from Figure 4.17. Crosses mark the intersection points to the neighboring region. The resonance positions are fitted with a line (blue). The residuals can be seen in the lower half of the plot, showing the insufficiency of the linear description.

relative positions to the intersection point at $I = 0.63\,\text{mA}$ are shown. Two data sets can be distinguished as seen most clearly by the difference in the relative resonance position of the intersection between the first and second region. The resonance positions for the electron beam currents 0.78 mA, 0.99 mA, 1.19 mA, 1.44 mA and 1.60 mA are shifted with respect to the other currents. The shift can also be seen in the intersection of the second to the third region. This is attributed to a change in the experimental setup. To increase the transmission, the gun position was changed between the two data sets which also leads to a change in resonance positions. Due to this, it is necessary to separate the measured data into these data sets. For the following analysis, the data for the five currents specified above is used.

The electron beam energy of the first resonance for the selected currents is plotted as a function of the trap depth in Figure 4.20. For the first region as marked in the figure, the resonance position seems to be independent of the current as the trap is full and the maximal compensation due to the ions is reached. In the second and third region, the shift of the resonance position seems to be proportional to the current since the electron beam space charge is proportional to the current as given in equation 2.11 and maximal compensation is not reached. The beam energies for all the resonances of these five currents can be found in Figure 6.11 in the appendix.

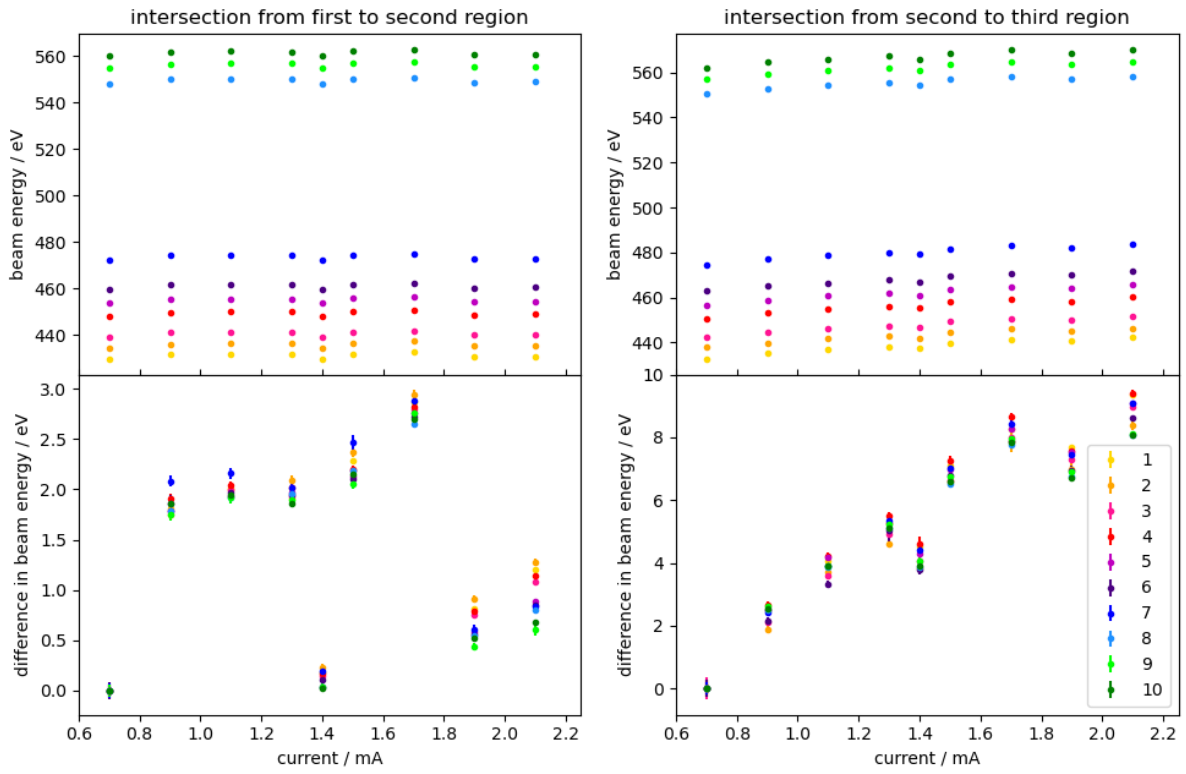

Figure 4.19: Electron beam energy for the intersection points between the three regions as a function of the current. Each color represents a different resonance. Top: Absolute position of the intersection points. Bottom: Resonance position relative to the respective intersection at $I = 0.66\,\mathrm{mA}$.

First of all, the ion space charge is calculated. This is accomplished by determining the shift in the resonance energy between an empty and a full trap due to the compensation of the ions. To achieve this, the difference of the nominal resonance energies at the intersection points is calculated for each current. The calculated shifts are plotted in Figure 4.21 as a function of the electron beam current. The shift increases with the electron beam current since the negative space charge and therefore the radial trapping potential of the electron beam increases and more ions can be confined. The ion compensation is fitted with a linear function. The result of the fit can be seen in Figure 4.22. In the left plot, the fitted linear function is extrapolated to zero current. The right plot depicts the slope of the fit which gives the ion space charge compensation per current. The weighted average is calculated as $(-5.82 \pm 0.36)\,\mathrm{eV/mA}$ and is marked in Figure 4.22. The slope of all fitted lines agrees within the uncertainty with the average.

In a second step, the electron beam space charge is calculated. The resonance energies of the intersection points between the second and third region are plotted as a function of the electron beam current in Figure 4.23. These are the resonance positions for an empty trap that

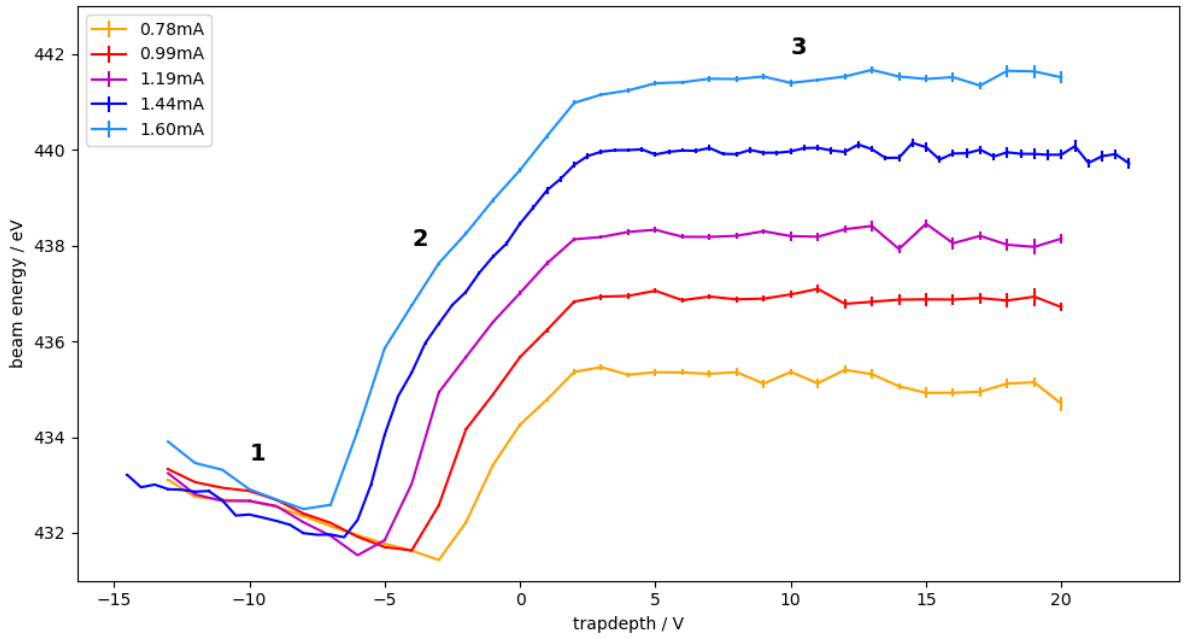

Figure 4.20: Electron beam energy of the first resonance as a function of the trap depth for the currents that were selected for the further data analysis. Each line represents a specific electron beam current. The three different regions are annotated in the plot.

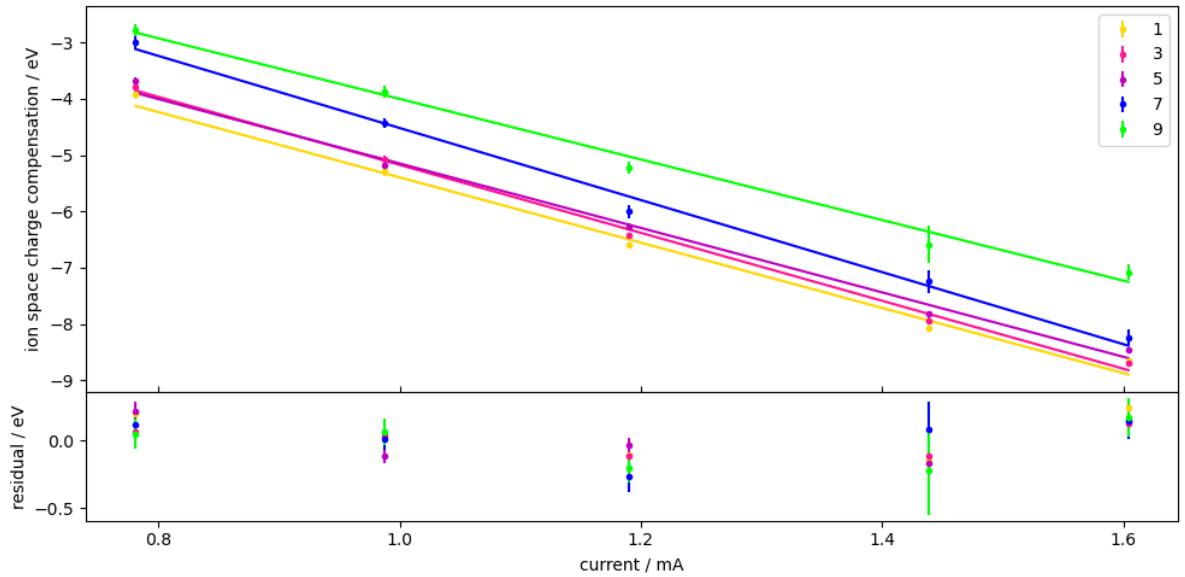

Figure 4.21: Difference of the resonance energies between the two intersection points as a function of the electron beam current. This corresponds to the compensation by the ion space charge. For the sake of clarity, only a selection of the resonances are plotted, each marked with a different color and fitted with a linear function. The residuals of the fits can be seen in the lower plot.

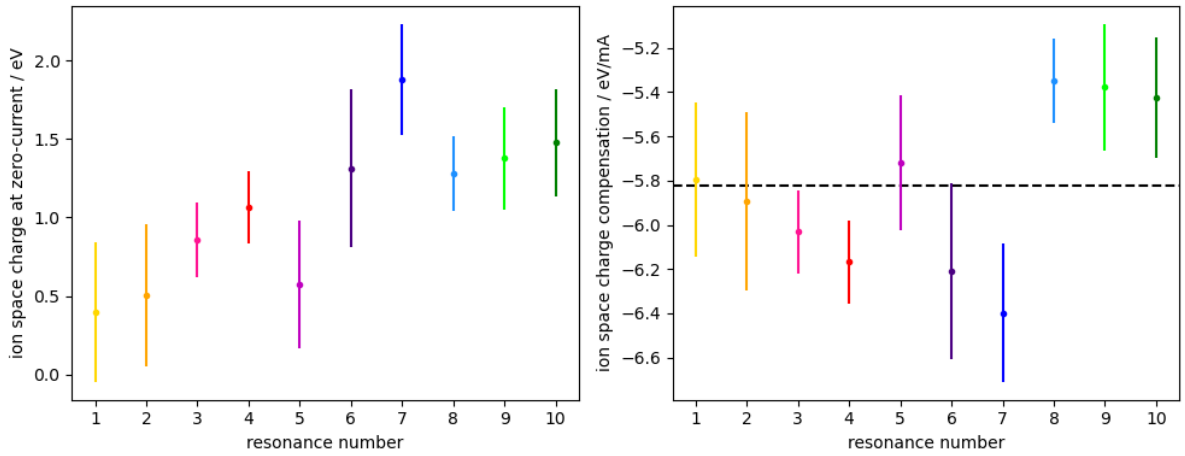

Figure 4.22: Result of the fit in Figure 4.21 for the different resonances. Left: Extrapolation of the linear fit to zero current. Right: Slope of the fitted linear function which gives the compensation by the ion space charge per current. The weighted average is marked in black.

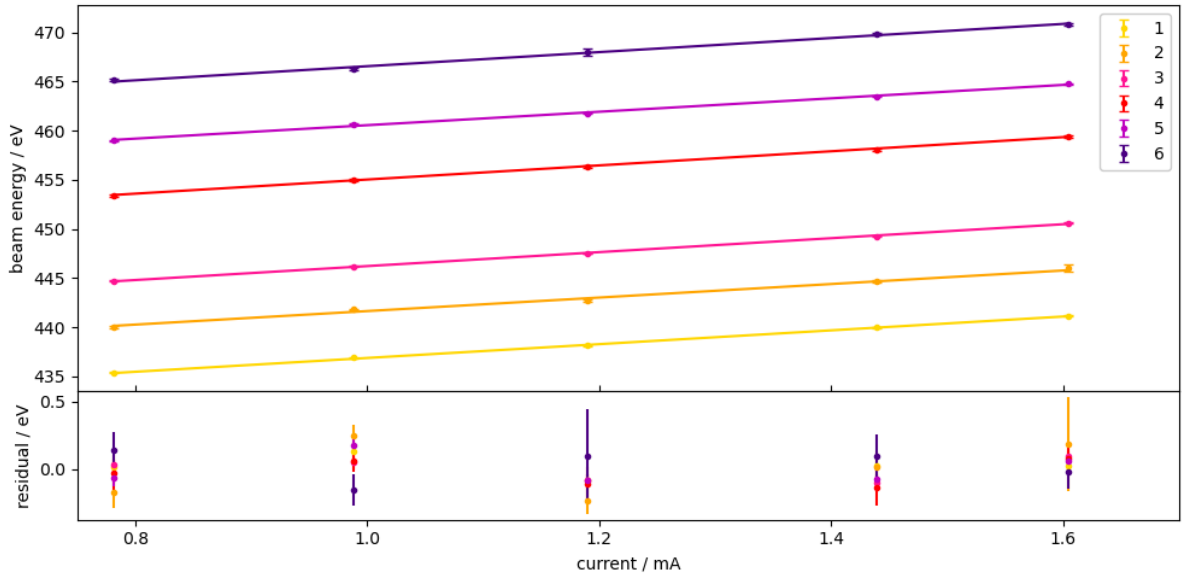

Figure 4.23: Resonance energy of the intersection between the second and third region as a function of the electron beam current. The resonance positions are fitted with a linear function and the residuals are depicted in the lower plot. For the sake of clarity, only a selection of the resonances is plotted.

are shifted solely by the electron beam space charge. The resonance energies are fitted with a linear function due to the proportionality of the beam current to the electron space charge in equation 2.11 and the result of the fit is shown in Figure 4.24. In the left plot, the linear function is extrapolated to zero current in order to give the resonance position without the contribution of the ion and the electron space charge. The slope of the fitted lines is shown in the right plot.

It corresponds to the electron space charge contribution per current. The weighted average is calculated as (6.81 ± 0.35) eV/mA and marked in the plot. Since the electron space charge is proportional to the inverse velocity according to equation 2.11, it is lower for higher electron beam energies.

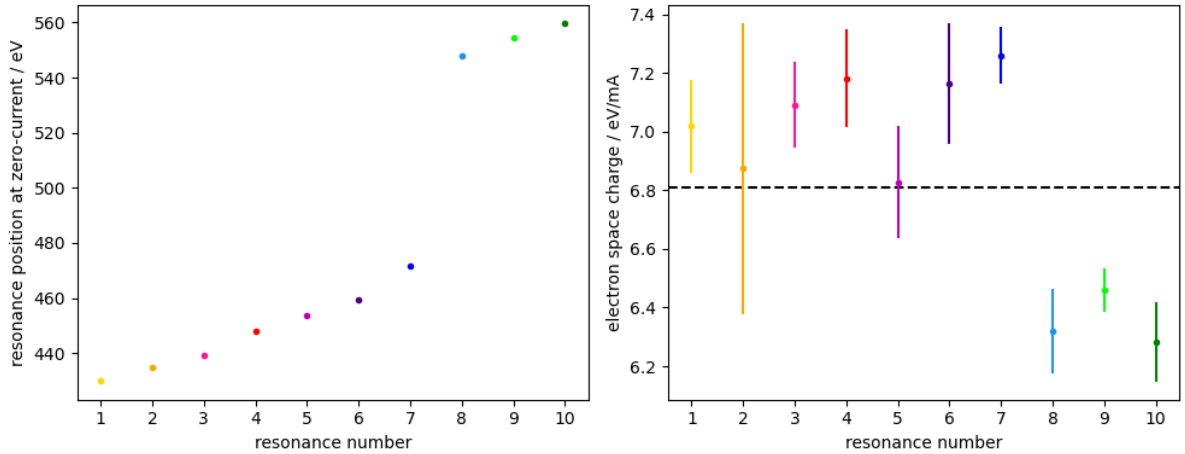

Figure 4.24: Result of the fit in Figure 4.23 for the different resonances. Left: The fitted lines are extrapolated to zero current to give the resonance position without influence of the electron or ion space charge. Right: Slope of the fitted line that corresponds to electron space charge per current. The weighted average is marked in black.

To calculate the final experimental resonance energies, the resonance positions from Figure 4.24 have to be corrected for the work functions of the cathode and DT4 according to equation 2.14. The work function of the cathode is $W_{\text{cath}} \approx 2\,\text{eV}$. The work function of DT4 is not precisely known and its material is specified only as titanium alloy in [33]. It is therefore approximated by the value for titanium which amounts to 4.33 eV [36]. For the helium-like oxygen resonances, the calculated energies are compared to the theoretical values from Figure 4.10. The difference of the experimental to the theoretical resonance positions is shown in Figure 4.25 and the final values are listed in Table 4.1. The experimental and theoretical resonance energies agree qualitatively. This can be improved by measuring the given voltages to the drift tubes and cathode with accurate high voltage dividers. Moreover, the work function of the cathode and DT4 are not directly measured, but estimated.

Given the ion and electron space charge, the compensation factor can be determined. It is the ratio of the ion charge inside the beam to the electron charge of the beam and can be calculated by dividing the ion space charge by the electron space charge. The results for all resonances are depicted in Figure 4.26. The weighted average for the compensation factor is $(85.2 \pm 1.7)\,\%$ and agrees with the individual values within the error.

No.	charge state	DR scheme	configuration	exp. E_{res} [eV]	theo. E_{res} [eV]
1	He	KLL	$\left[(1s2s)_0 2p_{1/2}\right]_{J=1/2}$ $\left[(1s2s)_0 2p_{3/2}\right]_{J=3/2}$	427.53 ± 0.20	426.74
2	He	KLL	$\left[(1s2s)_1 2p_{3/2}\right]_{J=1/2}$ $\left[(1s2s)_0 2p_{3/2}\right]_{J=3/2}$	432.44 ± 0.56	432.04
3	He	KLL	$\left[1s2p_{1/2}2p_{3/2}\right]_{J=5/2}$ $\left[1s2p_{1/2}2p_{3/2}\right]_{J=3/2}$	436.80 ± 0.18	436.58
4	He	KLL	$\left[1s2p_{3/2}^2\right]_{J=1/2}$	445.51 ± 0.21	446.30
5	Li	KLL	$\left[(1s2s)_1 2p_{1/2}2p_{3/2}\right]_{J=3}$ $\left[(1s2s)_1 2p_{3/2}^2\right]_{J=2}$ $\left[(1s2s)_1 2p_{1/2}2p_{3/2}\right]_{J=1}$	451.39 ± 0.26	-
6	Li	KLL	$\left[(1s2s)_1 2p_{3/2}^2\right]_{J=1}$ $\left[(1s2s)_0 2p_{1/2}2p_{3/2}\right]_{J=2}$	457.05 ± 0.26	-
7	Be	KLL	$\left[(1s2s^2)_{1/2} 2p_{1/2}2p_{3/2}\right]_{J=5/2}$ $\left[(1s2s^2)_{1/2} 2p_{1/2}2p_{3/2}\right]_{J=3/2}$	469.13 ± 0.11	-
8	He	KLN	-	545.53 ± 0.18	543.91
9	He	KLO	-	552.01 ± 0.08	549.53
10	He	KLO	-	557.33 ± 0.17	555.13

Table 4.1: Experimentally determined and theoretical (FAC) resonance energies E_{res}

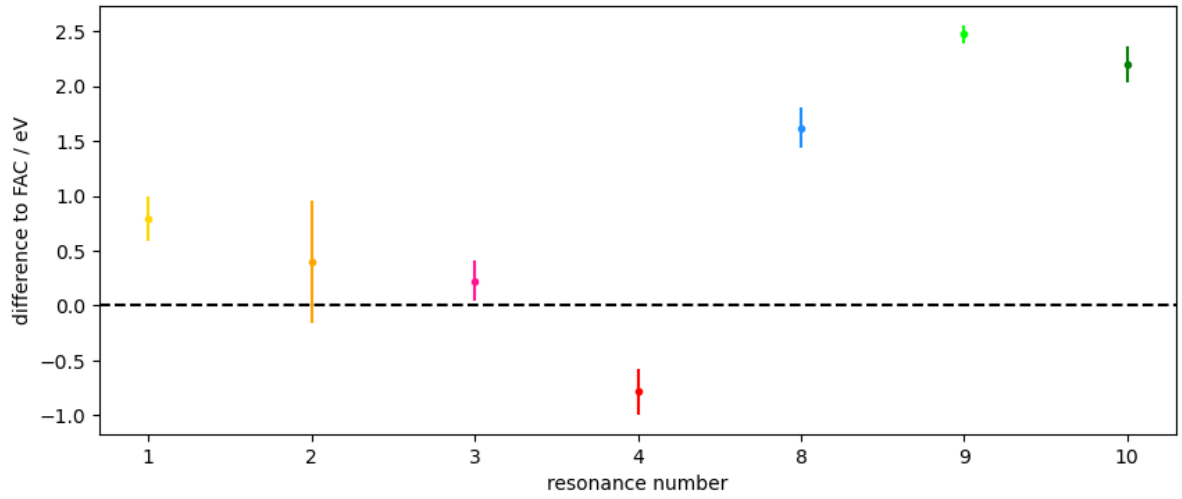

Figure 4.25: Difference of the experimentally determined resonance positions for helium-like oxygen to the theoretical calculations with FAC. The experimental resonance energies are corrected for the work function of the cathode and DT4.

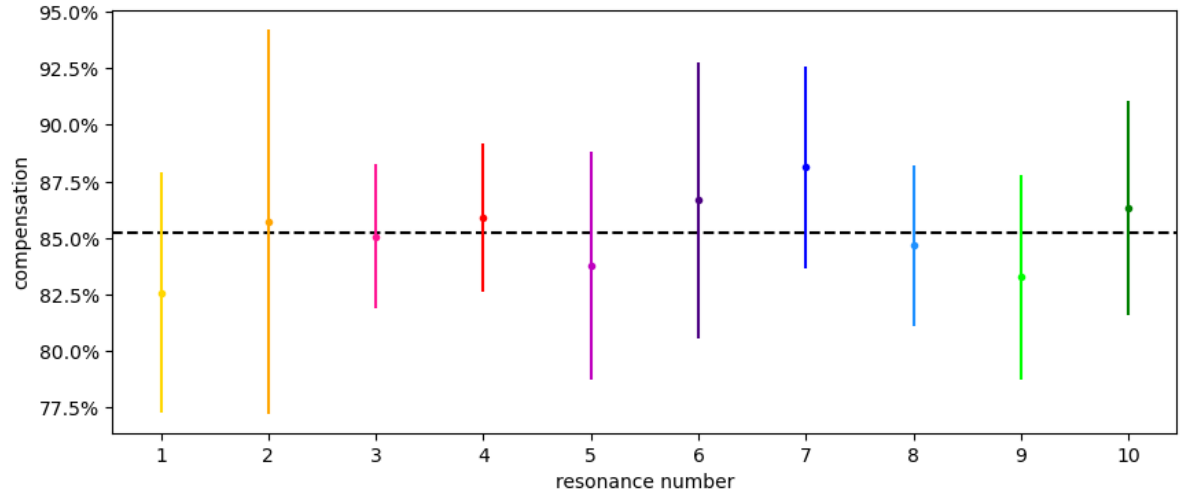

Figure 4.26: Compensation factor for each resonance for a deep trap. The weighted average is marked in black.

4.5 Charge state distribution

In order to calculate the resonance strengths, the charge state distribution inside the trap has to be known. This can be determined from the ToF measurements. As described in section 3.8.4, the ToF spectrum was recorded for each combination of beam current, trap depth and electron beam energy. The integrated signal for each ion peak is proportional to the ion number. By integrating the peaks and calculating their relative percentages, the contribution of each ion to the charge state distribution can be inferred. The calculated resonance strengths are expected

to be independent of the electron beam current. The charge state distribution, the number of ions, the electron current density and the line intensity are hence calculated for a beam current of $I = 1.44\,\mathrm{mA}$. For this current, the most detailed DR measurement was performed. In the upper plot of Figure 4.6 it can be seen, that the charge state distribution is almost constant for deep traps. Therefore, one of the deep trap depths can be chosen to calculate the distribution, in this case $V_T = -9\,\mathrm{V}$. The ToF spectrum for $I = 1.44\,\mathrm{mA}$, $V_T = -9\,\mathrm{V}$ and varying electron beam energies can be seen in Figure 4.27. The two red lines were identified as helium-like (left) and lithium-like oxygen (right).

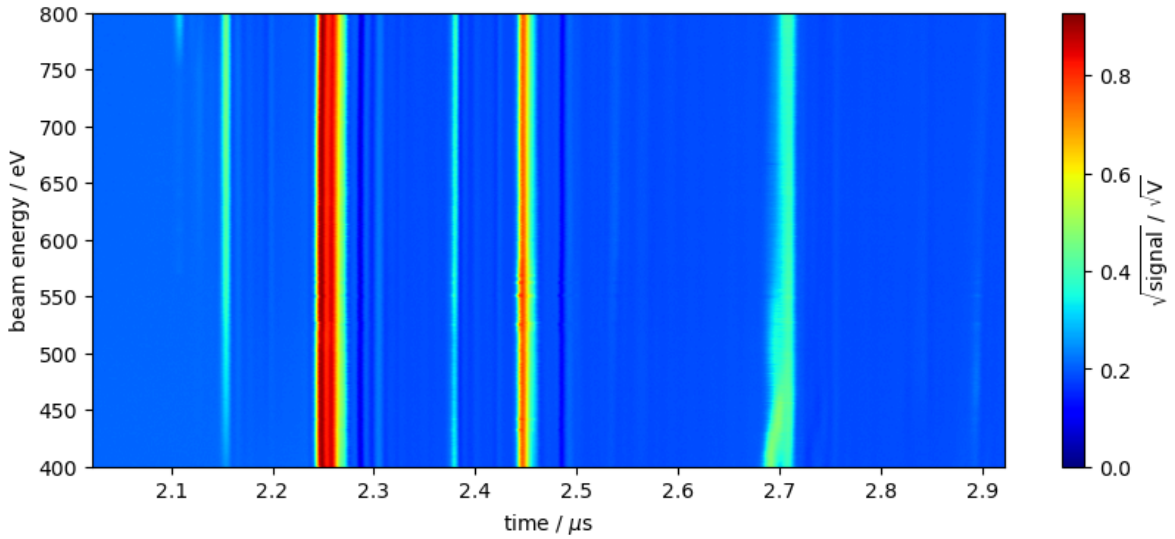

Figure 4.27: ToF signal for $I = 1.44\,\mathrm{mA}$ and $V_T = -9\,\mathrm{V}$ for varying beam energies.For better visibility, the square root of the signal is depicted .

On a side note, the DR resonances are also reflected in the ToF data. Because the recombination cross section of the ion is significantly enhanced at a resonance, the population of this charge state decreases inside the trap. Simultaneously, the amount of ions of the lower charge state to which the ion recombines increases. This can be seen in Figure 4.28. In the upper plots, the ToF signal of helium-like oxygen is depicted. On the left, a closer view of the peak in 4.6 is shown, whilst the signal was summed up along the time axis on the right. The summed voltage is proportional to the integrated signal and shows the amount of ions in the trap as a function of the beam energy. The same was done in the plots in the middle of the figure for lithium-like oxygen. For certain energies, The summed signal shows a distinct decrease in helium-like oxygen and an increase in lithium-like oxygen. The ratio of the summed signal of lithium-like oxygen to the summed signal of helium-like oxygen is shown in the lower plot of Figure 4.28.

The ratio of the lithium-like to helium-like oxygen ToF signal can be compared to the DR data for $I = 1.44\,\mathrm{mA}$ and $V_T = -9\,\mathrm{V}$ as displayed in Figure 4.29. Since the ToF data is quite noisy, only the most distinct peaks can be made out. Most of the peaks from the DR data can be found in the ToF data and match in good agreement. It can be seen in Figure 4.10 that only the peaks

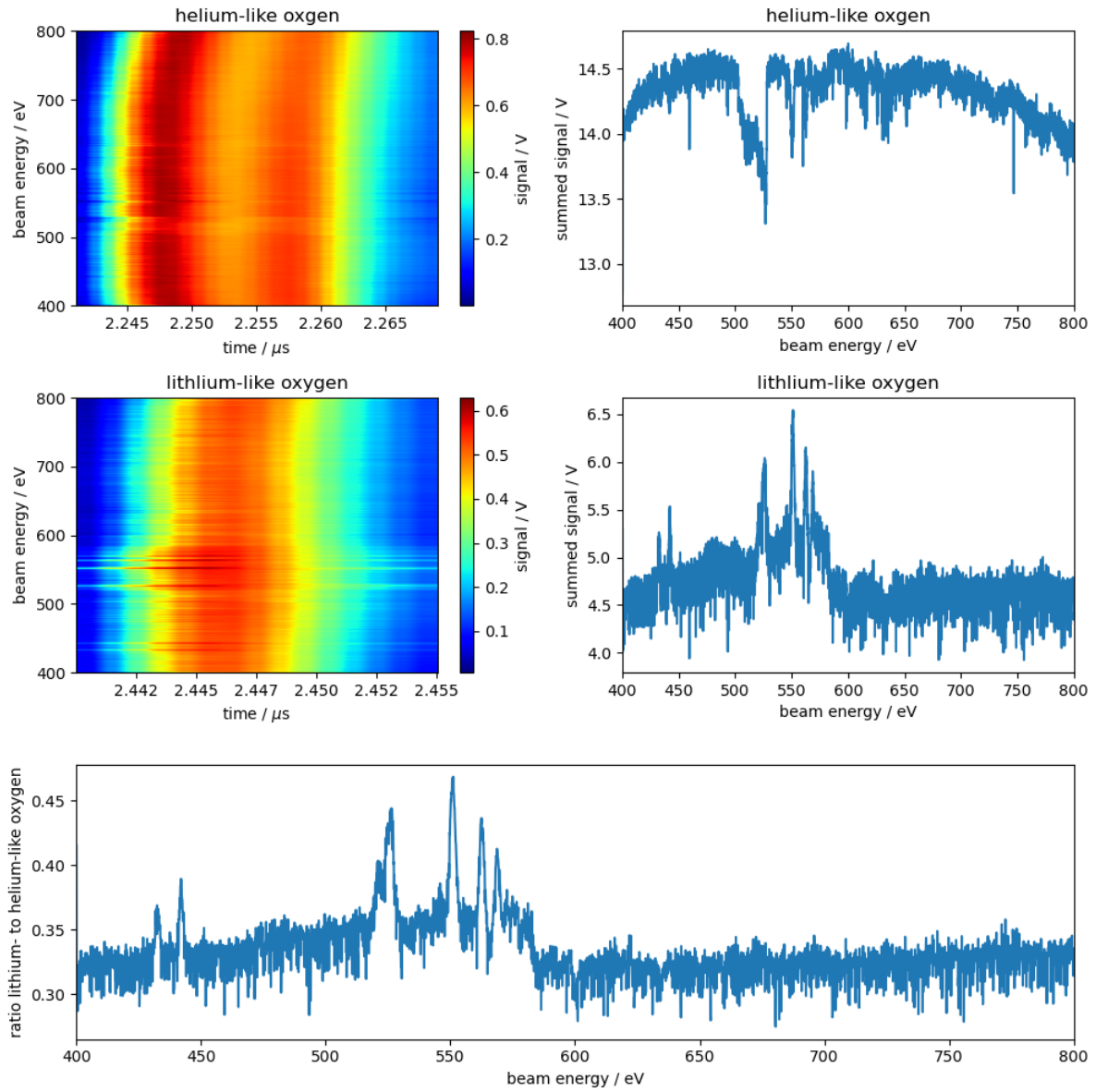

Figure 4.28: ToF signal for helium-like and lithium-like oxygen. Left: Spectra of the helium-like (top) and lithium-like (bottom) oxygen line from Figure 4.30. Right: ToF signal summed along the time axis for the helium-like (top) and lithium-like (bottom) oxygen. Bottom: Ratio of the summed lithium-like to the summed helium-like oxygen ToF signal.

of the helium-like DR resonances have a corresponding peak in the ToF data. The other peaks belong to different charge states and are therefore not seen as a change in the helium-like to lithium-like distribution.

To calculate the charge state distribution, the ToF data was separated into ten energy slices. Each slice encompasses the region of one of the DR resonances marked in Figure 4.11. These slices were summed up along the beam energy axis. The summed ToF signal for the first DR

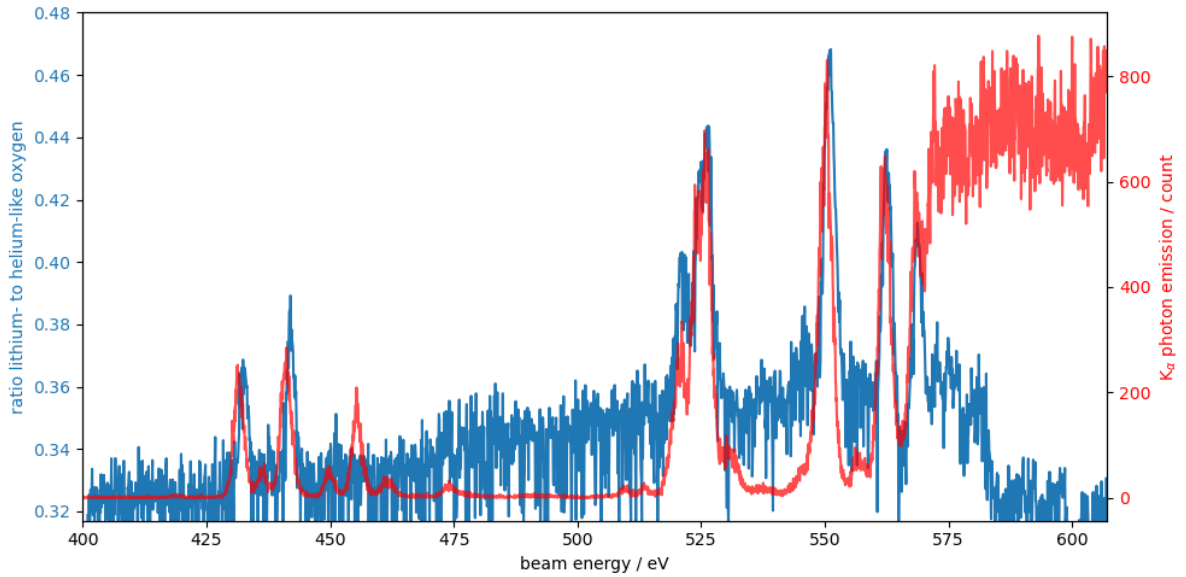

Figure 4.29: Comparison of the resonances seen in the TOF data to the resonances in the DR data for $I = 1.44\,\text{mA}$ and $V_T = -9\,\text{V}$. Blue: Ratio of the lithium-like to helium-like summed ToF signal from Figure 4.28. Red: K_α photon count as a function of the beam energy.

resonance can be seen in Figure 4.30 and for all resonances in Figure 6.12 in the appendix. The regions of the most distinct ToF peaks are marked. For the analysis, the other ToF peaks are negligibly small and thus only the marked peaks are integrated to determine the charge state contribution. The double peak structure is most likely due to the extraction system. If the parameters of the extraction are changed, the structure can vanish or be enhanced. The charge states of the marked peaks were identified analogous to section 4.2 and are annotated in Figure 4.30.

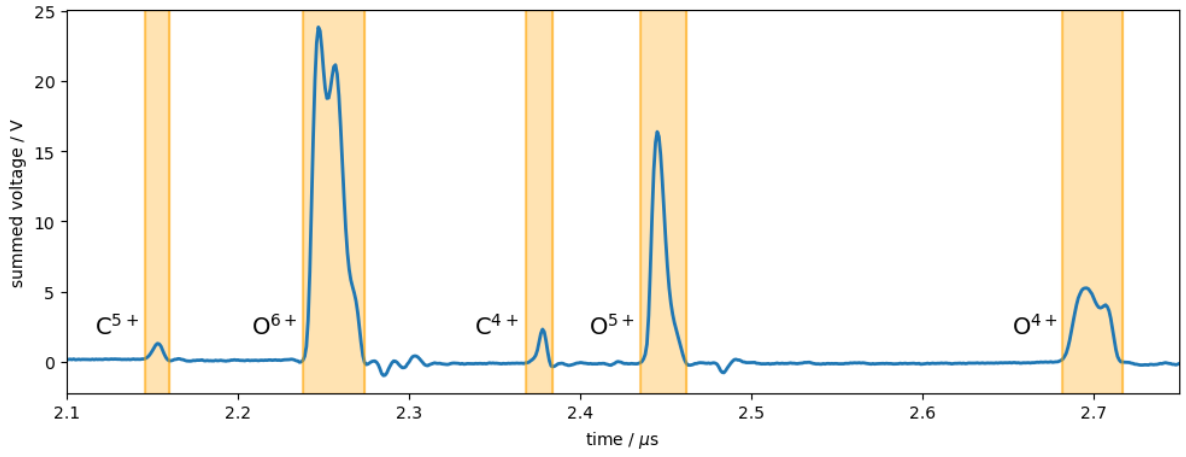

Figure 4.30: Summed ToF signal for the first DR resonance. The ion peaks that are going to be integrated are marked in orange and annotated with the corresponding charge state.

To calculate the relative contribution, the marked peaks were numerically integrated using the trapezoidal rule. The maximum uncertainty due to the numerical integration is given by

$$\Delta I = \frac{(b-a)^3}{12N^2} |\max\left(f''(t)\right)|, \tag{4.5}$$

where a and b are the boundary points of the interval, t is a value in $[a,b]$, N is the number of steps in the interval and f'' the second derivative of the data. f'' can be calculated numerically [37].

The percentage of the integrated area for the different ions corresponds to the percentage of the ion content due to the signal being proportional to the number of the detected ions. The percentage of the different charge states is plotted in Figure 4.31 for all resonances. The uncertainties originate from the numerical integration with the trapezoidal rule. The average relative contributions are (61.3 ± 0.9), % for helium-like oxygen, (22.7 ± 1.8) % for lithium-like oxygen, (12.2 ± 2.6) % for beryllium-like oxygen, (2.1 ± 0.7) % for hydrogen-like carbon and (1.6 ± 0.3) % for helium-like carbon. The percentage of the lower charge states slightly decreases for higher energies as the percentage for the higher charge states increases, since the electrons are more energetic and ionisation cross sections increase for the higher charge states relative to the lower ones.

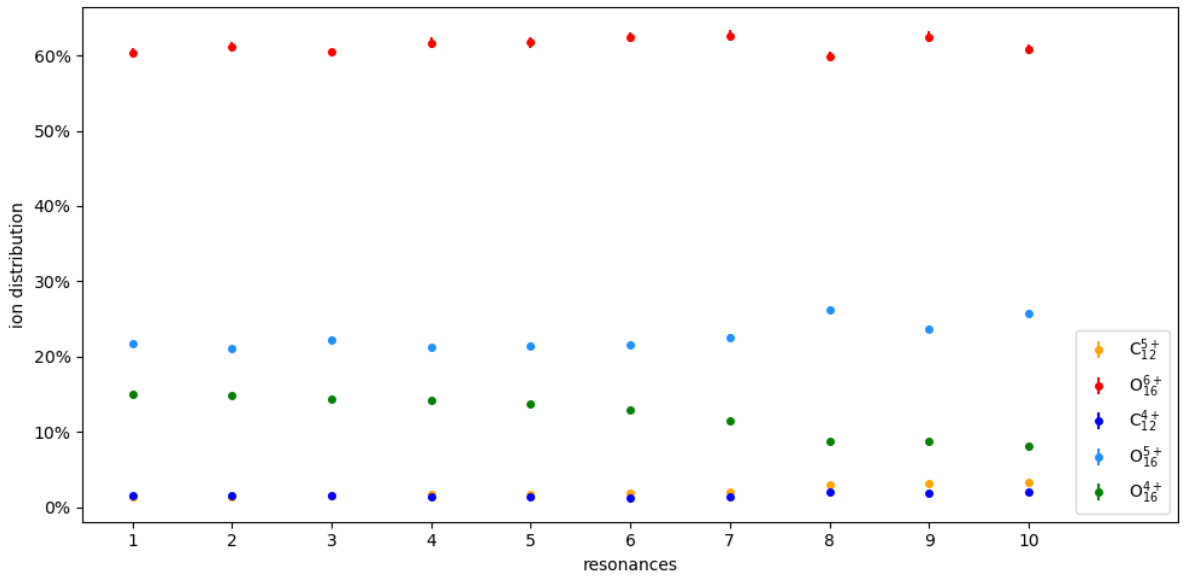

Figure 4.31: Percentage of the ion charge states in the trap for the different resonances. Each ion is depicted in a different color.

4.6 Electron current and number of ions

To determine the resonance strength, the electron current density and number of ions inside the electron beam are required. The resonance strength is expected to be independent of the electron beam current. Since the ion distribution was determined for $I = 1.44\,\mathrm{mA}$, the remaining unknown parameters needed for the resonance strength were also calculated for this current.

The beam radius and thus the electron current density depend on the velocity v_e and therefore on the beam energy. The observed resonance energies range from 432 eV to 562 eV. The relativistic velocity v_e can be calculated with equation 2.12 and ranges from $1.23 \cdot 10^7 \frac{\mathrm{m}}{\mathrm{s}}$ to $1.41 \cdot 10^7 \frac{\mathrm{m}}{\mathrm{s}}$.

To calculate the electron current density, the electron beam radius needs to be known. There are two ways to calculate the beam radius. One way is to utilise the Herrmann radius with $I = 1.44\,\mathrm{mA}$, $B = 0.86\,\mathrm{T}$, $T_c = 1400\,\mathrm{K}$ and $r_c = 1.7\,\mathrm{mm}$ according to equation 2.9. B_c can be estimated. The cathode position is at a minimum of the EBIT magnetic field, but the earth magnetic field and weak magnetic fields in the laboratory still need to be taken into account. B_c is therefore estimated as $100\,\mu\mathrm{T}$ [33]. With these values, the Herrmann radius was determined as $68.4\,\mu\mathrm{m}$. Another way to calculate the beam radius involves the space charge potential. Because of to the ion compensation, the space charge potential inside r_e can be assumed to be flat [33]. Therefore, the measured space charge $\Phi_e = I \cdot (6.81 \pm 0.35)\,\mathrm{eV/mA}$ is assumed to be equivalent to $\Phi_e(r_e)$. Rearranging equation 2.11 gives

$$r_e = r_{\mathrm{dt}} \cdot \exp\left(\frac{2\pi\epsilon_0 v_e \Phi_e(r_e)}{I}\right). \tag{4.6}$$

The calculated electron beam radius amounts to $(23.6 \pm 5.6)\,\mu\mathrm{m}$ for 432 eV and $(12.2 \pm 3.3)\,\mu\mathrm{m}$ for 562 eV.

The electron current density j_e is estimated using formula 2.13 for $I = 1.44\,\mathrm{mA}$, the beam radius as determined from the space charge. Consequently, the electron current density is $(5.2 \pm 2.5) \cdot 10^{24} \frac{1}{\mathrm{m^2 s}}$ for 432 eV and $(1.9 \pm 1.1) \cdot 10^{25} \frac{1}{\mathrm{m^2 s}}$ for 562 eV.

The amount of ions can be calculated from the electron beam current I and the compensation factor $\alpha = (85.2 \pm 1.7)\,\%$ which is equivalent to the ratio of the ion to the electron space charge inside the beam. The ion charge per time is

$$\frac{dQ_i}{dt} = \alpha \cdot I. \tag{4.7}$$

From this, the ion charge per length can be calculated by

$$\frac{dQ_i}{dl} = \frac{1}{v_e}\frac{dQ_i}{dt}, \tag{4.8}$$

with the electron velocity v_e. To determine the number of ions inside the trap, the average charge state $\bar{q}_i$ needs to be known. This can be inferred from the charge state distribution calculated in section 4.5. The total number of ions per length is calculated by

$$\frac{dN_i}{dl} = \frac{1}{e\bar{q}_i}\frac{dQ_i}{dl}, \tag{4.9}$$

where e is the elementary charge. To get the number of ions inside the trap is needed. Only ions that are observable through the cut-out of DT4 can be measured and thus the length l is set to the cut-out length of 16 mm. The total number of ions inside the trap is calculated as $(1.84 \pm 0.15) \cdot 10^6$ for 432 eV to $(1.56 \pm 0.13) \cdot 10^6$ for 562 eV with a total ion charge of $(9.98 \pm 0.80) \cdot 10^6\, e$ for 432 eV to $(8.75 \pm 0.70) \cdot 10^6\, e$ for 562 eV. This is consistent with the measurements performed with the bender in section 3.8.2 that estimated an lower limit of $(6.1 \pm 0.1) \cdot 10^6\, e$ for long ramp times and optimal trap depths.

To calculate the resonance strength, the overlap factor f of the electron beam with the ion cloud is required which is defined as the ratio

$$f = \frac{N_i^{in}}{N_i}, \tag{4.10}$$

where N_i is the total amount of ions inside the trap and N_i^{in} the number of ions inside the electron beam [20]. The overlap factor however is a complex parameter and cannot be calculated with the measurements performed in this work. It can be estimated via the geometrical overlap factor f_g as

$$f_g = \left(\frac{r_e}{r_i}\right)^2, \tag{4.11}$$

where r_e is the radius of the electron beam and r_i the radius of the ion cloud [38]. The former is given by the electron space charge radius, whilst the latter is estimated by the gyroradius of the circular ion trajectory due to the Lorentz force

$$r_i = \frac{m_i v_\perp}{|q_i| B}, \tag{4.12}$$

where m_i is the ion mass, $v_\perp$ the velocity component perpendicular to the magnetic field, q_i the ion charge and B the magnetic flux density[39]. The ion velocity is calculated from the ion temperature T_i that can be estimated using equation 2.15. The velocity is non-relativistic and can therefore be determined by

$$v_\perp = \sqrt{\frac{2k_B T_i}{m_i}} \tag{4.13}$$

with the Boltzmann constant k_B. The uncertainty on the ion temperature is estimated to be 20%. This leads to an ion cloud radius of $(368 \pm 37)\,\mu$m. The resulting overlap factor depends on the electron beam energy due to the space charge radius and reaches from $(4.1 \pm 2.1) \cdot 10^{-3}$ for 432 eV to $(1.1 \pm 0.6) \cdot 10^{-3}$ for 562 eV.

4.7 Line intensity

Another factor required to calculate the resonance strengths is the line intensity which is determined for the same trap depth of -9 V as the charge state distribution. As seen in Figure 4.6, the intensities stay approximately constant for deep traps. Since the counts were recorded for discrete energy steps, they have to be divided by the time that was spend at each energy to get the intensity. The time interval was measured during the experiment for each step and results in an average time of (611.5 ± 26.9) ms. The intensity for each resonance is then extracted by fitting a Gaussian distribution and calculating the area underneath the function. For this, the energy step size of 0.1 eV has to be taken into account. The resulting intensities can be seen for each resonance in Figure 4.32 as a function of the electron beam current. The uncertainties are estimated from the fit and the standard deviation of the time interval.

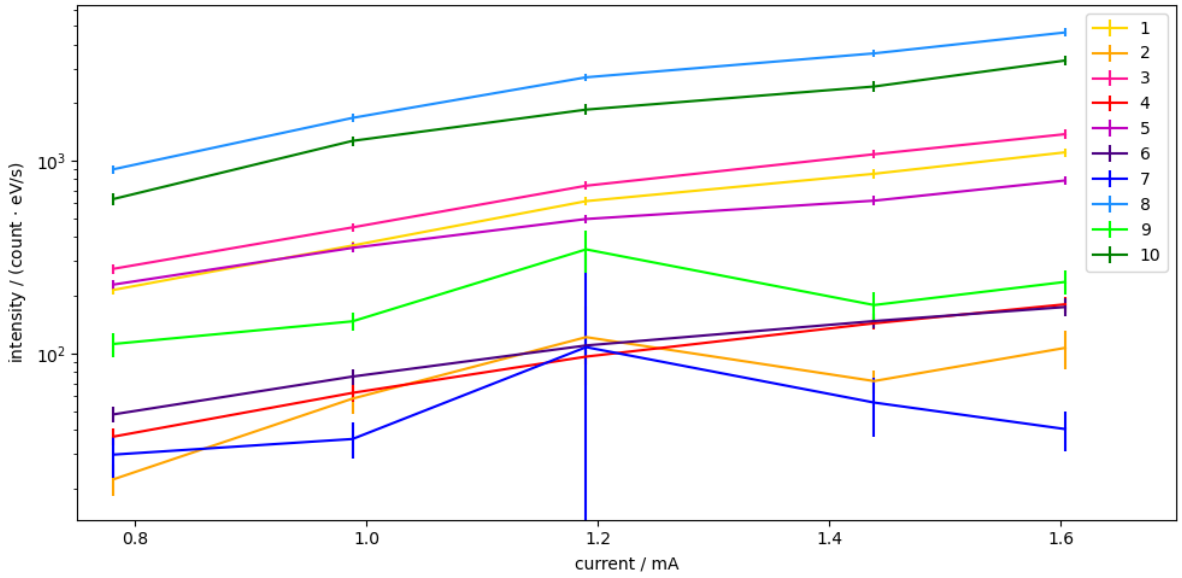

Figure 4.32: Intensity of the resonances as a function of the electron beam current. Each resonance is marked in a different color.

4.8 Absolute resonance strengths

The absolute DR resonance strengths $S_{90^\circ}^{\mathrm{DR}}$ can be calculated using

$$I_{90^\circ}^{\mathrm{DR}} = \frac{j_{e,\mathrm{eff}}}{e} S_{90^\circ}^{\mathrm{DR}} p_{q_i} N_i \Omega \eta, \tag{4.14}$$

where $I_{90^\circ}^{\mathrm{DR}}$ is the intensity of the resonance recorded at 90° , $j_{e,\mathrm{eff}}$ the effective current density, e the electron charge, N_i the number of ions in the trap, p_{q_i} the percentage of ions with the charge q_i, Ω the solid angle of the detector and η the detection efficiency [25].

No.	charge state	$I_{90^\circ}^{\mathrm{DR}}\left[\frac{\mathrm{count\cdot eV}}{\mathrm{s}}\right]$	$j_e\left[10^{24}\frac{1}{\mathrm{m^2 s}}\right]$	$f\left[10^{-3}\right]$	$p_{q_i}[\%]$	$N_i\left[10^6\right]$
1	He	853 ± 45	5.1 ± 2.5	4.1 ± 2.1	60.3 ± 0.7	1.84 ± 0.15
2	He	72 ± 9	5.4 ± 2.6	3.9 ± 2.0	61.2 ± 0.7	1.82 ± 0.15
3	He	1077 ± 56	5.7 ± 2.8	3.7 ± 2.0	60.4 ± 0.6	1.81 ± 0.15
4	He	143 ± 11	6.3 ± 3.1	3.4 ± 1.8	61.7 ± 0.7	1.79 ± 0.14
5	Li	619 ± 35	6.6 ± 3.3	3.2 ± 1.7	21.4 ± 0.5	1.78 ± 0.14
6	Li	147 ± 12	7.1 ± 3.5	3.0 ± 1.6	21.5 ± 0.4	1.76 ± 0.14
7	Be	56 ± 19	8.1 ± 4.0	2.6 ± 1.4	11.5 ± 0.1	1.73 ± 0.14
8	He	3590 ± 170	17.1 ± 9.3	1.2 ± 0.7	59.9 ± 0.7	1.61 ± 0.13
9	He	178 ± 30	18.2 ± 9.9	1.2 ± 0.7	62.5 ± 0.7	1.59 ± 0.13
10	He	2417 ± 145	19.2 ± 10.5	1.1 ± 0.6	60.8 ± 0.7	1.59 ± 0.13

Table 4.2: Parameters used to calculate the resonance strengths

The important parameter for the recombination process inside the EBIT is the effective current density $j_{e,\mathrm{eff}}$. It is complicated to determine as it depends on the spatial distribution of the ions, overlap of the ion cloud with the electron beam and also on the ion gyration and oscillations in the trap [38]. It is therefore approximated with the overlap factor f as

$$j_{e,\mathrm{eff}} \approx f \cdot j_e \approx f_g \cdot j_e, \tag{4.15}$$

where f_g is the gemoetric overlap of the electron beam and the ion cloud.

The solid angle Ω depends on the distance between the trap center and the detector and the active area of the detector. The active area is specified as $150\,\mathrm{mm}^2$ by the manufacturer and the distance is $(31\pm1)\,\mathrm{mm}$ according the the SolidWorks model of the EBIT, resulting in a solid angle of $4\pi\cdot(12.4\pm0.8)\cdot10^{-3}\,\mathrm{sr}$.

The detection efficiency η depends on the thin layer of aluminium foil separating the detector and the trap chamber and the layer of silicon dioxide on the surface of the detector. The transmission efficiency of the 500 nm thick aluminium filter is 48.7% at the oxygen K_α wavelength of 573.95 nm [40] with an estimated uncertainty of 10%. In addition, a layer of silicon dioxide is located on the detector with an estimated thickness of 80 nm due to the reaction of the silicon with the residual oxygen in the EBIT. This results in a transmission efficiency of 78.2% for the K_α wavelength [40]. Since the thickness of the dioxide layer is not precisely known, the uncertainty of the transmission efficiency is estimated to be 10%. This results in a total detection efficiency $\eta = (38.0\pm5.4)\%$.

The parameters used to calculate the resonance strengths are listed in Table 4.2. The resulting values for the resonances are listed together with the theoretical values in Table 4.3 and shown

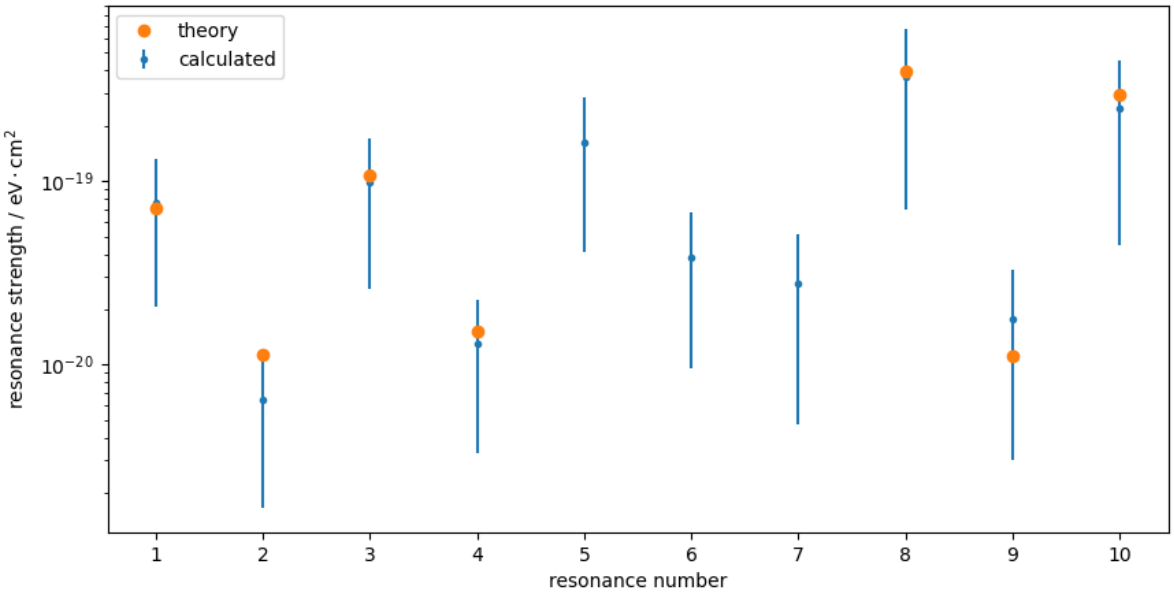

Figure 4.33: Experimentally determined and theoretical resonance strengths.

in Figure 4.33. The theoretical FAC calculations agree with the experimental results within the uncertainty. The relative errors of the resonance strengths including the relative errors of the used parameters are listed in Table 4.4. The relative errors of the calculated resonance strengths range from 72% to 83%. The main contributions to this large uncertainty is given by the current density j_e and the overlap factor f. The large uncertainty of the current density originates from the propagation of the electron space charge error. The resulting errors of the electron beam radius r_e and the current density j_e get increasingly larger. Since the ion temperature can only be estimated by equation 2.15, the temperature uncertainty is reckoned to be 20% which results in the large uncertainty for the overlap factor.

No.	charge state	DR scheme	$S_{90^\circ}^{\mathrm{DR}}\left[10^{-21}\,\mathrm{eV}\cdot\mathrm{cm}^2\right]$	$S_{90^\circ}^{\mathrm{theo}}\left[10^{-21}\,\mathrm{eV}\cdot\mathrm{cm}^2\right]$
1	He	KLL	76.8 ± 56.0	71.2
2	He	KLL	6.4 ± 4.8	11.3
3	He	KLL	97.9 ± 72.1	107.3
4	He	KLL	12.9 ± 9.6	15.1
5	Li	KLL	162.2 ± 121.2	-
6	Li	KLL	38.6 ± 29.1	-
7	Be	KLL	27.9 ± 23.2	-
8	He	KLN	370.9 ± 300.6	398.6
9	He	KLO	17.8 ± 14.8	11.2
10	He	KLO	249.3 ± 204.2	294.0

Table 4.3: Experimentally determined and theoretical (FAC) resonance strengths

No.	$S_{90^\circ}^{\mathrm{DR}}$	$I_{90^\circ}^{\mathrm{DR}}$	j_e	f	p_{q_i}	N_i	r_e	Ω	η
1	72.3	5.2	47.9	51.9	1.1	8.1	23.9	6.5	14.1
2	74.3	13.2	48.1	52.1	1.1	8.1	24.1		
3	73.6	5.2	48.4	52.4	1.1	8.1	24.2		
4	74.5	7.8	48.9	52.8	1.1	8.1	24.4		
5	74.7	5.6	49.2	53.1	2.2	8.1	24.6		
6	75.4	8.3	49.5	53.4	2.0	8.1	24.7		
7	83.0	33.9	50.2	54.0	0.7	8.1	25.1		
8	81.1	4.7	54.0	57.6	1.1	8.1	27.0		
9	83.1	16.7	54.4	57.9	1.1	8.1	27.2		
10	81.9	6.0	54.6	58.2	1.1	8.1	27.3		

Table 4.4: Relative error of the parameters used to calculate the resonance strength. All values given in percent.

5 Conclusion and outlook

In this work the DR resonance energies and absolute resonance strengths of highly charged oxygen ions were determined.

A lower limit for the total ion charge inside the trap was estimated for various ramp times and trap depths by using the bender as an improvised Faraday cup. For long ramp times and sufficiently deep traps, the lower limit of the total ion charge was determined as $(6.1 \pm 0.1) \cdot 10^6 e$. A decrease can be seen for deeper traps, possibly due to an increase of the ion temperature with the trap depth. In a next step, the charge states inside the trap were identified by a time-of-flight measurement for different trap depths and ramp times to observe the change of the ion charge state distribution in the trap. The predominant charge states in the trap were confirmed to be oxygen ions, with the main contribution originating from helium-like oxygen, followed by lithium-like and beryllium-like oxygen. Apart from oxygen ions, carbon and argon ions were found in the trap.

As a first step to estimate the DR resonance strengths, the required parameters had to be inferred from the time-of-flight and fluorescence data. First, the x-ray fluorescence data from the silicon drift detector was analysed. The signal for the K_α photon emission was selected and the focus was put on ten distinct DR resonance peaks whose resonance energies were determined for each trap depth-beam current combination. The resonance energies show a clear shift as a function of trap depth as seen in Figure 4.12. This shift was corrected for the reach-through effect due to the influence that the voltages applied to DT3 and DT5 have on the potential of DT4. The shift per trap depth caused by the reach-through was determined as (0.11 ± 0.02) eV/V. With this correction applied, the electron and ion space charge were determined. The ion space charge per electron beam current was determined by the shift in the resonance energy between a full trap and an empty trap that is caused by the ion content inside the trap. It amounts to (-5.82 ± 0.36) eV/mA. The electron space charge is given by the shift of the resonance energies at various electron beam currents for an empty trap and is estimated as (6.81 ± 0.35) eV/mA. The resonance energies without the contribution of the electron and ion space charge were determined by extrapolating the resonance position of an empty trap to zero current. These energies also had to be corrected for the work functions of the cathode and the drift tube DT4. In Table 4.1, the resonance energies determined this way are listed together with the calculated theoretical DR resonance energies. The compensation of the electron space charge by the ion charge is given by the ratio of the ion to the electron space charge and estimated as $(85.2 \pm 1.7)\%$ for deep traps. By integrating the peaks attributed to the different charge states in the time-of-flight signal, the relative charge state distribution can be inferred. The average contribution is $(61.3 \pm 0.9)\%$ for helium-like oxygen, $(22.7 \pm 1.8)\%$

for lithium-like oxygen and $(12.2 \pm 2.6)\,\%$ for beryllium-like oxygen. The electron beam radius was calculated from the space charge as $(23.6 \pm 5.6)\,\mu m$ to $(12.2 \pm 3.3)\,\mu m$. From the compensation, the total number of ions inside the trap is determined as $(1.84 \pm 0.15) \cdot 10^6$ to $(1.56 \pm 0.13) \cdot 10^6$. In order to get the number of ions inside the electron beam, the overlap factor has to be known. Since it was beyond the scope of this work to estimate the overlap experimentally, it was approximated by the geometric overlap as $(4.1 \pm 2.1) \cdot 10^{-3}$ to $(1.1 \pm 0.6) \cdot 10^{-3}$. The line intensities were determined by the Gaussian fit of the resonance. However, due to the unidirectional electron beam, these values reflect the intensity at a 90° angle. The transmission efficiency of the fluorescence signal was estimated as $\eta = (38.0 \pm 5.4)\%$ from the thickness of the aluminium filter and the silicon dioxide layer on the active surface of the photon detector.

In a final step, the DR resonance strengths at 90° angle were calculated from the estimated parameters listed in Table 4.2. The experimental values are summarised in Table 4.3 together with the calculated values. The relative uncertainty of the resonance strength and the parameters used for the calculation can be found in Table 4.4. Due to the propagation of the uncertainty of the electron space charge to the electron current density and the large uncertainty of the ion temperature and hence the overlap factor, the relative uncertainty of the resonance strength amounts to 72% to 83%. The experimental and theoretical values match within the error.

Further measurements would profit from a better characterisation of the PolarX-EBIT parameters. A more comprehensive study of the extraction system could be performed, since the shape and size of the peaks does depend on the beam line parameters. In addition, the work function of the titanium alloy drift tubes was approximated by the work function of pure titanium which might lead to a systematic shift of the determined resonance energies.

The electron beam radius determined from the space charge is a factor of 3 to 5 lower than the calculated Herrmann radius. The reason for this is not precisely known. The deviation might be due to the assumption that the space charge potential inside the electron beam is completely flat due to the ion compensation. It is also questionable, that the Herrmann radius can be directly applied to the off-axis gun due to the deflection of the beam which changes the size and shape of the beam.

For future measurements of the absolute resonance strengths, it would be interesting to estimate the overlap factor more accurately. One way to estimate the overlap would be to utilise optical spectroscopy of metastable states whose lifetime is longer than the orbital period of the ion cloud, therefore emitting throughout the whole ion cloud and not only in the overlap with the electron beam. For this, magnifying optical elements are needed [41, 42]. Another way would be to infer the overlap factor from the effective electron current density by analysing the line ratio of density sensitive spectral lines to density insensitive lines. This has already been accomplished with the FLASH-EBIT for highly charged iron ions [38]. For both methods, suitable transitions in oxygen ions have to be identified.

In addition, the polarization of the photon emission could be measured simultaneously by adding an on-axis photon detector to detect the fluorescence at 0° and 90°. By determining the

polarization of the emission, the resonance strengths averaged over the whole solid angle can be calculated from equation 2.7. This method was employed for example in [43] and [44].

A more precise measurement of the resonance strengths is of interest to test atomic theory and beneficial for the modeling and diagnosis of astrophysical and laboratory plasmas.

Bibliography

[1] H. F. Beyer and V. P. Shevelko, *Introduction to physics of highly charged ions*. Institute of Physics Publishing, 2003.

[2] J. D. Gillaspy, "Highly charged ions," *Journal of Physics B: Atomic, Molecular and Optical Physics*, vol. 34, no. 19, p. R93, 2001. [Online]. Available: https://dx.doi.org/10.1088/0953-4075/34/19/201

[3] G. Peres, S. Orlando, F. Reale, R. Rosner, and H. Hudson, "The Sun as an X-Ray Star. II. Using the Yohkoh/Soft X-Ray Telescope-derived Solar Emission Measure versus Temperature to Interpret Stellar X-Ray Observations," *The Astrophysical Journal*, vol. 528, no. 1, p. 537, jan 2000. [Online]. Available: https://dx.doi.org/10.1086/308136

[4] W. H. Wollaston, "XII. A method of examining refractive and dispersive powers, by prismatic reflection," *Philosophical Transactions of the Royal Society of London*, vol. 92, pp. 365–380, 1802. [Online]. Available: https://royalsocietypublishing.org/doi/abs/10.1098/rstl.1802.0014

[5] J. Fraunhofer, "Bestimmung des Brechungs- und des Farbenzerstreungs-Vermögens verschiedener Glasarten, in Bezug auf die Vervollkommnung achromatischer Fernröhre," *Annalen der Physik*, vol. 56, no. 7, pp. 264–313, 1817. [Online]. Available: https://onlinelibrary.wiley.com/doi/abs/10.1002/andp.18170560706

[6] G. Kirchhoff, "Ueber die Fraunhofer'schen Linien," *Annalen der Physik*, vol. 185, no. 1, pp. 148–150, 1860. [Online]. Available: https://onlinelibrary.wiley.com/doi/abs/10.1002/andp.18601850115

[7] B. Edlén, "Early Observations of Highly Charged Ions," *Physica Scripta*, vol. 1983, no. T3, p. 5, jan 1983. [Online]. Available: https://dx.doi.org/10.1088/0031-8949/1983/T3/001

[8] B. Edlén, "Die Deutung der Emissionslinien im Spektrum der Sonnenkorona. Mit 6 Abbildungen." *Zeitschrift für Astrophysik*, vol. 22, p. 30, Jan. 1943.

[9] T. W. Walter Roedel, *Physik unserer Umwelt: Die Atmosphäre*. Springer Berlin, Heidelberg, 2010. [Online]. Available: https://doi.org/10.1007/978-3-642-15729-5

[10] R. Giacconi, H. Gursky, F. R. Paolini, and B. B. Rossi, "Evidence for x Rays From Sources Outside the Solar System," *Phys. Rev. Lett.*, vol. 9, pp. 439–443, Dec 1962. [Online]. Available: https://link.aps.org/doi/10.1103/PhysRevLett.9.439

[11] H. Friedman, S. W. Lichtman, and E. T. Byram, "Photon Counter Measurements of Solar X-Rays and Extreme Ultraviolet Light," *Phys. Rev.*, vol. 83, pp. 1025–1030, Sep 1951. [Online]. Available: https://link.aps.org/doi/10.1103/PhysRev.83.1025

[12] R. E. Marrs, S. R. Elliott, and D. A. Knapp, "Production and trapping of hydrogenlike and bare uranium ions in an electron beam ion trap," *Phys. Rev. Lett.*, vol. 72, pp. 4082–4085, Jun 1994. [Online]. Available: https://link.aps.org/doi/10.1103/PhysRevLett.72.4082

[13] A. Burgess, "Delectronic Recombination and the Temperature of the Solar Corona." *Astrophysical Journal*, vol. 139, pp. 776–780, Feb. 1964.

[14] J. Dubau and S. Volonte, "Dielectronic recombination and its applications in astronomy," *Reports on Progress in Physics*, vol. 43, no. 2, p. 199, feb 1980. [Online]. Available: https://dx.doi.org/10.1088/0034-4885/43/2/002

[15] M. E. Foord, S. H. Glenzer, R. S. Thoe, K. L. Wong, K. B. Fournier, B. G. Wilson, and P. T. Springer, "Ionization Processes and Charge-State Distribution in a Highly Ionized High- Z Laser-Produced Plasma," *Phys. Rev. Lett.*, vol. 85, pp. 992–995, Jul 2000. [Online]. Available: https://link.aps.org/doi/10.1103/PhysRevLett.85.992

[16] R. Bartiromo, F. Bombarda, and R. Giannella, "Spectroscopic study of nonthermal plasmas," *Phys. Rev. A*, vol. 32, pp. 531–537, Jul 1985. [Online]. Available: https://link.aps.org/doi/10.1103/PhysRevA.32.531

[17] J. F. Seely, U. Feldman, and G. A. Doschek, "Observations of Nonthermal Energy Distributions during the Impulsive Phase of Solar Flares," *Astrophysical Journal*, vol. 319, p. 541, Aug. 1987.

[18] C. Kobayashi, H. Umeda, K. Nomoto, N. Tominaga, and T. Ohkubo, "Galactic Chemical Evolution: Carbon through Zinc," *Astrophysical Journal*, vol. 653, no. 2, pp. 1145–1171, Dec. 2006. [Online]. Available: https://iopscience.iop.org/article/10.1086/508914

[19] K. Lodders, "Solar Elemental Abundances," 2019. [Online]. Available: https://doi.org/10.48550/arXiv.1912.00844

[20] F. Currell and G. Fussmann, "Physics of electron beam ion traps and sources," *IEEE Transactions on Plasma Science*, vol. 33, pp. 1763–1777, 2005. [Online]. Available: https://doi.org/10.1109/TPS.2005.860072

[21] J. R. C. López-Urrutia, "Frequency metrology using highly charged ions," *Journal of Physics: Conference Series*, vol. 723, no. 1, p. 012052, jun 2016. [Online]. Available: https://dx.doi.org/10.1088/1742-6596/723/1/012052

[22] S. M. Cavaletto, Z. Harman, C. Ott, C. Buth, T. Pfeifer, and C. H. Keitel, "Broadband high-resolution x-ray frequency combs," *Nature Photonics*, vol. 8, no. 7, pp. 520–523, 2014.

[23] S. Dobrodey, "Charge-exchange studies of bare and hydrogen-like low-Z ions in the X-ray and extreme-ultraviolet ranges inside an electron beam ion trap," Ph.D. dissertation, Ruprecht-Karls-Universität, Heidelberg, 2019. [Online]. Available: https://hdl.handle.net/21.11116/0000-0005-5881-6

[24] B. J. Wargelin, S. M. Kahn, and P. Beiersdorfer, "Dielectronic satellite contributions to Ne VIII and Ne IX K-shell spectra," *Phys. Rev. A*, vol. 63, p. 022710, Jan 2001. [Online]. Available: https://doi.org/10.1103/PhysRevA.63.022710

[25] K. L. Wong, P. Beiersdorfer, R. E. Marrs, K. J. Reed, and D. A. Vogel, "Electron impact excitation cross section measurements of highly charged heliumlike and lithiumlike ions," *AIP Conference Proceedings*, vol. 274, no. 1, pp. 545–548, 1993. [Online]. Available: https://doi.org/10.1063/1.43663

[26] S. Kühn, "High-precision soft X-ray transition measurements of neon-like mid-Z ions using ultra monochromatic synchrotron radiation," Ph.D. dissertation, Ruprecht-Karls-Universität, Heidelberg, 2021. [Online]. Available: https://hdl.handle.net/21.11116/0000-0009-8C16-1

[27] L. Brillouin, "A Theorem of Larmor and Its Importance for Electrons in Magnetic Fields," *Phys. Rev.*, vol. 67, pp. 260–266, Apr 1945. [Online]. Available: https://link.aps.org/doi/10.1103/PhysRev.67.260

[28] G. Herrmann, "Optical Theory of Thermal Velocity Effects in Cylindrical Electron Beams," *Journal of Applied Physics*, vol. 29, no. 2, pp. 127–136, 1958. [Online]. Available: https://doi.org/10.1063/1.1723053

[29] J. Gillaspy, *Trapping Highly Charged Ions: Fundamentals and Applications*. Nova Publisher, Hauppauge, NY, 2000-04-01 2000.

[30] V. Pastukhov, "Collisional losses of electrons from an adiabatic trap in a plasma with a positive potential," *Nuclear Fusion*, vol. 14, no. 1, p. 3, jan 1974. [Online]. Available: https://dx.doi.org/10.1088/0029-5515/14/1/001

[31] W. Demtröder, *Experimentalphysik 3: Atome, Moleküle und Festkörper*, 5th ed., ser. Springer-Lehrbuch. Springer Spektrum Berlin, Heidelberg, 2016.

[32] M. Togawa, "Investigation of the M-shell unresolved transition array of aluminium-like iron using monochromatic soft x-ray synchrotron radiation," Master's thesis, Ruprecht-Karls-Universität, Heidelberg, 2021. [Online]. Available: https://hdl.handle.net/21.11116/0000-0009-1027-9

[33] L. B. P. Micke, S. Kühn *et al.*, "The Heidelberg compact electron beam ion traps," *Review of Scientific Instruments*, vol. 89, no. 6, p. 063109, 2018. [Online]. Available: https://doi.org/10.1063/1.5026961

[34] L. Buchauer, "Konstruktion einer kompakten Elektronenstrahl-Ionenfalle mit Permanentmagneten für Fluoreszenzmessungen," Bachelor's thesis, Ruprecht-Karls-Universität, Heidelberg, 2012. [Online]. Available: https://hdl.handle.net/11858/00-001M-0000-0014-6A23-9

[35] J. Danisch, "Search for the O_{16}^{4+} /O_{18}^{4+} isotope shift in the photoionization of Be-like oxygen with monochromatic soft X-ray synchrotron radiation," Bachelor's thesis, Ruprecht-Karls-Universität, Heidelberg, 2022. [Online]. Available: https://hdl.handle.net/21.11116/0000-000A-BC19-7

[36] W. M. Haynes, *CRC Handbook of Chemistry and Physics*, 95th ed. CRC Press, 2014.

[37] K. E. Atkinson, *An Introduction to Numerical Analysis*, 2nd ed. New York: John Wiley & Sons, 1989. [Online]. Available: http://www.worldcat.org/isbn/0471500232

[38] G. Y. Liang, J. R. C. López-Urrutia, T. M. Baumann, S. W. Epp, A. Gonchar, A. Lapierre, P. H. Mokler, M. C. Simon, H. Tawara, V. Mäckel, K. Yao, G. Zhao, Y. Zou, and J. Ullrich, "Experimental investigations of ion charge distributions, effective electron densities, and electron-ion cloud overlap in electron beam ion trap plasma using extreme-ultraviolet spectrscopy," *The Astrophysical Journal*, vol. 702, no. 2, p. 838, aug 2009. [Online]. Available: https://dx.doi.org/10.1088/0004-637X/702/2/838

[39] W. Demtröder, *Electrodynamics and Optics*, ser. Undergraduate Lecture Notes in Physics. Springer International Publishing, 2019.

[40] B. Henke, E. Gullikson, and J. Davis, "X-Ray Interactions: Photoabsorption, Scattering, Transmission, and Reflection at E = 50-30,000 eV, Z = 1-92," *Atomic Data and Nuclear Data Tables*, vol. 54, no. 2, pp. 181–342, 1993. [Online]. Available: https://doi.org/10.1006/adnd.1993.1013

[41] T. P. Arthanayaka, P. Beiersdorfer, G. V. Brown, M. Hahn, N. Hell, T. E. Lockard, and D. W. Savin, "Measurements of the effective electron density in an electron beam ion trap using extreme ultraviolet spectra and optical imaging," *Review of Scientific Instruments*, vol. 89, no. 10, p. 10E119, Oct. 2018.

[42] T. Arthanayaka, P. Beiersdorfer, G. V. Brown, M. F. Gu, M. Hahn, N. Hell, T. Lockard, and D. W. Savin, "Laboratory calibrations of fe xii–xiv line-intensity ratios for electron density diagnostics," *The Astrophysical Journal*, vol. 890, no. 1, p. 77, feb 2020. [Online]. Available: https://dx.doi.org/10.3847/1538-4357/ab67b4

[43] C. Shah, P. Amaro, R. Steinbrügge, S. Bernitt, J. R. C. López-Urrutia, and S. Tashenov, "Polarization of k-shell dielectronic recombination satellite lines of fe xix–xxv and its application for diagnostics of anisotropies of hot plasmas," *The Astrophysical Journal Supplement Series*, vol. 234, no. 2, p. 27, feb 2018. [Online]. Available: https://dx.doi.org/10.3847/1538-4365/aaa4c0

[44] C. Shah, N. Hell, A. Hubbard, M. F. Gu, M. J. MacDonald, M. E. Eckart, R. L. Kelley, C. A. Kilbourne, M. A. Leutenegger, F. S. Porter, and G. V. Brown, "High-resolution laboratory measurements of k-shell x-ray line polarization and excitation cross sections in helium-like s xv ions," *The Astrophysical Journal*, vol. 914, no. 1, p. 34, jun 2021. [Online]. Available: https://dx.doi.org/10.3847/1538-4357/abf1ea

6 Appendix

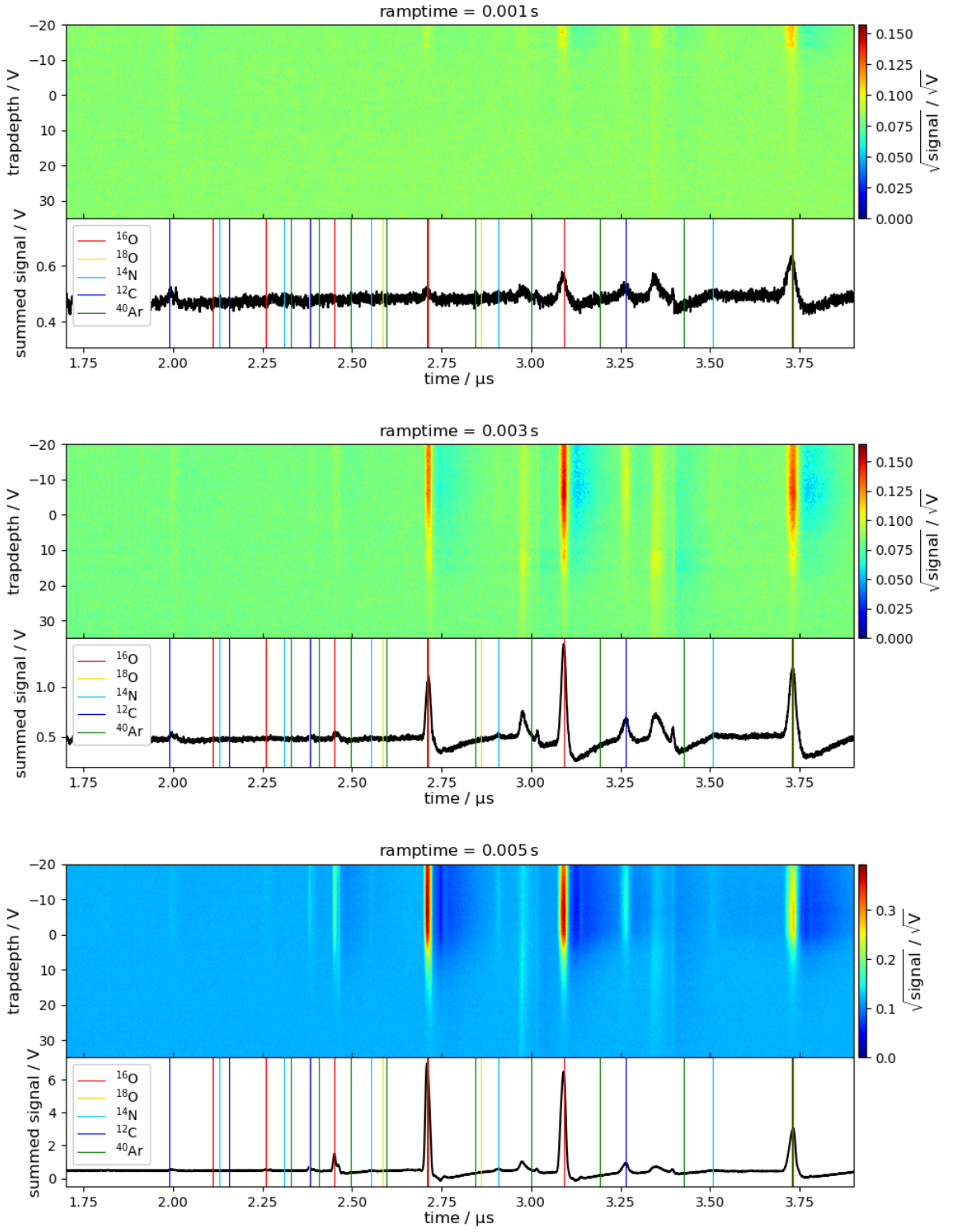

Figure 6.1: ToF scans. The upper half of the plots depicts the ToF signal for fixed ramp times of 0.001 s, 0.003 s and 0.005 s and varying trap depths. For better visibility, the square root of the signal is shown. The lower plots display the summed signal (black) and the ToF lines for ions of different q/m ratio (colored) similar to Figure 4.3. The ion lines are calculated using the parameters estimated in section 4.2.

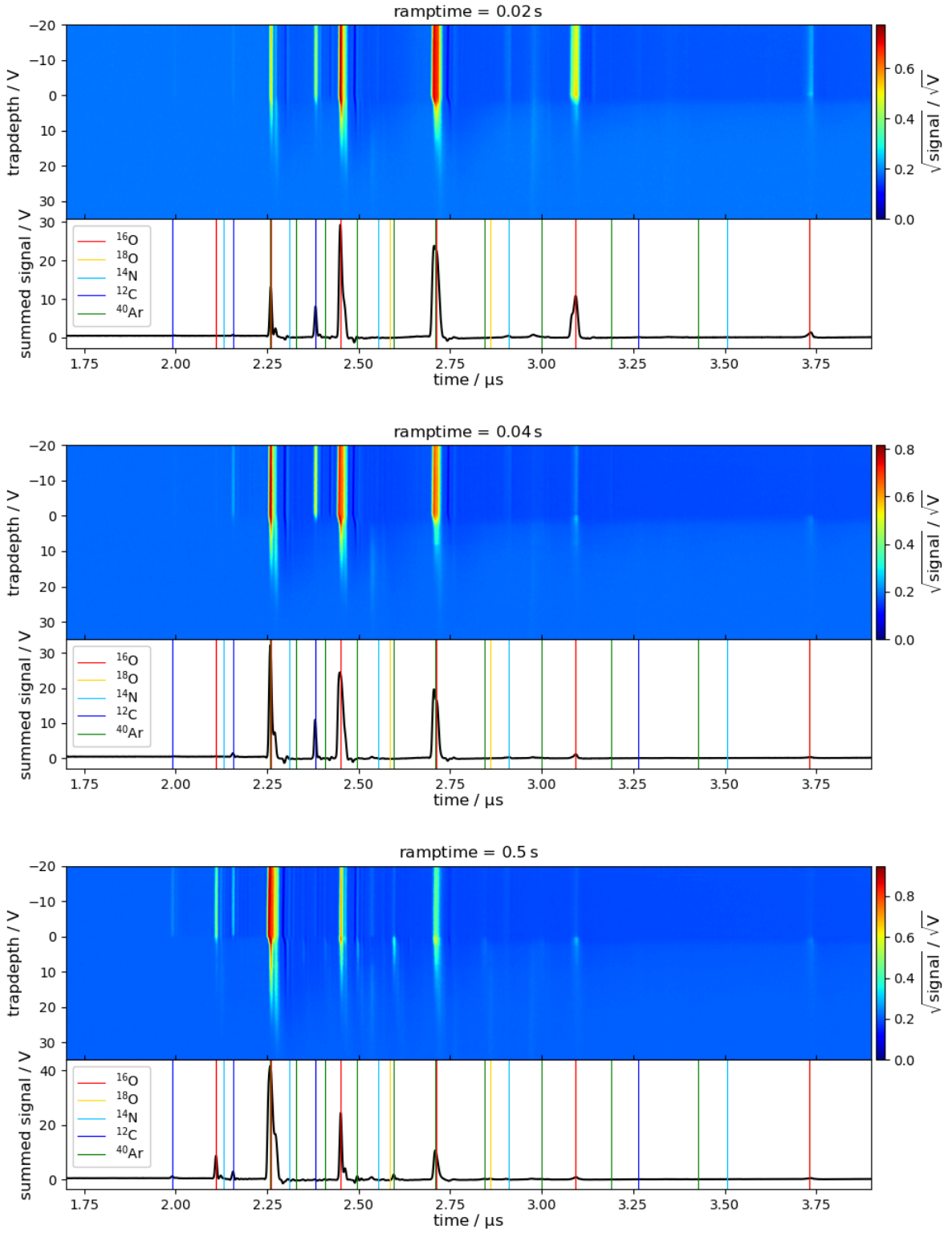

Figure 6.2: ToF scans as in Figure 6.1 for fixed ramp times of 0.02 s, 0.04 s and 0.5 s and varying trap depths.

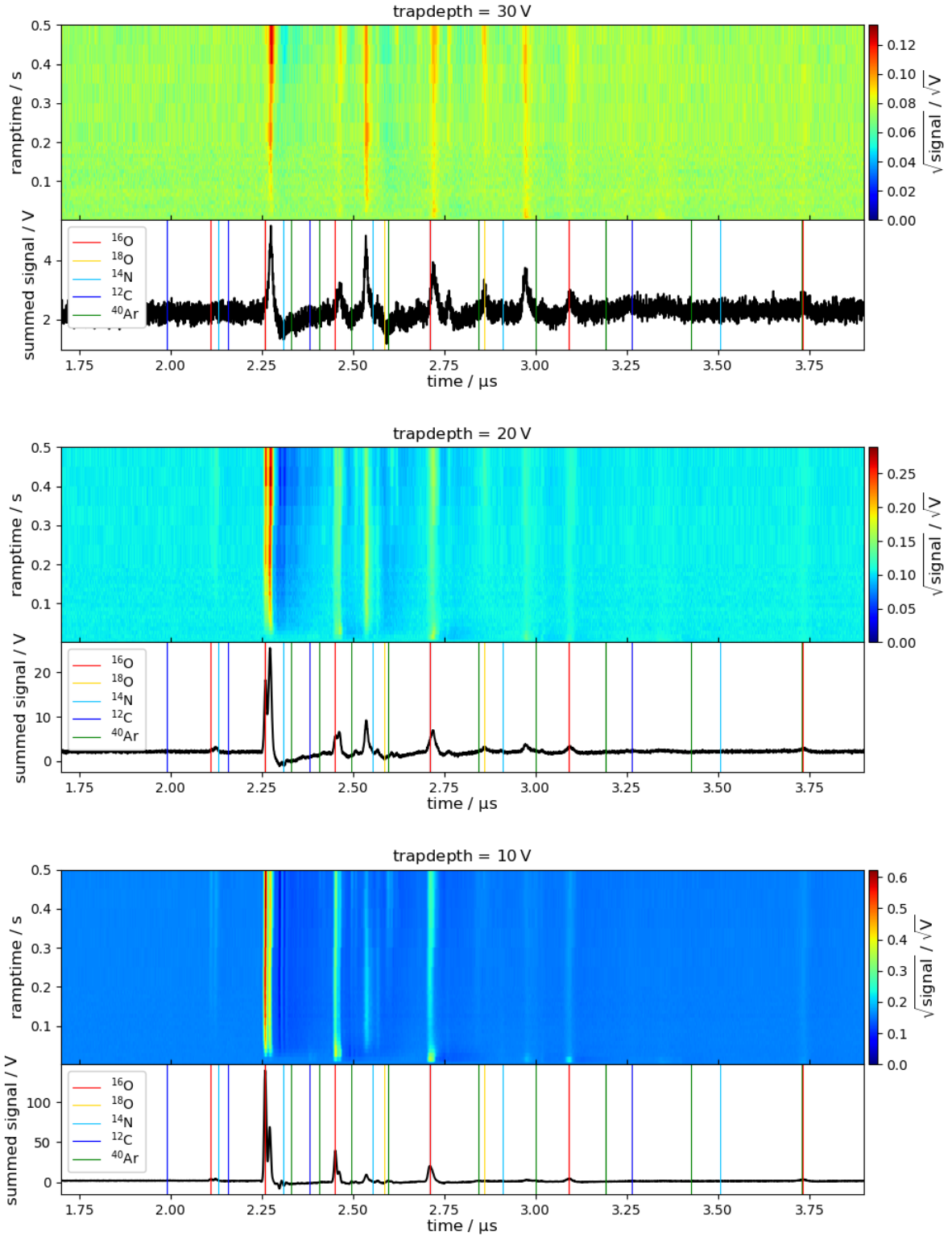

Figure 6.3: ToF scans as in Figure 6.1 for fixed trap depths of 30 V, 20 V and 10 V and varying ramp times.

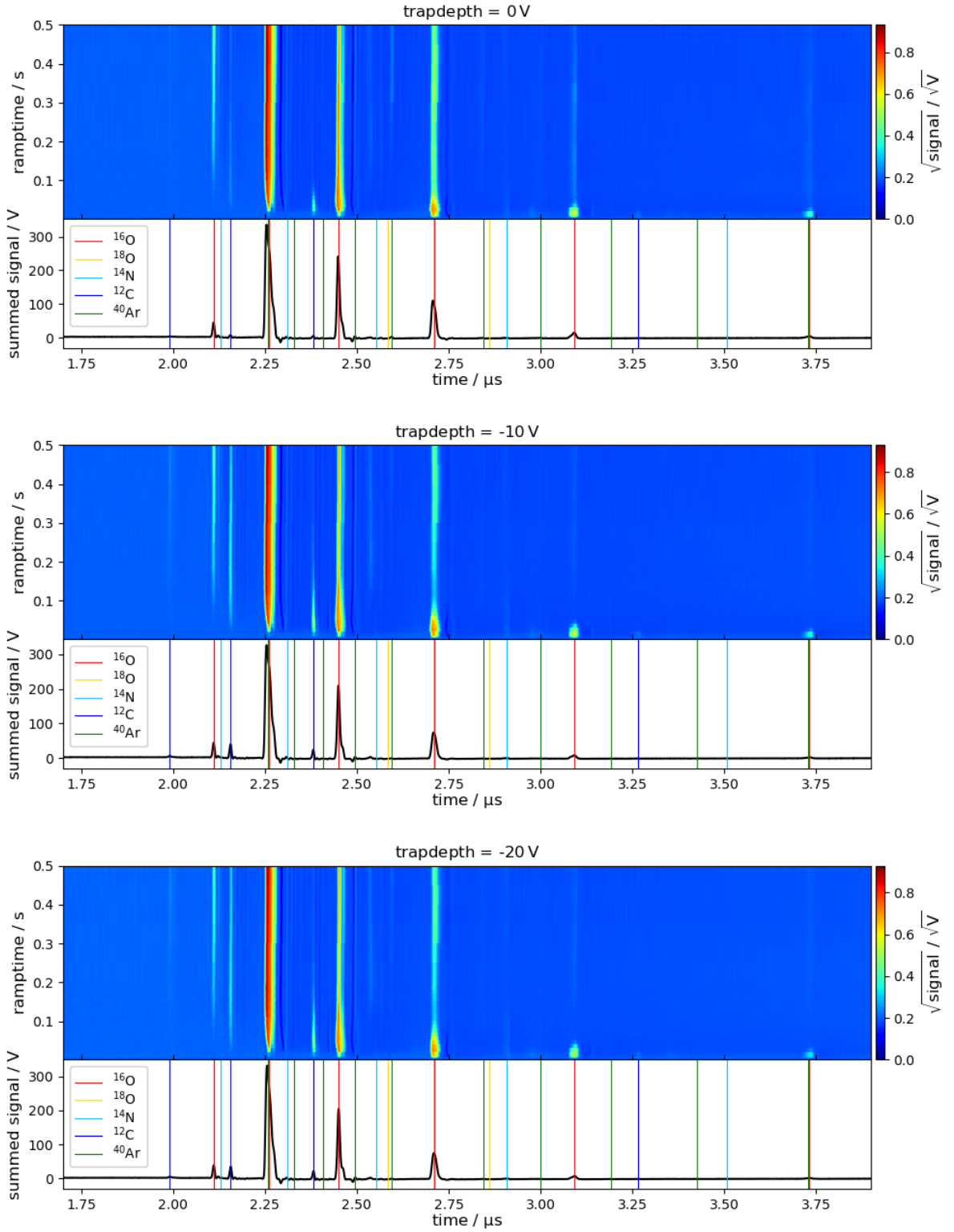

Figure 6.4: ToF scans as in Figure 6.1 for fixed trap depths of 0 V, -10 V and -20 V and varying ramp times.

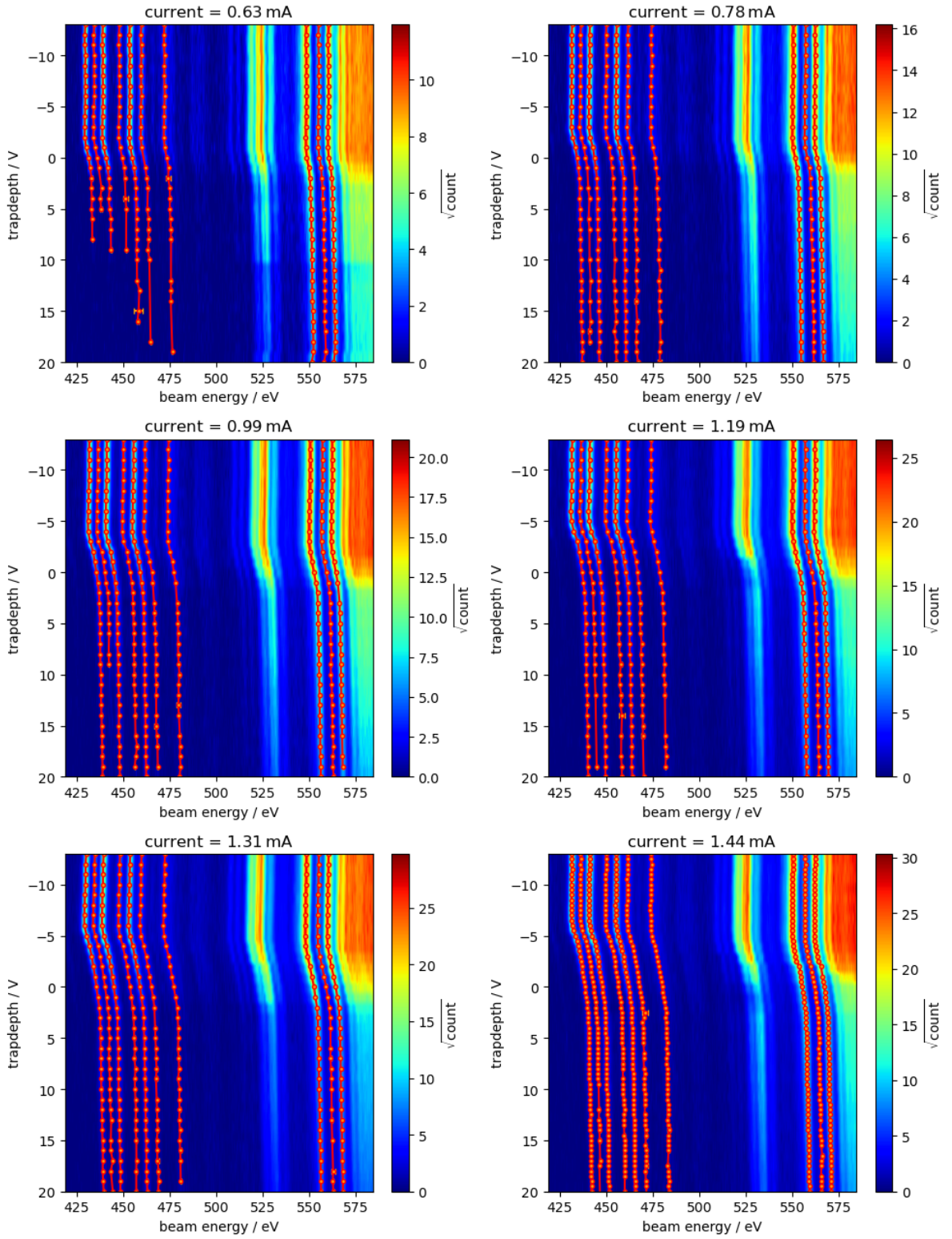

Figure 6.5: Summed photon count for the K_α emission as a function of the electron beam energy and the trap depth for various electron beam currents. Ten resonances were selected, fitted with a Gaussian distribution for each trap depth and ordered into lines. The center of the Gaussian functions are marked in red. The square root of the count is shown for better visibility.

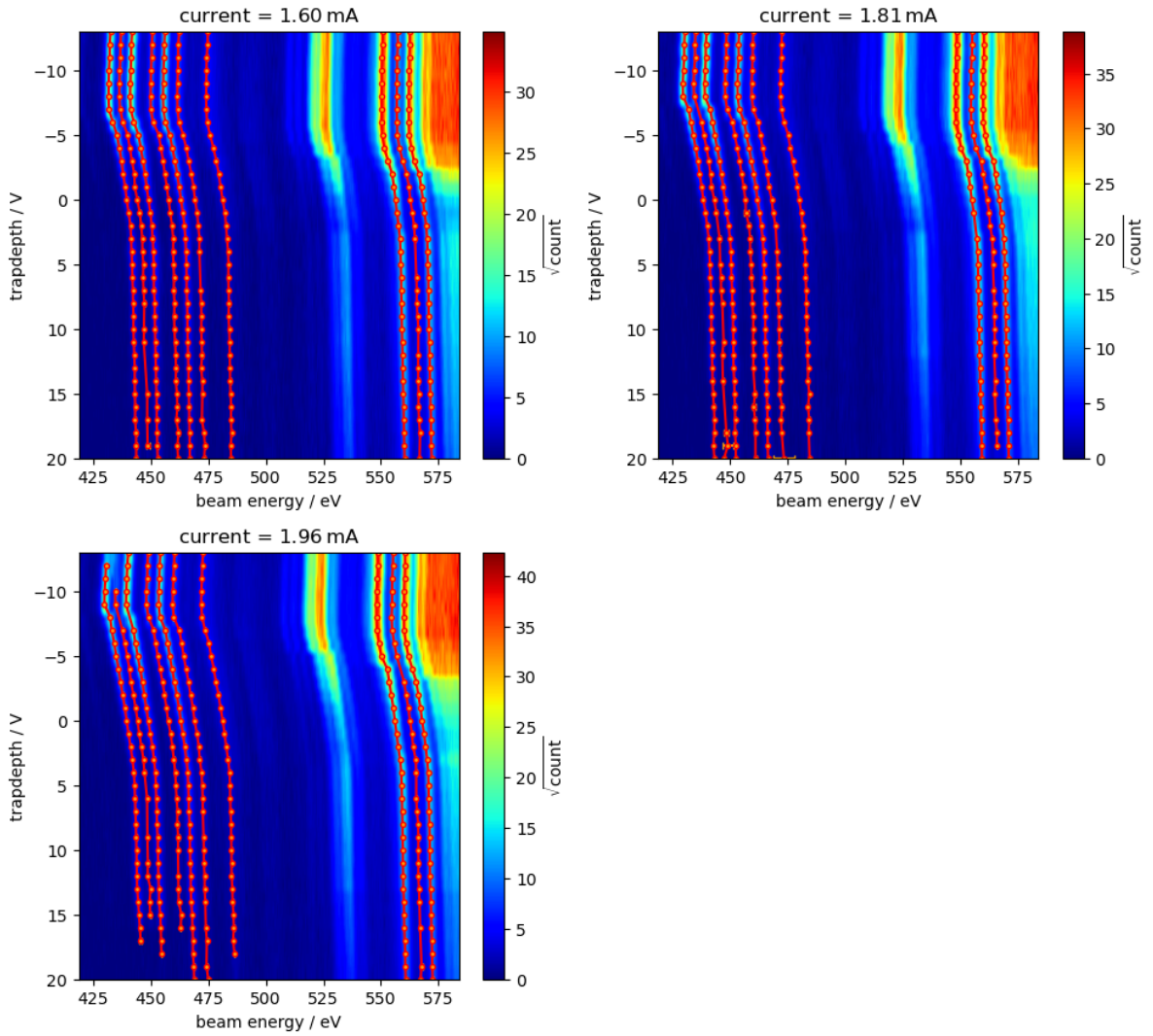

Figure 6.6: Summed photon count for the K_α emission as in Figure 6.5 for various electron beam currents.

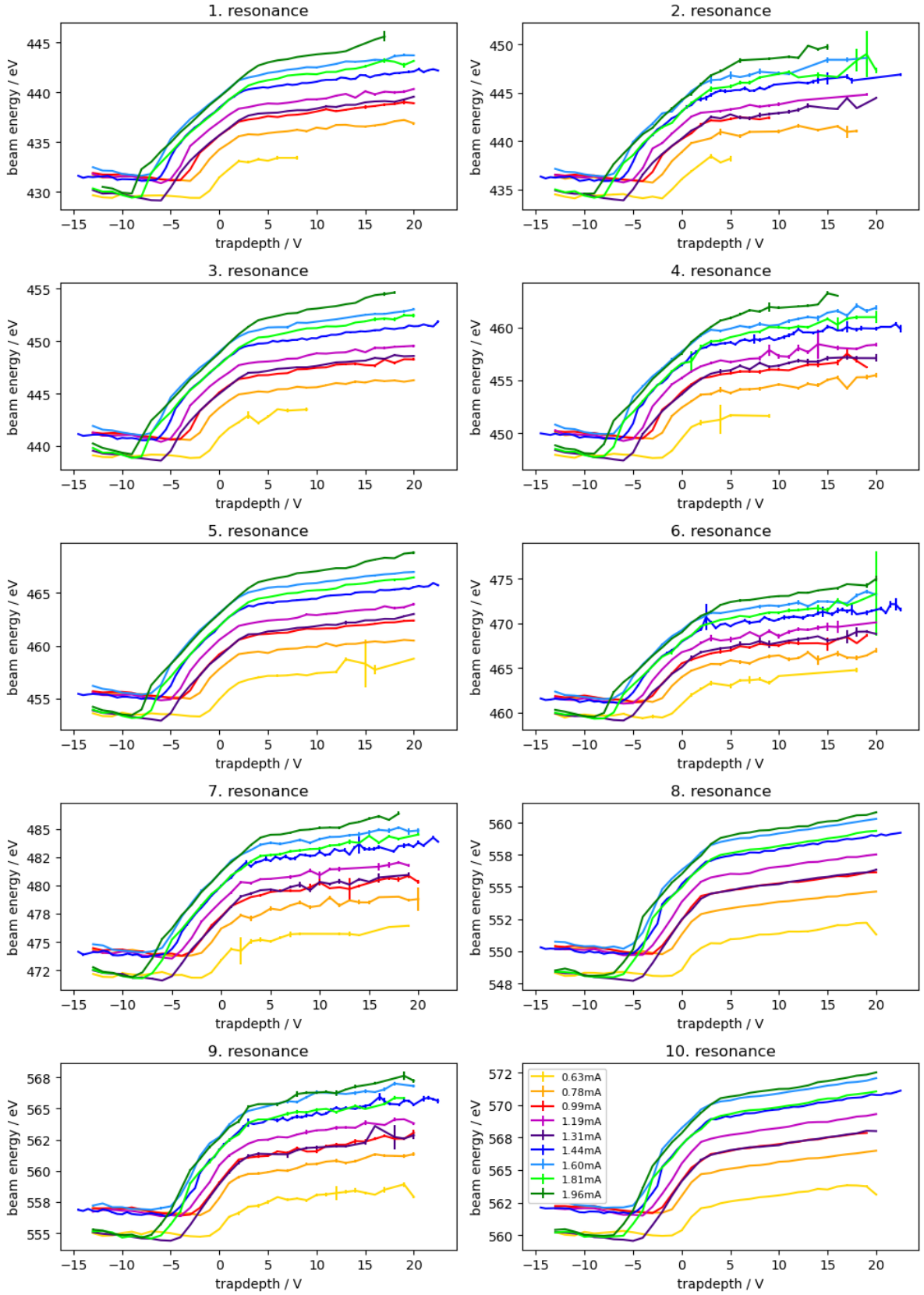

Figure 6.7: Fitted positions of all resonances as a function of the trap depth. Each line represents a different electron beam current.

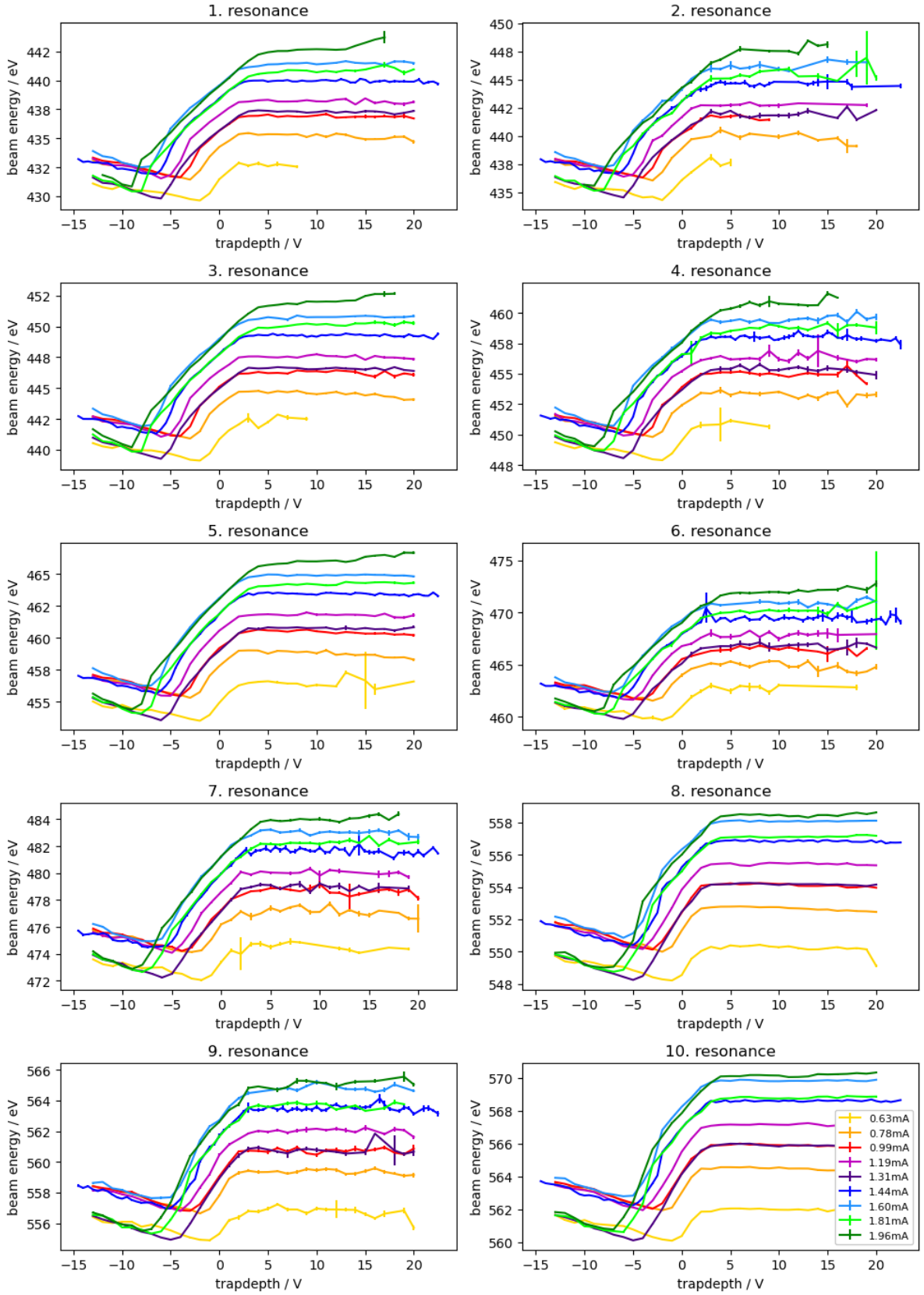

Figure 6.8: Fitted positions of all resonances as in Figure 6.7 after the correction for the reach-through effect.

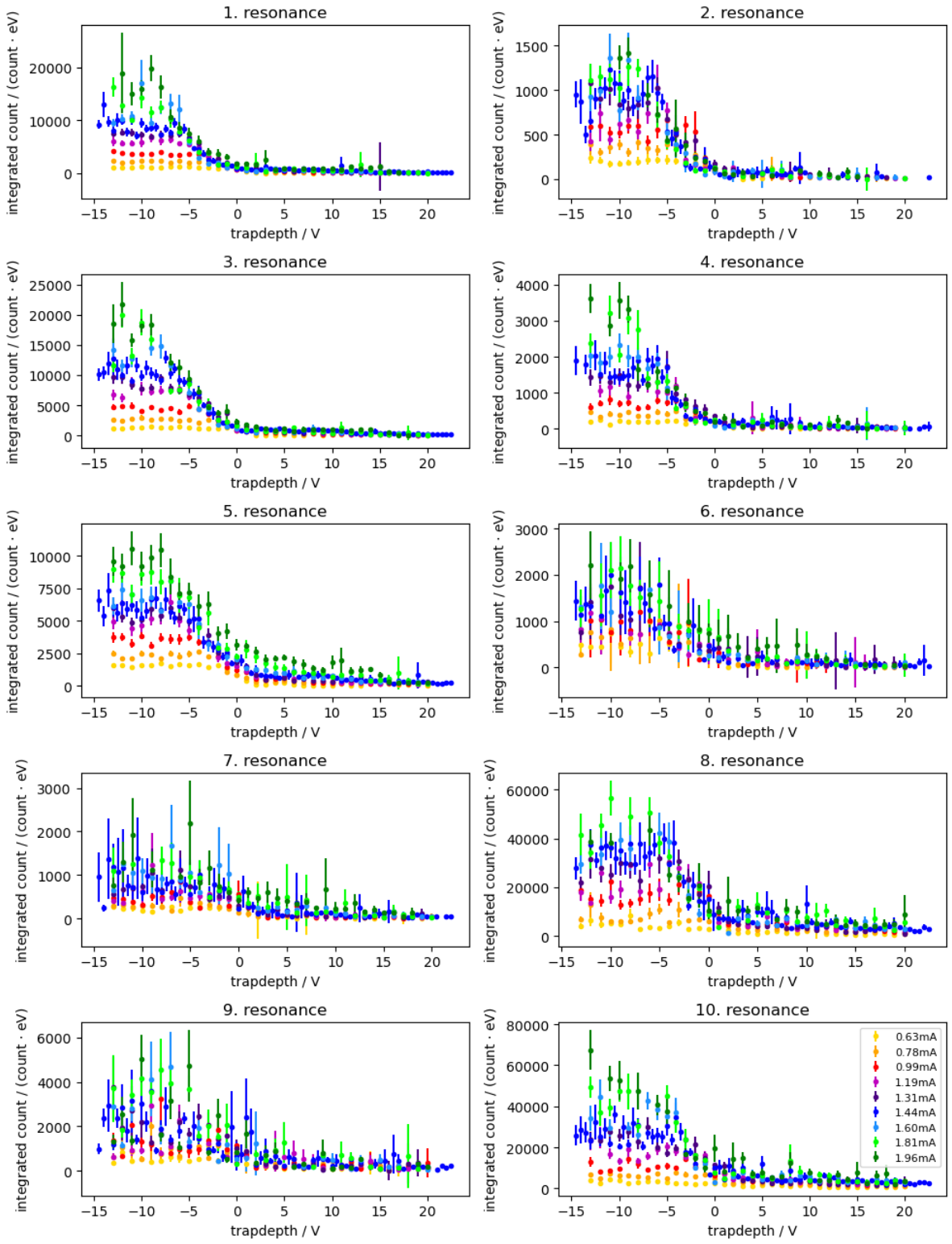

Figure 6.9: Area of the Gaussian function fitted to the resonance peaks as a function of the trap depth for all resonances. Each color represents a specific electron beam current.

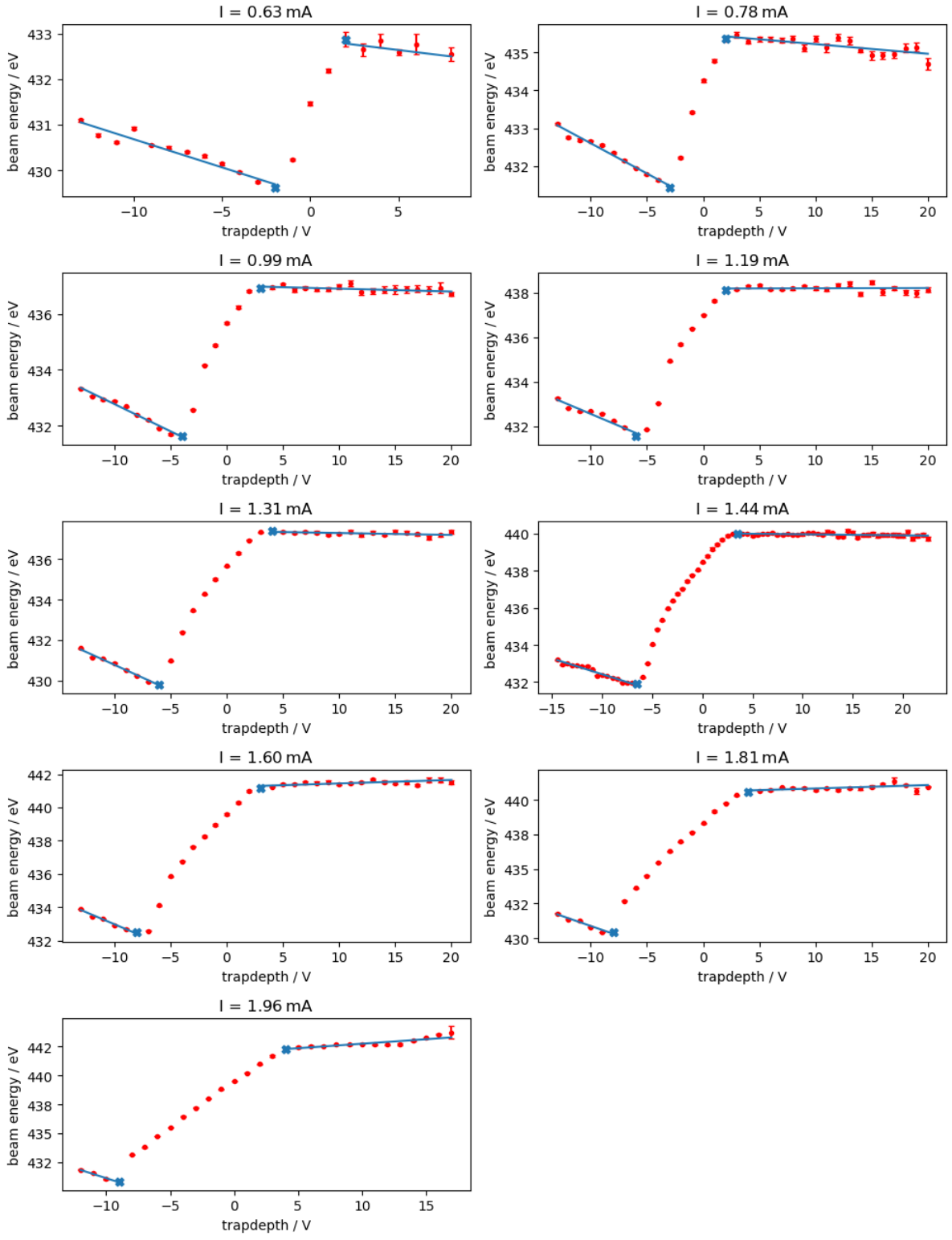

Figure 6.10: Determining the transition points between the three different regions for the first resonance line. The transition points are shown for all measured electron beam currents. The resonance positions (red) are plotted as a function of the trap depth and fitted with a line (blue) in the first and third section. Blue crosses mark the determined intersection points.

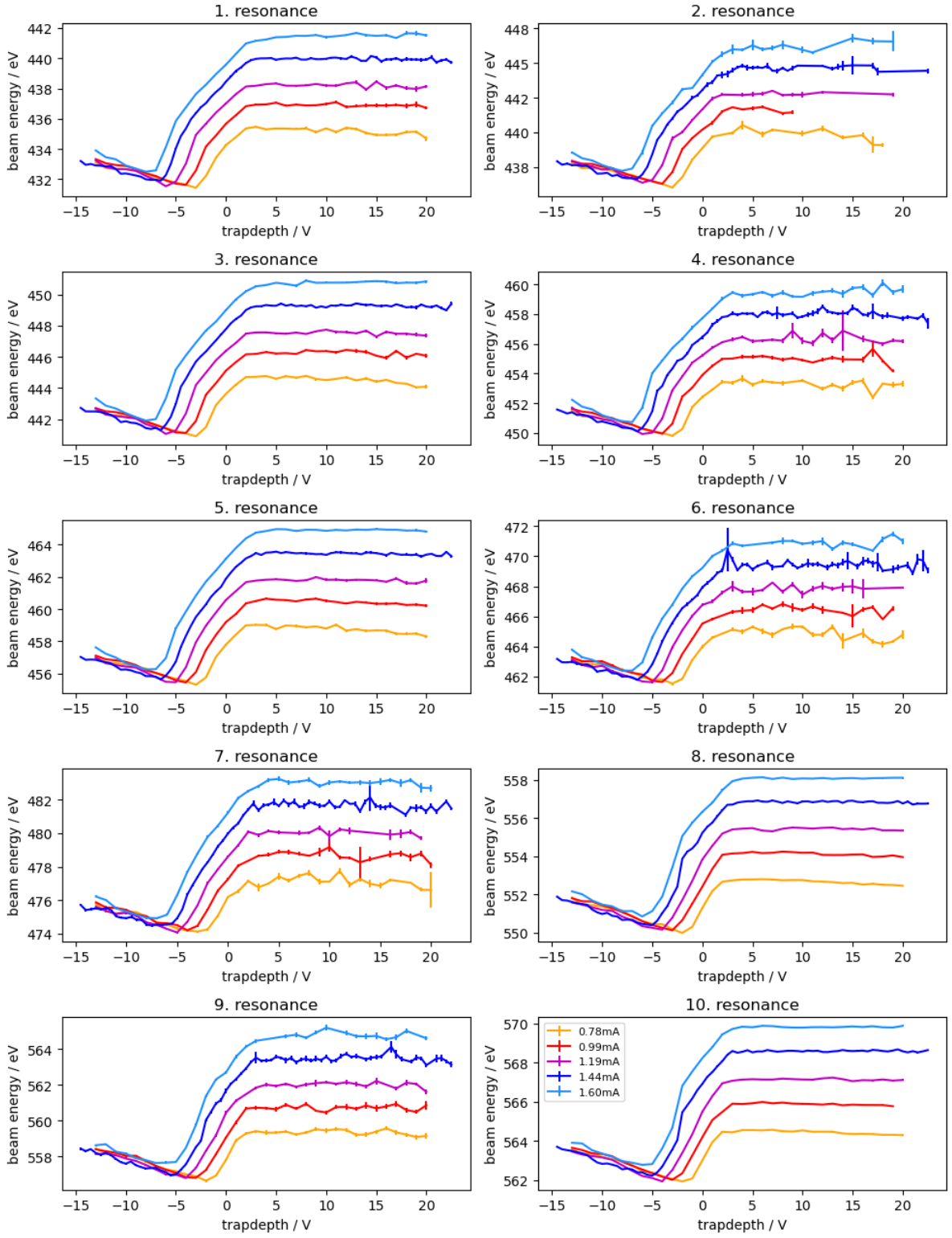

Figure 6.11: Electron beam energy of all resonances as a function of the trap depth for the currents that were selected for the determination of the electron and ion space charge. Each line represents a specific electron beam current.

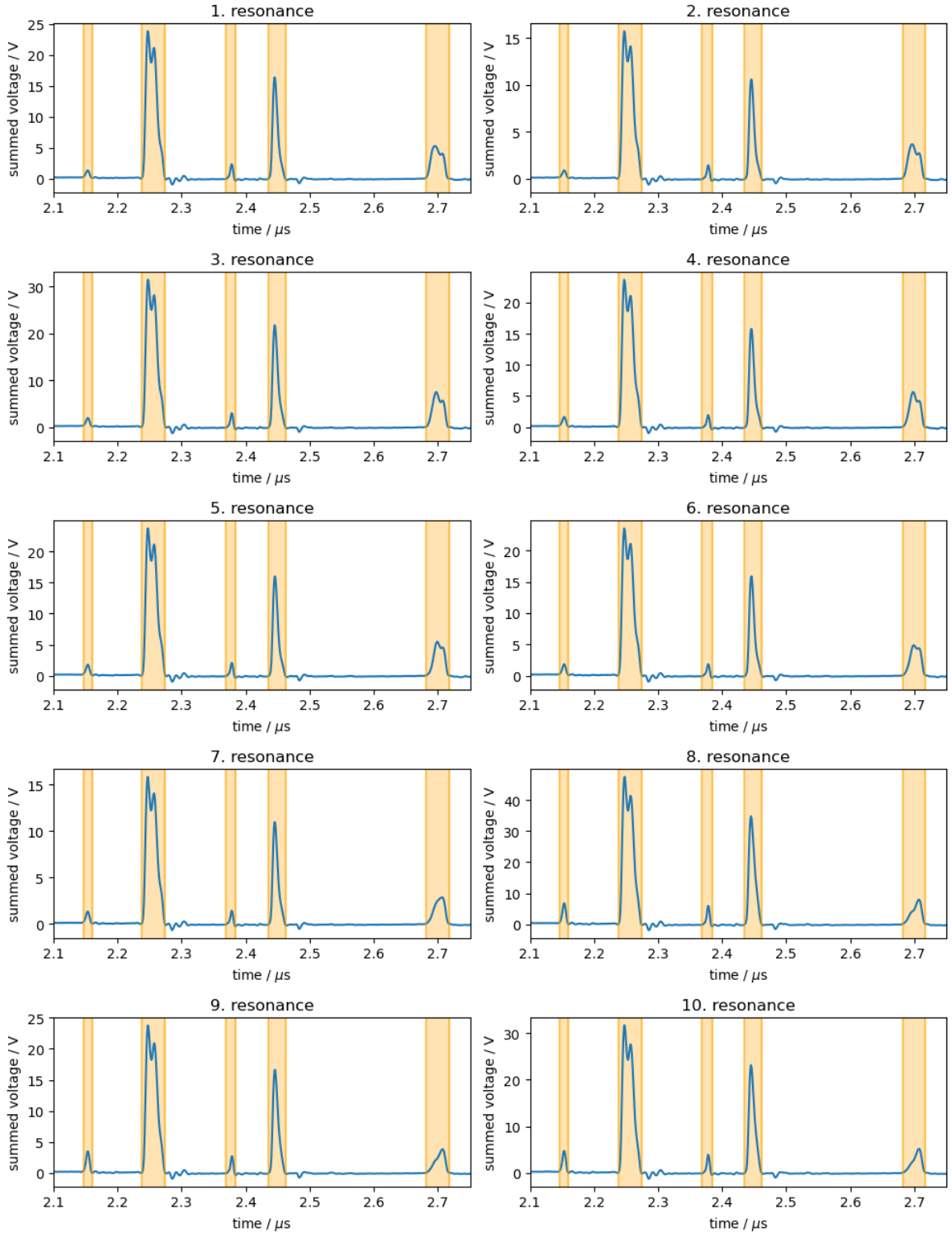

Figure 6.12: Summed ToF signal for all DR resonance. The ion peaks that are integrated to calculate the charge state distribution are marked in orange. The corresponding charge state are marked in Figure 4.30.